Simulation of Tracer Diffusion and Retention for Hypoxia Imaging with Positron Emission Tomography in Two- and Three-Dimensional Tumor Models

Dissertation
der Mathematisch-Naturwissenschaftlichen Fakultät
der Eberhard Karls Universität Tübingen
zur Erlangung des Grades eines
Doktors der Naturwissenschaften
(Dr. rer. nat.)

vorgelegt von
Linda-Jacqueline Wack
aus Lohr a. Main

Tübingen
2017

Tag der mündlichen Qualifikation:	19. Juni 2017
Dekan:	Prof. Dr. Wolfgang Rosenstiel
1. Berichterstatter:	Prof. Dr. Dr. Fritz Schick
2. Berichterstatter:	Prof. Dr. Daniela Thorwarth

Abbreviations

2D - Two-dimensional
3D - Three-dimensional
AIF/AIP - Average input function
CT - Computed tomography
CuATSM - ^{64}Cu(-II)-diacetyl-bis(N4- methylthiosemicarbazone
DCE - dynamic contrast enhanced
DTA - Distance to agreement
FEM - Finite element method
FDG - Fluorodesoxyglucose
FMISO - [^{18}F]fluoromisonidazole
FAZA - [^{18}F]fluoroazomycinarabinoside
FWHM - Full width at half maximum
GTV - Gross tumor volume
HE - Hematoxylin and eosine
HF - Hypoxic fraction
HX4 - [^{18}F]flortanidazole
IF - Immunofluorescence
IMRT - Intensity modulated radiotherapy
Linac - linear accelerator
LOR - Line of response
MRI - Magnetic resonance imaging
PDE - Partial differential equation
PET - Positron emission tomography
pO_2- oxygen partial pressure (oxygen tension)
p.i. - post injection
PSF - Point-spread function
RT - Radiotherapy
HNSCC - Squamous cell carcinoma of the head-and-neck
TAC - Time activity curve
T/B - Tumor to blood concentration ratio
ROI - Region of interest
VMAT - volumetric modulated arc therapy

Declaration of the framework of this collective work

Parts of this thesis have been published as a collective work, or have been submitted for publication to international peer-reviewed journals of Medical Physics. The contributions of each author are specified below.

I. Correlation of FMISO simulations with pimonidazole-stained tumor xenografts: A question of pO_2 consumption?

published in *Medical Physics 2016, 43: 4113-4121*

Linda Wack	First author, conception and execution of the study, data analysis, writing of the manuscript
David Mönnich	Development of the original mathematical model
Ala Yaromina	Immunofluorescence labelling and analysis of the tumor sections
Daniel Zips	Critical discussion of the results, proof-reading of the manuscript
Michael Baumann	Critical discussion of the results, proof-reading of the manuscript
Daniela Thorwarth	Supervision of the project, study conception

II. Three-dimensional simulation of [^{18}F]FMISO diffusion and retention in a realistic microscopic vessel architecture: A performance evaluation

submitted to *Physics in Medicine and Biology*

Linda Wack	First author, conception and execution of the study, data analysis, writing of the manuscript
David Mönnich	Development of the original mathematical model, critical discussion of the manuscript
Apostolos Menegakis	Culturing of tumor cells, assistance with immunofluorescence labelling and microscopy
Simon Böke	Culturing of tumor cells, animal care and handling, executing of PET/MR imaging

René Winter	Execution of PET/MR imaging, analysis of PET data
Katrin Trautmann	Cutting of cryosections
Aline Leun	Analysis of PET/MR data
Gregory Bowden	Assistance with FMISO production
Jonathan Cotton	Assistance with PET/MR imaging
Marcel Krueger	Assistance with PET/MR imaging
Bernd Pichler	Advice on PET/MR imaging
Daniel Zips	Critical discussion of the results, proof-reading of the manuscript
Daniela Thorwarth	Supervision of the project, study conception

III. Comparison of [18F]-FMISO, [18F]-FAZA and [18F]-HX4 for PET imaging of hypoxia - a simulation study

published in *Acta Oncologica 2015, 54: 1370-1377*

Linda Wack	First author, conception and execution of the study, data analysis, writing of the manuscript
David Mönnich	Development of the original mathematical model
Wouter van Elmpt	HX4 PET image acquisition
Catharina Zegers	HX4 PET image acquisition, primary contact person in Maastricht
Esther Troost	HX4 data acquisition
Daniel Zips	Critical discussion of the results, proof-reading of the manuscript
Daniela Thorwarth	Supervision of the project, study conception

Contents

1 Introduction

Cancer is one of the leading causes of death world-wide, and the most common cause of death in Germany after cardiovascular diseases [1]. Aside from surgery and chemotherapy, radiotherapy (RT) has emerged as an established mode of treatment in oncology over the course of the 20th century. It is estimated that 50% of all cancer patients would benefit from RT, either as a stand-alone treatment or in combination with surgery and chemotherapy [2]. In short, the aim of RT is to apply ionizing radiation to the tumor, while at the same time minimizing dose to the surrounding tissue and organs to prevent side effects.

The foundation of RT was laid by W.C. Röntgen with the discovery of the X-rays in 1895 [3]. Researchers at the time quickly realized the huge potential of this discovery for medical diagnostics and therapy, with treatment of benign and malignant lesions starting before the end of the 19th century [4].

From there, radiotherapy advanced continuously to the treatment modalities we know today. The benefit of fractionated treatment to healthy tissue was first suggested in 1919 [5, 6], and in the 1920's, irradiation from multiple directions, called "Kreuzfeuerbestrahlung" (cross-fire irradiation) was established, a precursor of modern conformal radiotherapy [7]. After the second world war, betatrons and linear accelerators (linac) became available for irradiation with photon energies in the MeV range [8, 9], allowing for the treatment of tumors in deeper body regions, and reducing side effects to the skin due to their decreased surface dose.

Through the invention of better imaging modalities in recent decades, such as computed tomography (CT) and positron emission tomography (PET) [10], the ability to acquire precise 3D images to locate and distinguish tumor tissue from surrounding healthy tissue has improved. Meanwhile the development of advanced radiation delivery techniques such as intensity modulated RT (IMRT) or volumetric modulated arc therapy (VMAT) [11–13], has enabled oncologists to precisely deliver dose to the designated tumor area.

However, not all patients can be cured using state-of-the-art combination therapies including RT, chemotherapy and surgery. In head-and-neck cancer, about 50% of all treated patients suffer from local failures, with similar results being observed for other tumor entities [14]. With the currently clinically used method for tumor classification, which includes tumor location, stage and histology, it is not possible to predict which patients will be cured and who will suffer from a recurrence. Therefore, researchers aim to find additional ways to classify tumors and thus further individualize therapy to increase cure rates and long-term survival. Such approaches include gene signatures [15], the so-called radiomics, which aims to derive prognostic features from radiological imaging data [16], or

functional imaging, an approach to visualize functional and metabolic properties of the tumor tissue [17, 18].

One of the most heavily investigated biological changes frequently observed in tumors is hypoxia [19, 20], which differs among tumours of the same entity and even within the same tumor. Hypoxia is associated with decreased radiosensitivity [21], therefore, it is not surprising that the presence of hypoxia has been linked to poor prognosis for treatment outcome [22]. However, hypoxia is difficult to assess, and the current gold standard are invasive oxygen probes, which measure only small parts of the tumor. Research and diagnostics would greatly benefit from a non-invasive method to assess hypoxia in 3D and with high resolution.

However, no such method has been clinically established until now. Current research focuses on PET using radiolabelled nitroimidazole-based tracers as the most promising approach [23]. Originally developed as radiosensitizers [24], these compounds form a highly reactive product during intracellular reduction and bind quickly to cellular macromolecules in the absence of oxygen, thereby accumulating in hypoxic tissue. Labelling with the β^+-emitter ^{18}F allows for their detection via PET [25]. The oldest and most widely used nitroimidazole tracer is ^{18}F-Fluoromisonidazole (FMISO) [26].

Beyond its use as a potential prognostic tool [18, 27], it is anticipated that the information gained from hypoxia PET can be used to make RT adjustments to counteract hypoxia-induced radioresistance. Approaches include breathing of high oxygen content gas such as carbogen [28], the use of radiosensitizers [29], or targeted radiation dose escalation to hypoxic areas, a process referred to as "dose painting" [30, 31]. The goal of dose painting is to escalate the dose to hypoxic subvolumes to counteract hypoxia-induced radioresistance, thus achieving a homogeneous effectiveness of RT over the entire tumor volume. With the modern treatment modalities, dose painting is technically feasible and easy to implement in the clinic once its benefits for the patient have been conclusively shown in clinical trials [32].

However, the effectiveness of hypoxia dose painting is highly dependent on the reliability of hypoxia PET imaging [23]. Still, many factors that have an impact on hypoxia PET imaging are not yet fully understood. Some studies have concluded that static images prior to therapy might be sufficient to predict outcome [33], while others observed no such correlation [18]. Other studies use dynamic imaging approaches to predict outcome [27], as it is unclear whether static imaging is sufficient to correctly assess tumor hypoxia. There are many factors that can impact the quality of hypoxia imaging, such as variations in perfusion, acute hypoxia, or renal clearance of the tracer, whose impact remains poorly understood. Also, many new hypoxia tracers have been developed in recent years, and pre-clinical studies assessing their properties have been inconclusive [34–37].

Investigation of many of the problems mentioned above is difficult in experimental setup, as they often contain too many uncertainties to safely attribute observed changes to one single variable.

Here, mathematical models simulating the physical and chemical aspects of tracer accumulation offer another approach to gain additional insight. Such models allow for the quantification of each variable's impact on image signal, which can help advance our understanding of PET image formation and makes them a useful additional tool for the planning of clinical and pre-clinical studies and the evaluation of imaging protocols.

In the past, several mathematical models for the simulation of tissue oxygen distributions and resulting PET tracer accumulation have been published. These models commonly employ a two-step approach. In the first step, tissue oxygenation is simulated, which serves as an input for a subsequent simulation of PET tracer accumulation. First presented by Kelly and Brady [38], similar approaches have been presented by Mönnich *et al* [39–41], Dalah *et al* [42, 43], Bowen *et al* [44], and Warren and Partridge [45]. However, a thorough validation as well as a three-dimensional simulation of PET tracer retention on actual tumor vasculature is still lacking.

In this work, we develop and validate a simulation tool based on the work by Mönnich *et al* [39–41]. The simulations are carried out on realistic tumor vasculature and can be used as a tool to estimate the impact of individual parameters on PET signal. Additionally, the model is extended to three dimensions and a thorough experimental validation is performed to demonstrate the reliability of the simulation as a tool to evaluate imaging scenarios, which has not been performed for any of the published models so far. An application of the model is shown in the last part of this thesis. Here, multiple nitromimidazole-based tracers are compared to determine the impact of their pharmacokinetic properties on image contrast.

The goal of this thesis is to provide a robust 3D simulation model that can predict spatial and temporal hypoxia tracer accumulation with satisfying accuracy to support planning of clinical and pre-clinical studies and assess dedicated imaging protocols.

2 Objectives and outline of this thesis

This thesis consists of three parts, each of which dealing with the simulation of nitroimidazole PET tracers on realistic tumor vessel maps. All studies were performed in squamous cell carcinomas of the head and neck (HNSCC) tumor xenografts, but the methodology may easily be extended to other tumor entities as well. The following sections provide an overview of the performed studies.

- **Part I (Chapter 4)** In this part, a first step towards experimental validation of the simulation approach was taken. Until this point, neither oxygen nor hypoxia tracer simulation studies had been published that provided a validation beyond demonstrating plausibility. For this study, immunofluorescence images from nine different HNSCC cell lines were used as vessel maps to simulate two-dimensional (2D) FMISO accumulation. The model was set to include only functional vessels as determined by perfusion staining, and optimize the parameter M_0, the maximum oxygen consumption. The simulation results were compared to pimonidazole stainings consisting of microscopic sections of HNSCC tumors to determine correlation, and optimized parameters were analysed for cell line specific differences. The objective was to demonstrate the general validity of the method, and its applicability to a number of cell lines, before attempting a full 3D validation. At the same time, the numerical solution approach to the model was altered to accomodate for a future three-dimensional (3D) expansion of the model.
- **Part II (Chapter 5)** Here, the model was extended to 3D and a more thorough validation of the model was performed by validating both the spatial location of simulated FMISO accumulation as well as the simulated TACs, which extends the previous study. The objective was to provide a full validation of the model, thus confirming the validity of conclusions drawn from simulations in the past. For this, 2D and 3D simulations on vessel maps derived from HNSCC xenograft tumors were performed, and sensitivity and specificity of the approaches were determined by comparing the results to pimonidazole stainings. Simulated activities were compared to FMISO PET activities measured in the same tumor, as a validation of simulated overall activity.
- **Part III (Chapter 6)** deals with the impact of tracer diffusion and clearance on image quality. The motivation of this study was to evaluate how FMISO compares to the newly developed tracers [^{18}F]fluoroazomycinarabinoside (FAZA) and [^{18}F]flortanidazole (HX4), and which pharmakokinetical properties had the largest impact on image quality. These tracers had

originially been developed to provide better image contrast than FMISO, however, preclinical data investigating that claim was sparse and inconclusive (cf. Section 4.1). Thus, blood input data for each of the three tracers was determined from clinical dynamic PET scans, and the model previously developed by Mönnich *et al* was adjusted to account for the differences in clearance and diffusion, and to allow for a 3D expansion.

3 Scientific background

3.1 Tumor hypoxia and radiotherapy

3.1.1 Tumor vasculature and the causes of hypoxia

A functional vascular system is essential for the function of the body, as it is the main pathway to supply cells with nutrients and oxygen, and remove waste products and carbon dioxide. With very few exceptions, such as cartilage, all tissues in the human body rely on an intricate network of capillaries to exchange substances needed for their proper metabolic function. In this regard, solid tumors are no exception. They form a functional blood supply through angiogenesis, which is the growth of new blood vessel branches from the host vascular network [46]. However, the dedifferentiation and rapid growth of tumor cells result in a rather chaotic organization of tumor vasculature. This results in leaky, irregularly perfused blood vessels with frequent blind endings and irregular intervessel distances, which lead to a decrease of oxygen supply [23, 47]. Once the supply of oxygen falls below the oxygen demands of the tumor, hypoxia is the consequence [48].

3.1.2 Types of hypoxia

If intervessel distances increase beyond 200-400 μm, regions far away from the blood vessel are no longer adequately supplied with oxygen, leading to the formation of chronic, diffusion-limited hypoxia. Typically, a blood vessel can supply cells as far away as 100-200 μm from the vessel [49]. However, as blood oxygen content drops with increasing vessel length and due to the unorganized nature of tumor vasculature, hypoxic areas may be located closer to the vessel. This type of hypoxia has been known and described since the early 20th century in the Krogh cylinder model, which describes the oxygen supply along cylindrical vessels [50, 51], and later confirmed by Thomlinson and Gray in the 1950's [52]. An example of chronic hypoxia *in vivo* is shown in Figure 3.1.

Another type of hypoxia is more acute in nature. It is caused by transient perfusion changes in the blood vessels, leading to an acute reduction or even cease of blood flow in affected vessels [53, 54]. In acutely hypoxic tissue, the level of vessel perfusion may differ, and does not always result in a complete shutdown. Instead, only blood cells may be restricted from passing through the vessel, while plasma flow will be maintained, leaving the cells deprived of oxygen, but not of other nutrients [55]. The latter will lead to hypoxia, but not necessarily to necrosis, as tumor cells are often able to generate energy from non-oxidative breakdown of glucose through lactate acid fermentaion, and maintain a high

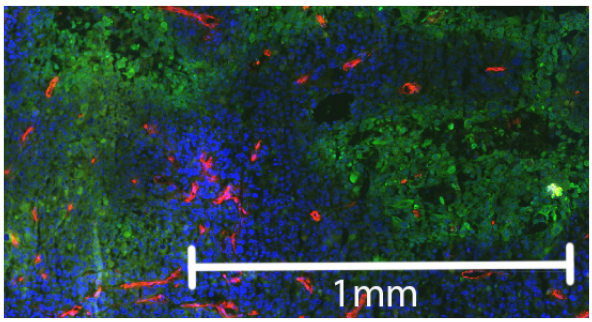

Figure 3.1: Chronic hypoxia in a HNSCC xenograft, as stained with pimonidazole. Colors indicate blood vessels (red, CD31), perfusion (blue, Hoechst) and hypoxia (green, pimonidazole). Note the distance of hypoxia from the perfused vessels.

level of cellular function. Though both types of hypoxia will lead to an increase in radioresistance, it is argued that acute hypoxia is the more dangerous type of the two, as acutely hypoxic cells are more likely to recover from radiation-induced cellular damage [56, 57].

3.1.3 Radiobiological effects of hypoxia

Since the 1950's, the impact of hypoxia on cell survival after radiotherapy has been investigated [21, 52], and it was found that the presence of hypoxia signifcantly decreases radiosensitivity. It was shown that the dose to hypoxic cells has to be increased by a factor of two to three to achieve the same level of damage observed in normoxic cells [21, 58].

There are several mechanisms that favor the survival of hypoxic cells under radiotherapy. For one, oxygen is important to fix radiation-induced damage to macromolecules in the cell. Ionizing radiation leads to the formation of free radicals, which ultimately cause tissue damage. These radicals, mostly hydroxyl free radicals, will interact with macromolecules in the cell, including DNA, resulting in DNA-derived free radicals. In the presence of oxygen, these radicals will react quickly with oxygen and then react further to produce a stable chemical change in the DNA molecule, frequently resulting in DNA strand breaks. In the absence of oxygen, however, the target is quickly reduced to its original form, effectively repairing the DNA damage [59–61].

There are also indications that hypoxia favors the survival of cancer cells with more aggressive phenotypes. It leads to the activation of the HIF pathway, a cell signalling cascade modulating cellular responses to hypoxia. The HIF pathway has been associated with the expression of markers related to cancer stem cell maintenance [62, 63]. Cancer stem cells have an improved capability for DNA repair, making them more likely to survive an exposure to ionizing radiation and

a likely cause for therapy failures [61].

In addition, hypoxia seems to favor the survival of apoptosis-resistant clones, as p53-deficient cells show a decreased rate of hypoxia-induced apoptosis compared to their non-mutated counterparts [64]. p53 is a protein involved in the induction of apoptosis following irreparable DNA damage.

3.1.4 Assessment of hypoxia and perfusion status using immunofluorescence

Due to its impact on radiation sensitivity, hypoxia has been a focus of radiobiological research during the last decades. The most common approaches for the detection of hypoxia on biological samples involve the use of antibodies. Monoclonal and polyclonal antibodies are a common method to detect and quantify the presence of biological marker proteins and molecules in experiments such as Western Blots, fluorescence assorted cell sorting, immunohistochemistry, and immunofluorescence (IF) microscopy. As IF microscopy was used for the detection of hypoxia on tumor xenografts in this study, the method is described in more detail.

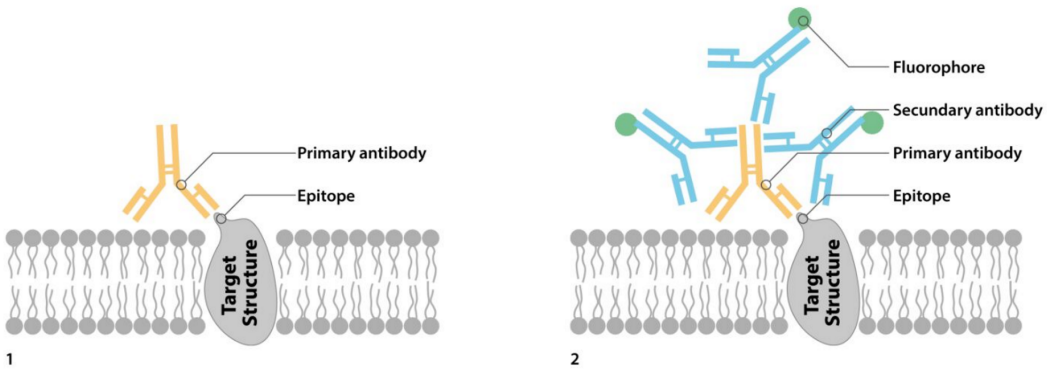

Figure 3.2: The principle of immunofluorescence. The primary antibody binds specifically to the antigen (1), while the secondary antibody carrying the fluorophore binds to the heavy chain of the primary antibody (2). The fluorophore can then be excited and its emission photon detected using a fluorescence microscope.

The principle of the method is outlined in Figure 3.2. Samples, usually derived from cell culture or tisse samples, are fixed on a slide. First, the sample is incubated in a reagent containing an antibody that selectively binds to the selected marker molecule [65]. In the case of hypoxia, this can be an exogeneous marker such as pimonidazole [66], or endogeneous markers, such as the HIF-upregulated proteins CAIX and GLUT-1 [67, 68]. For the staining of blood vessel, surface

proteins specifically expressed on endothelial cells, such as CD31 [69] or podocalyxin [70], are commonly used as marker proteins. Primary antibodies are either monoclonal, e.g. binding to one specific surface structure (epitope) of the target protein, or polyclonal, e.g. binding to multiple epitopes of the same protein. While monoclonal antibodies are usually derived from one single, immortalized cell line in cell culture, polyclonal antibodies are harvested from the serum of exposed animals, and are therefore the product of multiple B-cell clones.

In the second step, the slide is incubated with a reagent containing polyclonal antibodies against the primary antibody. As each secondary antibody is conjugated (labeled) with a fluorophore, the secondary antibody can be detected as the fluorophore will emit photons of a specific wavelength if excited in a fluorescence microscope. Since multiple secondary antibodies bind to each primary antibody, a signal amplification is achieved that increases the sensitivity of immunofluorescence microscopy [65].

Conjugated compounds include fluorescein isothiocyanata (FITC) with an excitation wavelength of 495 nm and an emmision wavelength of approximately 519 nm. Tetramethylrhodamine (TRITC) is another fluorophore, with an excitation maximum of 557 nm and an emission wavelength of 576 nm. The combination of primary antibodies from different species and secondary antibodies with labels of different wavelength can be used to visualize multiple markers on the same slide.

In our study, pimonidazole was used as a marker of hypoxia. It is an exogenenous marker that has to be applied prior to immunofluorescence staining. As a nitroimidazole, it has the same binding reaction as FMISO and other nitroimidazole-based tracers, and has been shown to correlate well with FMISO, FAZA and HX4, as well as endogeneous markers of hypoxa such as CAIX [34].

Perfusion status of the vessels can be assessed through injection of Hoechst 33342. Hoechst 33342 is an organic substance that intercalates with DNA, resulting in staining of the nuclei. If it is injected shortly before tumor excision, only nuclei adjacent to perfused vessels will be stained. The molecule itself is excitable at 355 nm, and emits photons of 465 nm wavelength. Therefore, it does not need antibodies for its detection via fluorescence microscopy.

3.1.5 Consequences for radiotherapy

Not surprisingly, the radiobiological effects induced by hypoxia adversely affect RT treatment efficacy in solid tumors. This has been shown in a number of clinical studies, both for two larger studies that measured tumor oxygen content directly through oxygen probes [22, 71], as well as a number of smaller studies applying PET imaging approaches [17, 18, 33, 72, 73]. Here, hypoxia resulted in higher rates of loco-regional recurrences, distant metastases and cancer-related deaths.

Several approaches to counteract hypoxia-induced radioresistance have been investigated. In the 1970's, several studies have used high-oxygen content gas breathing to increase tumor oxygenation during radiotherapy [74, 75]. Later, ra-

diosensitizers such as nimorazole gained more attention, and combined treatments were also investigated [28]. A meta-analysis of these methods revealed that there is clinical evidence that patients with hypoxic tumors benefit from these modifications, resulting in significantly better treatment outcome with no increase of radiation-induced side effects [76].

An escalation of dose to hypoxic tumors or tumor subvolumes is discussed as an alternative approach to fight hypoxia-induced radioresistance. Several approaches of dose painting have been suggested. The most simple approach is to homogeneously increase the prescibed dose to tumors in which a significant amount of hypoxia has been detected [23]. While this approach is straightforward and easy to apply without placing high demands on the hypoxia imaging modality, it carries the risk of increased side effects due to the higher dose on surrounding normal tissue.

Two alternative approaches include escalating dose exclusively to hypoxic subvolumes, either homogeneously (dose paiting by contours) or adjusted proportionally to the severity of hypoxia detected in each subvolume (dose painting by numbers). Planning studies showed that these approaches are technically feasible thanks to the introduction of IMRT treatment in the clinical routine [30, 31, 77]. However, they both depend on thoroughly validated spatially highly resolved images of hypoxia. As imaging modalities for the detection of hypoxia are still under clinical evaluation, hypoxia-based dose painting has yet to be clinically established.

3.2 Positron emission tomography (PET)

3.2.1 Principles of PET imaging

Positron emission tomography is a functional imaging modality in nuclear medicine. It uses substances labeled with β^+ emitters (tracers) that accumulate if certain metabolic conditions are met. Imaging is done by detection of coinciding photon pairs generated by positron annihilation.

Positron-emitting radioisotopes used for PET imaging include ^{11}C, ^{13}N, ^{18}F, ^{15}O, ^{68}Ga and ^{64}Cu, with half-lifes ranging from a few minutes to several hours. β^+-decay occures in nuclei with a high proton number. The mass of the nucleus will not change, but the charge is decreased by one, as described in the following equation:

$$ {}^{\mathrm{A}}_{\mathrm{Z}}\mathrm{X} \longrightarrow {}_{\mathrm{Z}-1}{}^{\mathrm{A}}\mathrm{Y} + \mathrm{e}^+ + \nu_e $$

The neutrino will leave the patient's body with no relevant interaction and thus plays no further role in tomography. The positron will quickly annihilate with an electron in its vicinity, resulting in the formation of two photons with the energy of 511 keV each. The photons will be emitted in an angle of approximately 180°. Their specific energy and the precise angle as well as their coinciding detection

within a few nanoseconds can be used to reconstruct a line of response (LOR) on which the annihilation event occured.

In PET scanners, this principle is exploited to reconstruct 3D images of the distribution of annihilation events in the body. The scanner contains rings of scintillator crystals and photomultipliers which detect annihilation radiation. The number of possible LORs that can be distinguished is determined by the number of detector panels. The number of incidents on each LOR is directly proportional to the amount of tracer molecules. Image reconstruction such as filtered back projection or iterative approaches such as Maximum Likelihood - Expectation Maximization can be used to obtain an image of tracer distribution in the patient's body [78].

Compared to other medical imaging modalities, PET images have a poor resolution, with a geometric resolution of roughly 4-6 mm in clinical scanners. Even in modern scanners, a much higher resolution cannot be achieved for a number of physical and technical limitations inherent to PET imaging [79]. They include the limited number and finite size of detector panels, scattering of photons and residual impulse of the electron-positron pair resulting in emission angles different from 180°, and multiple coincidences at the same time, resulting in the assignment of wrong LORs. Also, the number of counts is inherently restricted, as only a small fraction of emitted photons is detected as true coincidences and the amount of injected tracer is limited due to its toxicity for the patient.

In the past, PET has been combined with other anatomical and functional imaging modalities. One of them is PET/CT [80, 81]. The approach allows to perform functional PET imaging while acquiring precise, high resolution anatomical information without repositioning of the patient. The additional advantage for radiotherapy is the information on electron density included in the CT scan, which is important for treatment planning. The functional imaging can help in more precise target delineation and early detection of hypoxia [82].

In recent years, systems combining PET and magnetic resonance imaging (MRI), so-called PET/MR scanners, have become commercially available. With this imaging modality, the functional information derived from a PET scan can be acquired together with anatomical as well as functional MR sequences, such as diffusion-weighted MRI [83]. However, electron density for RT treatment planning and attenuation correction cannot be directly deduced from MR scans. This can be overcome either through generation of pseudo-CTs from MR images, which is a subject of on-going research [84, 85], or through deformable registration of a separate CT scan on the MR image [86].

3.2.2 Applications of PET imaging in oncology besides hypoxia imaging

The introduction of PET imaging into the clinical routine has helped to improve cancer treatment in radiotherapy, far beyond the possible detection of hypoxia. PET images can be used for tumor staging, detection of metastasis, tumor delineation and monitoring of treatment success, often with higher sensitivity and

specificity than CT and MRI alone [87]. The most commonly used radioisotope for PET tracers is ^{18}F, as its half life of 109 min is long enough for the tracer to be transported over short distances, which allows PET scans to take place outside of radiopharmacies, but short enough to have a relatively high activity, reducing the amount of tracer that needs to be injected to achieve enough PET detector counts for image reconstruction in a given time frame.

A number of PET tracers have been developed for a variety of indications, often specifically for tumor entities of selected organs. Here, the most commonly used tracers and their indications are described briefly.

The most widely used tracer for clinical oncology is ^{18}F-Fluorodesoxyglucose (FDG). It enters cells through the glucose transport proteins in the cell membrane, where it is phosphorylated by hexokinase in the first step of glycolysis analogous to D-glucose. The phosphorylated FDG can no longer leave the cells. High uptake of FDG indicates high metabolic activity, which is frequently observed in tumor cells, but also organs such as the brain [87, 88]. FDG PET has proven useful in the contouring of tumor volume for RT, where its inclusion led to superior treatment outcomes compared to CT and MRI based contours [89, 90]. Additionally, it has been used for tumor staging in the search for lymph node and distant metastatases for a variaty of tumor entities, including HNSCC [90, 91]. Dose escalation on FDG imaging similar to hypoxia dose painting is also a target of on-going research [92]. As glucose uptake can also be increased in hypoxic regions due to the Pasteur effect [23], correlation with the hypoxia tracer FMISO has been observed in some patients [93].

^{18}F-FET and FDOPA are a possible substitute for FDG in areas where FDG uptake is difficult to interprete as they show a physiologically high glucose uptake, such as the brain. As a derivative of the amino acid tyrosine (FET), or phenylalanine (FDOPA), these tracers show high uptake in neoplasms but low uptake in healthy brain tissue, resulting in a better signal-to-background ratio than FDG. They have recently become clinically established for neuro-oncological indications [94].

^{18}F-FLT as a proliferation marker for highly-proliferating tumors such as lymphoma, where it is used for the monitoring of treatment success. Chemically similar to the DNA component thymidine, it will be incorporated into DNA during replication, thus accumulating in cells undergoing proliferation. High activity in FLT scans indicates high proliferation activity, which is often associated with cancer growth [95].

[^{18}F]fluciclovine is a PET tracer specifically designed for the detection of prostate cancer recurrences, and has shown a higher sensitivity than CT in clinical studies [96]. It is a derivative of the amino-acid Leucine.

3.2.3 PET imaging for the detection of hypoxia

As PET is currently the most promising approach under evaluation for the non-invasive imaging of hypoxia, a number of different hypoxia tracers have been

developed in the last years. Most of these PET tracers are chemical derivates of nitroimidazole labeled with ^{18}F, which were originally developed as radiosensitizers [24]. These molecules are defined by their nitro-group, which is responsible for the retention of the molecule in hypoxic cells, and a variable residual, denoted as R–NO_2. The residuals are lipophilic and allow for free diffusion in tissue. The nitro group can be reduced in a multi-step reduction to an amino group NH_2 by nitroreductases in living cells. Two of these intermediate steps are shown below:

$$\mathrm{R{-}NO_2} \underset{+\,\mathrm{O_2}}{\overset{+\,\mathrm{e^-}}{\rightleftharpoons}} \mathrm{R{-}NO_2{}^{-\bullet}} \xrightarrow{+\,3\,\mathrm{e^-}} \mathrm{R{-}NHOH}$$

These intermediate products are highly reactive and will bind to macromolecules, effectively trapping the tracer inside the cell. In the presence of oxygen, the first step is reversible, and the reactive intermediate product will be quickly oxidized. The molecule will remain in its original cell and retain its ability to diffuse freely [23].

There are many nitroimidazole-based tracers under clinical and preclinical investigations. In this work, we investigated three of them more closely: FMISO, FAZA and HX4. Their chemical structures are shown in Figure 3.3.

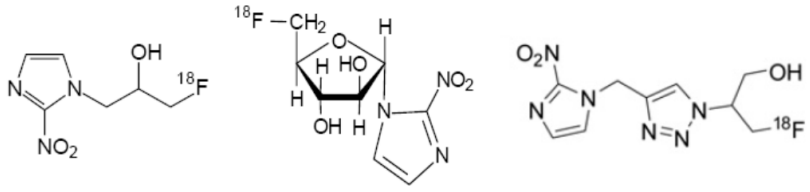

Figure 3.3: Nitroimidazole-based hypoxa PET tracers from left to right: FMISO, FAZA and HX4.

The oldest and best-evaluated hypoxia tracer is ^{18}F-FMISO. It is highly lipophilic, which allows for fast diffusion in tissue, but at the same time limits the elimination of unbound tracer from the tissue, resulting in a poor image contrast [97]. FMISO has been used in several clinical studies, where its usefulness for prognosis was demonstrated. Two strategies for image interpretation have been suggested: while some studies rely on static imaging 2-4 h after tracer administration [18, 33, 73], other studies rely on the analysis of time activity curves (TACs) [27]. For these scans, a dynamic scan is performed for the first 30 min, followed by static scans 2 and 4 h post injection (p.i.). While static scans require less scanning time, making the procedure easier for staff and patient, the inclusion of the perfusion information obtained from the early phases of the dynamic scans allows for differentiation of tissue areas that would be very similar in late static images, and possibly increase the prognostic value.

As a result of its poor image contrast, attempts have been made to develop tracers which have a lower background signal due to faster clearance from the

blood. One of them is FAZA. Like FMISO, it has undergone clinical evaluation by correlating its accumulation to treatment outcome, showing that increased FAZA uptake in static PET scans 2 h p.i. prior to RT indicates a poor prognosis [72]. While FAZA seems to have an increased clearance compared to FMISO, no clinical evaluation of image contrast compared to FMISO exists, and pre-clinical studies are inconclusive [36, 37, 98, 99].

More recently, HX4 has been developed. With its high clearance, it yields superior image contrast in patients when compared to FMISO [35, 100]. Unlike FMISO, a large portion of HX4 is excreted through the kidney, resulting in faster elimination of unbound tracer than through the hepatic route alone [99]. As of now, no study linking HX4 uptake to treatment outcome has been published.

Other nitroimidazole-based tracers include ^{18}F-EF3, ^{18}F-EF5, and ^{18}F-FETNIM. Their imaging characteristics are similar to FMISO, and none of them has been shown to be superior to FMISO in animal experiments, even though it seems that in some cases, less unwanted metabolites are formed in the body [23].

Very recently, another nitroimidazole based tracer,^{18}F-FAZDR, has been presented. Its investigation is on-going, but it performed better than FAZA in a preclinical imaging study [101].

In contrast to the tracers mentioned above, ^{64}Cu-ATSM is not a derivate of nitroimidazole. Its binding mechanism under hypoxic conditions is not completely understood, and it is not certain whether hypoxia is the only metabolic process affecting its retention [23]. Recently, more doubt has been cast on Cu-ATSM as a specific marker of hypoxia, as correlation with the endogeneous hypoxia marker CAIX has been poor compared to nitroimidazole-based markers [34].

An inherent problem of hypoxia PET imaging is its low resolution. The voxel size is often larger than microscopic hypoxic areas, so many small hypoxic volumes will be missed if their volume percentage in the voxel is too small. Additionally, as the volume imaged in one voxel can be very heterogeneous, the resulting PET signal may be difficult to interpret. Further investigation and a better understanding of hypoxia tracer retention dynamics is needed before these imaging modalities can be rountinly established in the clinic.

3.3 Principles of diffusion

3.3.1 Overview

Diffusion describes the net movement of particles from places of high concentrations to regions of low concentrations, i.e. the movement of particles along a concentration gradient. As opposed to the active transport through cell membranes in biological systems, diffusion at constant temperatures is a passive process, as it occurs without additional energy supply. Diffusion is caused by the thermic movement of particles, which has first been observed by Robert Brown [102]. He noticed that small particles such as pollen moved in irregular patterns when suspended in fluids. In the early 20th century, Einstein and Perrin presented ev-

idence that the movement Brown observed was caused by the thermic motion of water molecules which collided with the suspended particles, resulting in random movements of these particles [103, 104].

While the movement of an individual particle is random, Brownian motion can lead to a net flux in one direction. This occurs when the likelihood of a particle moving in one direction is higher than a particle moving in the opposite direction. This is the case when a concentration gradient is present. Here, net flux of particles along the concentration gradient will continue until a homogeneous particle distribution is reached, resulting in an increase of entropy and finally, thermodynamic equilibrium.

Even before the underlying mechanisms of diffusion were known, the laws describing diffusion processes were investigated. Thomas Graham was among the first to investigate diffusion systematically. He could show that the diffusion rate was proportional to the differences in concentration between two regions and that its speed was proportional to temperature [105]. However, it was Adolf Fick, a German mathematician and physiologist, who finally discovered the laws guiding diffusion [106]. These laws are therefore known as Fick's laws. These laws are summarized in the following two subsections. A more detailed description on how they are derived can be found in reference [107].

3.3.2 Diffusion in steady-state systems: Fick's first law of diffusion

Fick's first law describes the diffusive flux of particles going from regions of high concentration to regions of low concentrations, stating that its magnitude is proportional to the concentration gradient. In order for Fick's first law to be applicable, the concentration gradient must remain constant over time, assuming a steady state of particle distribution. For a gradient along one spatial dimension, this law can be described as follows:

$$j = -D \cdot \frac{dc}{dx} \tag{3.1}$$

Here, j is the flux density, e.g. the number of particles passing through an area A orthogonal to the flux direction in a given time interval dt, and D is the diffusion coefficent. This diffusion coefficient is dependent on particle size, viscosity of the solution, absolute temperature and particle charge. For freely diffusing, spherical particles in fluids with a low Reynolds number, the Stokes-Einstein equation can be used to determine the diffusion coefficient D:

$$D = \frac{k_B \cdot T}{6\pi \cdot \eta \cdot r} \tag{3.2}$$

where k_B is the Boltzmann constant, T is the absolute temperature, η is the viscosity, and r the particle radius. This relation is known as the Stokes-Einstein equation.

3.3.3 Diffusion in non-stationary systems: Fick's second law of diffusion

Unlike Fick's first law, Fick's second law is applicable in situations where no steady-state can be assumed. Therefore, particle concentration in these systems must be described not only a function of space, but also as a function of time. Under the assumption of mass conservation, Fick's second law can be derived from Fick's first law 3.1:

$$\frac{\partial c}{\partial t} = -\frac{\partial j}{\partial x} \tag{3.3}$$

For a constant diffusion coefficient D and a one-dimensional concentration gradient, this results in the following equation:

$$\frac{\partial c}{\partial t} = D\frac{\partial^2 c}{\partial x^2} \tag{3.4}$$

The solution of Fick's second law is highly dependent on the choice of initial and boundary conditions. Depending on the chosen conditions, the equation can be solved analytically or numerically.

The three-dimensional case can be described as follows:

$$\frac{\partial c}{\partial t} = D\nabla^2 c \tag{3.5}$$

Commonly, this equation is solved numerically. The approached used in this thesis will be described in detail in section 3.4.3. Fick's second law is also known as the diffusion equation. As Fick himself already realized, the laws guiding diffusion and heat conduction are essentially identical, making the diffusion equation an equivalent of the heat equation.

3.4 Biophysical modelling of tumor hypoxia and hypoxia tracer accumulation

3.4.1 Overview

In this thesis, the accumulation of FMISO in tumors was mathematically simulated based on the tumor microvasculature. The most common approach is to divide the simulation into two steps. First, a steady-state oxygen diffusion and consumption is modeled. The oxygen distribution simulated in the first step is used as an input to calculate tracer binding rates, which is followed by a simulation of tracer diffusion and retention.

First introduced by Kelly and Brady [38], a similar approach of FMISO simulations was used in a number of later studies [39–41, 43, 45]. Additionally, many models to describe oxygen distribution have been published, both in 2D [108,109], and more recently also in 3D [70, 110–112]. Frequently, artificial 2D vessel maps have been used for these simulations, particularly in the older studies [38,43]. The use of 2D vessel maps derived from tumor microsections was first introduced by

Mönnich *et al* [39]. In the last years, several 3D simulations of oxygen have been published [70,110–112]. With one exception [110], all these models use 3D vascular maps derived from tumor vasculature. Only one 3D simulation of FMISO has been published so far, which uses artificial vessel maps [45]. All simulations are solved numerically, using finite difference [38] and finite element methods [39], or convolution-based approches [45, 70, 112]. In the following section, the methods used in this work for the simulations of oxygen and tracer distributions will be described in more detail. The generation of vessel maps and the numerical methods are discussed, as well as the choice of parameters. While a continuation of their work, many of methods presented here differ from those introduced by Mönnich *et al*, such as the inclusion of perfusion status for the vessel map generation and the extension of the model to three dimensions.

3.4.2 Generation of tumor vessel maps

Generation of 2D vessel maps from HNSCC tumor microsections

In part III of this thesis, vessel maps from Mönnich *et al* were used. Their generation is outlined in [113]. Microsections from HNSCC tumor xeongrafts were labelled for blood vessels using immunofluorescence against the endothelial marker 9F1, and scanned with a resolution of 2.67 μm, as described previously [114, 115].

Gray-scale images of the vasculature were bilaterally filtered to reduce noise and preserve edges. Images were then thresholded to create binary images. Threshold values were determined according to the background noise level in avascular regions.

These vessel maps are not suitable for validation as they did not exclude unperfused vessels due to a missing perfusion staining. However, these vessel maps showed highly heterogeneous levels of perfusion, ranging from densely perfused tissue to virtually avascular regions, which was an advantage in the setup of the study presented in part III.

Generation of 2D perfused vessel maps

In part I, a method was used to include additional information on vessel perfusion status. The images used for this part of the work were kindly provided by the OncoRay Center, Dresden.

The method is shown in Figure 3.4. Sections from HNSCC tumor xenografts were immunofluorescently labelled for endothelial marker CD31 and hypoxia marker pimonidazole. Hoechst 33342 had been applied prior to tumor excision. Images were scanned at a resolution of 1.02 μm and stained with hematoxylin and eosine (HE). The HE stainings were used to draw masks including only vital tumor tisse. The methodology is described in detail by Yaromina *et al* [69].

For the generation of the vessel maps, we used the information contained in the CD31 and Hoechst image to include only perfused vessels. The vital tissue

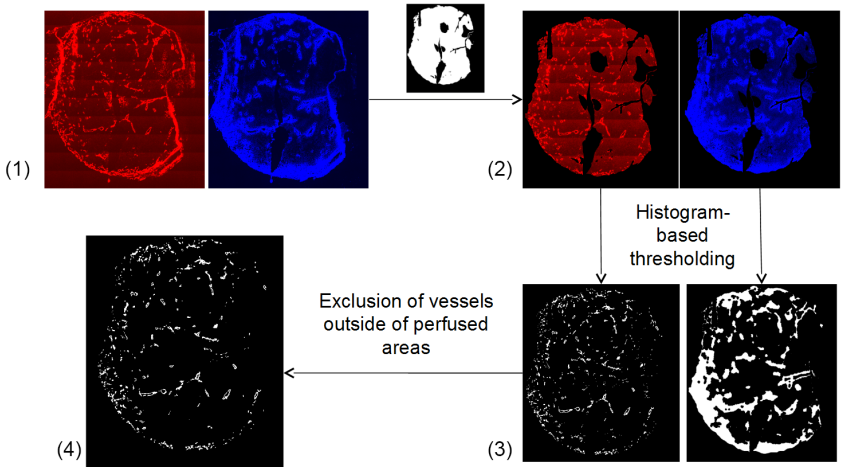

Figure 3.4: Inclusion of perfusion status to the final vessel map: (1) Raw fluorescence images of endothelial marker CD31 and perfusion marker Hoechst 33342 are cut to contain only vital tumor tissue (2). (3) A histogram-based thresholding is performed to obtain binary images of vasculature and perfusion. (4) All vessels located outside of perfused areas are excluded.

mask was applied to include only vital tissue and both images were thresholded to obtain binary images of vascularization and perfusion status. The threshold was determined based on the histogram shape of the background signal. A morphological opening filter was applied to reduce noise. For Hoechst images, a morphological closing operation was performed to include areas outside of the nuclei, as nuclei are the only cellular structures that retain Hoechst. The processed images were then multiplied in a pixel-by-pixel fashion to obtain a vessel map that contains only vessels inside perfused areas.

Generation of 3D perfused vessel maps

Although the methodology is similar to generating a 2D vessel map, obtaining 3D vascular structures is far more challenging. There are two methods that can potentially be used for this.

The first approach is confocal microscopy. Confocal microscopy allows to focus on one z-plane of the sample while excluding light from other planes of the sample. By changing the focal plane, samples can be scanned in the z-direction, resulting in a 3D image stack of the sample [116]. This method is very appealing for a number of reasons: It yields a highly-resolved, perfectly registered 3D image stack, is very time-efficient due to automatisation and requires no further cutting of the sample. This method has been used by Grimes *et al* [112] for the generation of 3D vessel maps, with excellent results. However, it comes with one major pitfall: the depth from which signal can be detected is limited, both due to sperical abberations, absorption of photons and diffusion limitations of the antibodies in

the tissue. While samples with thicknesses of over 100 μm can now be easily imaged [117], samples with a thickness of over 1 mm cannot be imaged with this method. However, oxygen in tissue can easly diffuse over 100 μm, making it advisable to use thicker samples to avoid edge effects. Additionally, the PET voxel size of the validation scans we used was $0.7 \times 0.7 \times 0.8$ mm^3, using vessel maps of at least that size and a large fraction of the tumor is recommended to make results comparable.

The approach used in this work is tedious and time consuming. Snap-frozen tumor xenografts injected with pimonidazole and Hoechst 33342 prior to excision are cut into sections of 10 μm each, with a total of 120 sections per tumor, and stained and imaged as described above. After scanning, images are manually registered, first rigidly and then deformably. This is necessary to reduce deformations introduced during the cutting and fixation process of each section. Then a mask is drawn based on HE and fluorescence signal and thresholding of CD31 and Hoechst images is performed as described above. The so reconstructed 3D vessel map is a close representation of the real tumor vasculature. This approach has the disadvantage of introducing cutting artefacts to the final map and is more time consuming. However, it allowed for the reconstruction of relatively large tumor volumes of 3x3x1.2 mm^3, which can be reasonably compared against PET time activity curves obtained from the same tumor.

3.4.3 Numerical methods for the simulation of reaction-diffusion processes

The diffusion of oxygen and tracers can be analytically solved in simple geometries according to the diffusion equation. Assuming the diffusion coefficent D to be constant, this equation reduces to the following linear differential equation:

$$\frac{\partial c(r,t)}{\partial t} = D\nabla^2 c(r,t). \tag{3.6}$$

Effectively a form of Fick's second law of diffusion, it describes the diffusion of a substance with a concentration $c(r,t)$ along a concentration gradient over a time t, depending on location $r = \sqrt{\sum_{i=1}^{n} x_i^2}$, with n being the number of dimensions. This equation can still be solved analytically. However, as the model has to take oxygen consumption and tracer binding into account, each voxel simultaneously has to act as a source and sink, Eq. 3.6 changes to:

$$\frac{\partial c(r,t)}{\partial t} = D\nabla^2 c(r,t) - R(c(r,t)). \tag{3.7}$$

with R being a consumption factor dependent on substance concentration. Here, a numerical approach to solve the problem is necessary.

The work presented here is a continuation of the work performed by Mönnich *et al* [39–41]. It applied a 2D finite element method (FEM) approach for the solution of this parabolic partial differential equation (PDE), and was implemented

in MATLAB. However, for the extension of the model to 3D, an increase of computational efficiency was necessary, which was done by changing the numerical method to a kernel-based approach.

The approach we chose is outlined in Lagerlöf *et al* [70], where the authors describe an oxygen-simulation model implemented in 3D. Their method employs Green's function, a description of how a δ-function propagates in space. For the diffusion equation, Green's function is Gaussian, the fundamental solution of the diffusion equation. For an n-dimensional problem, the solution kernel is as follows:

$$c(r,t) = k \cdot t^{-\frac{n}{2}} \cdot \mathrm{e}^{\frac{r^2}{4D \cdot t}}. \tag{3.8}$$

It describes the concentration at time t and at a distance $r = \sqrt{\sum_{i=1}^{n} x_i^2}$ from a point source, where D is the diffusion coefficient, and k is a normalization factor meeting the following condition:

$$\int_0^\infty c(r,t)dr \equiv 1. \tag{3.9}$$

With this approach, each voxel is treated as a source of oxygen, with its strength depending on local oxygen partial pressure (pO_2). Convolution with the Gaussian kernel will spread the oxygen over neighboring voxels without changing the total amount of oxygen present. The underlying assumption of this approach is that the pixels can be regarded as point sources. Resolutions ranged from 5-10 μm. As this is much smaller than the distance from hypoxic regions, this was judged to be a valid assumption [45, 70].

The convolution was applied using the built-in MATLAB function *imfilter*, as it was faster than a 3D fast fourier transform and subsequent multiplication in the fourier space. Additionally, a Gaussian filter is separable, meaning that a 3D filter can be replaced by filtering each dimension with a onedimensional filter. This approach further reduces computation time.

Pure diffusion out of a blood vessel at any time point t and number of dimensions n can be modeled in a single convolution step using the appropriate kernel. However, in this case, the model is run repeatedly with small time steps Δt. Between each step, the substance concentration c was reset inside the blood vessels to model continuous substance supply through the blood. The approach is visualized in Figure 3.5. Additionally, between each step, substance reaction (comsumption for oxygen and irreversible binding for tracers) can be substracted from the concentration of free diffusible substance c. Unlike previous models, the model does not include boundary conditions at the blood vessel walls. At the edges of the vessel maps, the map was mirrored, effectively resulting in a Neumann boundary condition as the concentration gradient is set to 0.

3.4.4 Modelling of oxygen transport and consumption

The reaction-diffusion equation used for the modelling of this simulation has been described above in Eq. 3.7. Here, P is the local oxygen partial pressure. Typi-

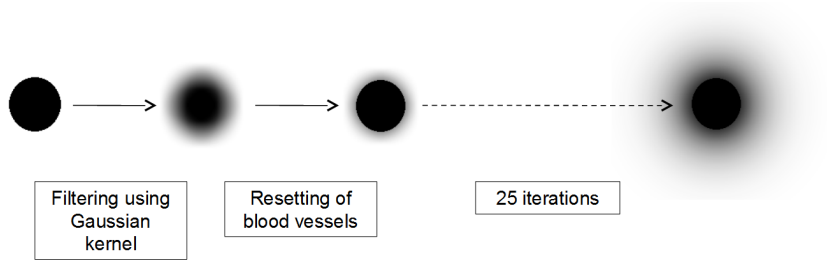

Figure 3.5: Modelling diffusion and substance supply of a blood vessel through iterative filtering with Gaussian kernel and subsequent resetting of concentration within blood vessels.

cally, as oxygen diffuses freely through cellular membranes, a constant diffusion coefficient D_{O_2} for both intra- and extracellular space is assumed. With a consumption term $M(P)$, the reaction-diffusion model for oxygen is described as:

$$\frac{\partial P}{\partial t} = D_{O_2}\nabla^2 P - M(P). \tag{3.10}$$

The cellular oxygen consumption rate $M(P)$ is a non-linear function of oxygen partial pressure in tissue. It is typically modelled as a Michaelis-Menten kinetic [118], which is the common model used to describe substance-dependence of biochemical processes involving enzymes [119]. For the consumption of oxygen, the equation is described as:

$$M(P) = \frac{M_0 P}{P + P_0}. \tag{3.11}$$

Here, M_0 is the maximum oxygen consumption rate, meaning that for high values of oxgen partial pressure P, the function will asymptotically approach M_0. Half-maximal consumption rate is reached at an oxygen content of P_0. The function is plotted in Figure 3.6 below, and the simulated oxygen distribution for a single blood vessel with a diameter of 50 μm is shown in Figure 3.7.

3.4.5 Modelling tracer transport and consumption

Similarly, modeling of tracer diffusion and irreversible tracer binding can be performed using the same reaction-diffusion equation given in Eq. 3.7. Here, the tracer diffusion coefficient D_T is also assumed to be constant in tissue, as nitroimidazoles are lipophilic organic substances that can pass cell membranes quite easily. However, these diffusion coefficients are different for each tracer. Their determination is described below in Section 3.4.7. The second term is the irreversible binding of free tracer. The reaction-diffusion equation for tracer binding

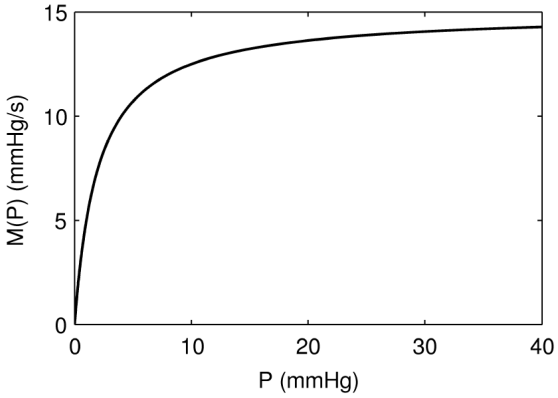

Figure 3.6: Michaelis-Menten kinetic of oxygen consumption with M_0 of 15 mmHg/s and P_0 of 2.0 mmHg. Courtesy of D. Mönnich, University Hospital Tübingen

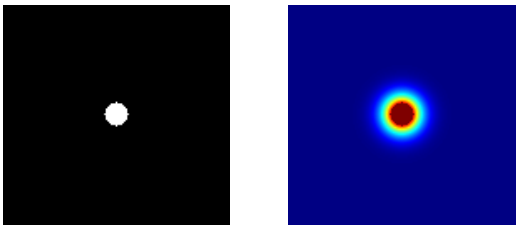

Figure 3.7: A simple vessel maps containing a blood vessel with a diameter of 50 μm, and the resulting simulated oxygen distribution on the right. The color map indicates pO_2 ranging from 0 mmHg (blue) to 40 mmHg(red)

is expressed as two coupled partial differential equations:

$$\frac{\partial C_f}{\partial t} = D_T \nabla^2 C_f - \frac{\partial C_b}{\partial t} \tag{3.12}$$

with C_f as the concentration of free tracer and C_b being the concentration of bound tracer. As the tracer binding rate is a function of local oxygen partial pressure, it can also be referred as:

$$\frac{\partial C_b}{\partial t} = K(P) C_f. \tag{3.13}$$

This equation shows that tracer binding at a specific location is directly proportional to the concentration of free tracer at that location. The reaction rate $K(P)$ includes two multiplicative effects, $F_1(P)$ and $F_2(P)$:

$$K(P) = F_1(P) \cdot F_2(P). \tag{3.14}$$

This model of tracer binding has been developed and described in detail by Mönnich *et al* [39]. The first effect, $F_1(P)$ models the increasing binding rate of nitroimidazole tracers with decreasing oxygen partial pressure:

$$F_1(P) = \frac{K_{max} P_1}{P + P_1}. \tag{3.15}$$

Similar to a Michaelis-Menten kinetic, K_{max} is the maximum binding rate, while the half-maximum binding rate is reached at an oxygen partial pressure of P_1. However, reduction of nitroimidazole-based tracers can take place only in vital cells as it is dependent on a functional cellular metabolism. Therefore, tracer uptake will be lowered in regions where hypoxia is severe enough to induce necrosis. The second effect, $F_2(P)$, models this relationship. It is close to 1 for high oxygen partial pressure, but drops to 0 for a specified value P_2:

$$F_2(P) = (\frac{P}{P + P_2})^k. \tag{3.16}$$

The parameter k determines the step width at P_2.

$F_1(P)$, $F_2(P)$ and the resulting $K(P)$ are shown in Figure 3.8 below. As in the

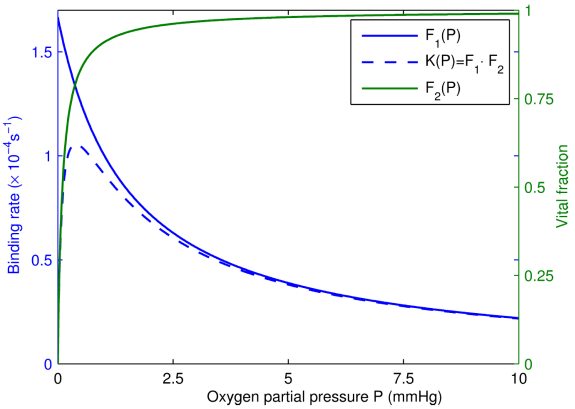

Figure 3.8: $F_1(P)$, $F_2(P)$ and the resulting $K(P)$, with parameter values of $K_{max} = 1.7 \times 10^{-4}$ s^{-1}, $P_1 = 1.5$ mmHg, $P_2 = 0.1$ mmHg, and $k = 0.3$. Courtesy of D. Mönnich, University Hospital Tübingen

oxygen simulation, free tracer is supplied via the blood vessels. But in contrast to the oxygen simulation, where the blood vessels are reset to a constant value, the tracer concentration changes over time as the tracer is washed in and later cleared from the blood stream. The amount of free tracer concentration inside the blood vessels (C_{iv}) is modelled according to the following function:

$$C_{iv}(t) = A_1 \mathrm{e}^{\frac{-t}{\tau_1}} + A_2 \mathrm{e}^{\frac{-t}{\tau_2}}. \tag{3.17}$$

This equation is a sum of two exponential functions. The first part with time constant τ_1 describes the wash-in, e.g. the tracer distribution in the body immediately after injection. This is followed by a slow wash-out with time constant τ_2, caused by the tracer elimination through excretory pathways. A_1, A_2, τ_1 and τ_2 are fit parameters that were determined from dynamic hypoxia PET scans. The fitting approach and results are outlined in Section 3.4.7. A simulation result for the same vessel at imaging times of 5, 30, 60, and 90 min is shown in Figure 3.7 is shown in Figure 3.7.

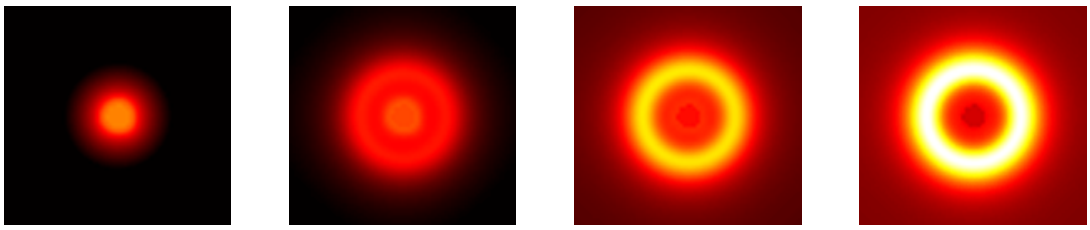

Figure 3.9: Simulation results of FMISO accumulation for imaging times of 5 min, 30 min, 60 min and 80 min (from left to right). Colors indicate activity concentrations ranging from 0 (black) to 500 kBq/ml (white).

3.4.6 Limitations and simplifications of the method

This simulation model works with a number of assumptions and simplifications which might not always model reality accurately. Here, we will briefly discuss some of these limitations and how they may impact the simulation results.

One assumption is that the diffusion coefficient D is homogeneous in tissue, and that the tracer will diffuse freely in extra- and intracellular space. While it is true that lipophilic compounds such as FMISO can easily pass through cellular membranes, effectively resulting in a rather homogeneous diffusion coefficient, this assumption might not hold true for more hydrophilic tracers such as FAZA. Moreover, the studies by Pruijn *et al* [120, 121] showed that diffusion coefficients for pharmaceutical compounds can differ drastically between different cell lines, which might be a result of varying cell size and density. As tumor tissue is often heterogeneous, it is likely that the diffusion coefficient for hypoxia PET tracers will show large variations within one tumor sample.

As described above, the use of Green's function for the simulation of diffusion processes assumes that each pixel can be regarded as a point source. Therefore, the resolution of the simulation is critical and should be as high as possible to approximate this assumption. It is critical that the diffusion kernel used for each iteration is large compared to the pixel size of the simulated tissue. Therefore, we used pixel sizes of no more than 5 μm for the oxygen simulations and 10 μm for the tracer simulations. These resolutions present a compromise between simulation accuracy and computational efficiency, and are in line with or even smaller than resolutions used in previously published studies [45, 70]. A higher

resolution for the oxygen simulations was recommended due to the smaller time steps Δt of 10 ms used for this step of the simulation, as opposed to Δt of 1 s for the tracer simulations.

Another simplification is the assumption of a homogeneous blood pO_2. In reality, oxygen content in the blood vessel is highly variable, ranging from about 100 mmHg for arterial blood to about 30 mmHg for venous blood. The value of 40 mmHg is the approximate value observed in tumor capillaries and has been used in previous publications [39, 108, 122]. However, blood vessel content can differ from this average value for individual vessels, which in turn affects the resulting oxygen distribution in tissue. The only means we had to counteract this effect was to exclude dysfunctional vessels based on Hoechst perfusion stainings as described above, effectively assigning them a pO_2 of 0 mmHg. Unfortunately, there is no realiable method to determine blood oxygen content in capillaries after tumor excision. Therefore, we had to rely on the homogeneous value of 40 mmHg as an approximation.

3.4.7 Parameter values

Many of the parameters that were used in ths study are equivalent to those used by Mönnich *et al* [39]. Throughout the course of this study, some parameters were changed, either due to the study design or because new experimental, more reliable parameter values were published in the meantime. In the following sections, we will outline which parameters stayed constant throughout this work, and which changes were made to the model and why.

Parameters of oxygen transport and consumption

Table 3.1: Table of oxygen parameters that were used for all simulations

Symbol	Meaning	Value	Reference
P_{RBC}	Typical pO_2 in erythrocytes	40 mmHg	[122]
D_{O_2}	O_2 diffusion coefficient	$2 \times 10^{-9}\,\mathrm{m}^2/\mathrm{s}$	[123]

The parameters in Table 3.1 were used for all simulations. Taken from Mönnich *et al* [39], they are based on experimental measurements made in other studies.

For the preliminary 2D validation presented in part I, parameter M_0 was optimized over its entire literature range for optimum correlation of simulation results with pimonidazole stainings. As shown in the results section of part I, it is dependent on the investigated cell line and by far the most powerful parameter.

In part I, P_0 was also changed to the only available *in vivo* value at the time, obtained from sea urchin eggs, while the previous standard value was an optimum value derived from oxygen simulations. Lately, a new experimental study using

Table 3.2: Standard parameters and literature ranges for maximum oxygen consumption rate M_0 and Michaelis-Menten coefficient P_0

Symbol	Meaning	Standard	Reference	Literature range	References
M_0 (mmHg/s)	Max. O_2 comsumption rate	15	[108]	2.7 - 11.1 (in vivo) 8.6-33.5 (in vitro)	[124] [123, 125]
P_0 (mmHg)	Michaelis-Menten coefficient	2.0	[118]	0.5-2.5 (in silico) 4.8(in vitro)	[108, 118] [126]

cancer cell spheroids has confirmed that the standard Michaelis-Menten coefficient is within the range of their experimental data [45]. Its impact on the simulation results is much smaller than for M_0.

In parts II and III, the standard values listed in Table 3.2 were used.

Parameters of tracer diffusion and retention

Table 3.3: Table of tracer parameters taken from Mönnich et al. [39] that were used for all simulations

Symbol	Meaning	Value	Reference
P_1	pO_2 inhibiting binding by 50%	$(0.8 - \mathbf{1.5})$ mmHg	[127]
$K_{\max}$	Max. binding rate (anoxia)	$1.7 \times 10^{-4}\,s^{-1}$	Optimised
P_2	pO_2 inducing 50% necrosis	0.1 mmHg	Simulated pO_2 120 µm from vessels
k	Determines step width at P_2	0.3	Optimised

While Mönnich *et al* [39] used a published diffusion coefficient for misonidazole [128] to model FMISO diffusion, the approach in this work is different. Pruijn *et al* [120, 121] developed a model to predict the diffusion coefficent of organic substances through multicellular membranes based on their partition coefficent and their molecular weight. We used their model to estimate tracer diffusion coefficients on the respective tracers' chemical properties.

These input values were taken from the PubChem database or published literature values, except for the partition coefficient of FAZA, where published literature values varied by several orders of magnitude [36, 37, 98, 129]. Instead, the partition coefficient for FAZA was determined using the simulation softwares XLOGP3, ALOGPS 2.1, Molinspiration and LogKow [130–132], and taking the average over these simulation results as suggested in [133]. The input for this prediction and the result is listed in Table 3.4 below.

The maximum binding rate of FMISO, K_{max}, was first established by Mönnich *et al* through optimization. Lately, a new value has been experimentally estab-

Table 3.4

Symbol	Meaning	FMISO	FAZA	HX4	References
M	Molecular weight	189.14	247.18	269.22	PubChem database
P	Partition coefficient	0.41	0.30	0.2	[100, 134–136]
D_T ($\times 10^{-11}$ m^2/s	Diffusion coefficient	7.90	2.99	3.55	[120, 121]

lished from data obtained in cell spheroids [45]. Therefore, the parameter value was changed accordingly from 1.7×10^{-4} s^{-1} to 4.4×10^{-4} s^{-1} for part II of this work.

Determining blood input functions for FMISO, FAZA and HX4

For part III, blood input functions were determined from clinical dynamic hypoxia PET scans using the respective tracers (FMISO: n = 10, FAZA: n = 3, HX4: n = 5). For each scan, a region of interest (ROI) with a size of six voxels inside the heart or a major blood vessel was determined. Patients were 57-71 years old and suffered from HNSCC (FMISO, FAZA) or non-small cell lung cancer (HX4).

For the FMISO and FAZA groups, imaging was performed at the University Hospital Tübingen in a GE Advance Scanner (GE Medical Systems, Milwaukee, WI, USA), with a slice thickness of 4.25 mm and a pixel spacing of 4.3 mm. Reconstruction was performed using OSEM 2D with four iterations and eight subsets, and a scatter correction (convolution subtraction) was applied.

HX4 patients were imaged at MAASTRO Clinic, Maastricht, The Netherlands in a Philips Gemini TF 64 PET/CT scanner (Philips Healthcare, Best, The Netherlands). The axial field of view was set to 18 cm, with a slice thickness of 4 mm and a spatial resolution of approximately 5 mm full-width at half maximum (FWHM). Image reconstruction was performed using a 3D ordered-subset iterative time-of-flight reconstruction technique (BLOB-OS-TF) with three iterations and 33 subsets. Attenuation correction and scatter correction (SS-SIMUL) were performed.

From these images, tracer concentration in the blood ROI was determined at 20-45 time points over a period of 4 hours post-injection (p.i.). These values were fitted to Eq. 3.17. The average input function (AIF) was determined by taking the average over all scans from the same patient group for each parameter. The results are listed in Table 3.5 below.

For part II, the input function was determined by fitting the average input function (Eq. 3.17) to activity from well-perfused muscular tissue. This was done as a substitute because the heart was outside of the field of view, and the activity in well-perfused tissue with excellent arterial blood supply is expected to closely follow the arterial blood activity.

Table 3.5: Average input functions for FMISO, FAZA and HX4 as determined from clinical PET scans

Tracer	A_1 (kBq/ml)	τ_1 ($\times 10^{-3}$ s^{-1})	A_2 (kBq/ml)	τ_2 ($\times 10^{-5}$ s^{-1})
FMISO	18.11 ± 7.08	2.0 ± 0.71	10.92 ± 2.49	1.90 ± 1.55
FAZA	13.10 ± 4.50	1.30 ± 0.60	13.1 ± 3.70	4.27 ± 1.51
HX4	33.55 ± 12.81	3.10 ± 0.94	12.31 ± 3.27	11.78 ± 5.75

3.4.8 Validation

Validation of such a model is extremely difficult, and very few validation attempts have been made in the past. One of them was performed by Mönnich *et al* and is outlined in [39, 113]. They could show that accumulation of simulated FMISO uptake roughly matches the accumulation of pimonidazole stainings and that simulated median oxygen partial pressure and oxygen distribution is similar to the oxygen content of HNSCC observed *in vivo* [113, 123, 137]. Furthermore, simulated TACs using this model agreed with those observed in clinical PET scans.

Additionally, another approach presented by Bowen *et al* [44], which is based on electrochemical modelling of FMISO binding reactions, demonstrated that their simulated oxygen histograms agree with measurements of oxygen content using invasive probes.

However, for a full validation of the model, it is necessary to verify that the results agree both microscopically and macroscopically, meaning that the model must be able to simulate spatial tracer activity on the microscopic cellular level as well as time-activity curves and retention dynamics observed in macroscopic PET scans, preferably for the same vascular model. Data for such a validation is difficult and time-consuming to obtain, and has therefore not been attempted until now.

Microscopic validation using pimonidazole stainings

Pimonidazole is a nitroimidazole-based marker of hypoxia. Therefore, it shows similar biochemical properties and the same binding reaction as clinically studied hypoxia PET tracers. In experiments, it could be shown that it correlates well with FMISO, FAZA and HX4 as well as endogeneous markers of hypoxia [34, 67, 68, 138]. We therefore chose pimonidazole as a gold-standard validation for the microscopic distribution of hypoxia tracers.

In part I, we validated the simulation results by downsampling the resolution of both simulation and pimonidazole staining results to 50×50 μm^2 and determining Pearson correlation coefficent R and the resulting coefficent of determination R^2. The choice of parameters was considered optimal for maximum R^2. Only vital tumor tissue was included in the analysis.

In part II, the approach was altered. Pimonidazole images were manually contured to obtain binary images of the tumor distinguishing between hypoxia-positive and negative regions. For the simulations, a fixed threshold was set which was set to be half-way between minimum and maximum activity. Simulation performance was evaluated by determining sensitivity and specificity, as well as how far away false-positive voxels were placed from true-positive regions (distance-to-agreement (DTA)). Again, only vital tumor tissue was included in the analysis.

Macroscopic validation against PET measurements of the same tumor sample

For the macroscopic validation, experimental TACs obtained from a small animal PET (Bruker, Ettlingen, Germany) were used. A 90 min dynamic FMISO PET/MR scan was performed on tumor-bearing female nude mice (NMRI nu/nu, Charles River Laboratories) carrying HNSCC tumor xenografts (FaDu). Animals were injected with pimonidazole (Hypoxyprobe, Burlington, USA) and Hoechst 33342 (Sigma Aldrich, Deisenhofen, Germany) 1 h and 1 min before tumor excision, respectively. After excision, tumors were snap-frozen and used for vessel map reconstruction as described in Section 3.4.2. This way, we were able to obtain vessel maps for which an FMISO PET scan was available.

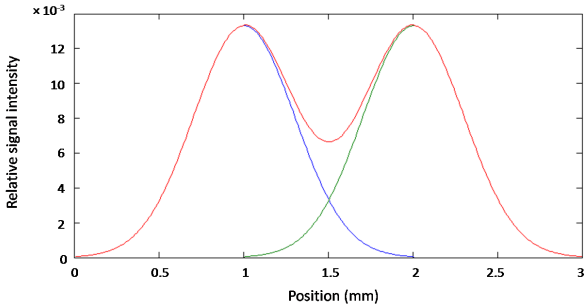

Figure 3.10: Filtering of two point sources (blue and green) located at 1mm and 2mm on the x-axis with a Gaussian filter used to approximate the blurring induced by the point-spread function of the PET scanner. σ was set to 300 μm, resulting in a resolution of approximately 1mm (red).

PET time-activity curves were determined inside a ROI drawn to include the entire tumor. Corresponding activities were simulated on the generated vessel map. However, these results are not directly comparable, as the point-spread function (PSF) of the scanner will result in a convolution of raw PET signal with said PSF. In order to make simulation and PET scans comparable, a convolution of the simulation results with the scanner PSF is necessary.

Unfortunately, the scanner PSF is not known, and likely to change over the field of view. It is influenced by a number of physical and technical aspects, such as the range of the emitted β^+ particles, the number and size of detector

elements and the size and distance of the imaged object to the center of the field of view [79]. We therefore had to approximate the PSF using a Gaussian function with a standard deviation σ of 300 μm and FWHM of 720 μm based on what we knew about voxel size ($0.7 \times 0.7 \times 0.8$ mm) and resolution (approximately 1-1.2 mm). This folding kernel is shown in Figure 3.10.

The assumption for the convolution of the simulation results was that surrounding tissue had normoxic activity taken from the input function to avoid folding with empty space. In Figure 3.11, the impact of the convolution on raw simulated signal is shown. One can clearly see that overall activity is decreased and spread more smoothly due to the signal contribution of normoxic areas outside of the tumor. In the figure, connective tissue and necrotic areas were removed using the tissue mask generated from HE stainings for better visibility. In this case, simulated signal from necrotic areas was not removed from the simulation results as there was no way to eliminate it from the PET scan. Due to an application error during one of the PET scans, a functional TAC was available for only one tumor.

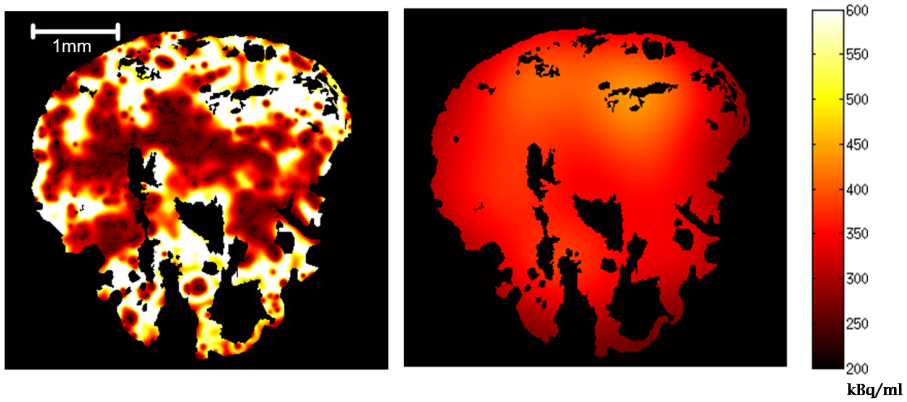

Figure 3.11: 3D simulation results for an HNSCC xenograft tumor (FaDu) before and after filtering with a Gaussian point-spread function ($\sigma = 300\mu$m) used to imitate the blur caused by the PET scanner. This tumor was part of the study presented in part II.

4 Part I: Correlation of FMISO simulations with pimonidazole-stained tumor xenografts: A question of O_2 consumption?

Linda J. Wack[1], David Mönnich[1,2,3], Ala Yaromina[4,5], Daniel Zips[2,3,6], Michael Baumann[2,3,4,7,8], Daniela Thorwarth[1]

[1] Section for Biomedical Physics, Department of Radiation Oncology, University Hospital Tübingen, Germany
[2] German Cancer Consortium (DKTK),Tübingen, Germany
[3] German Cancer Research Center (DKFZ), Heidelberg, Germany
[4] OncoRay - National Center for Radiation Research in Oncology, Faculty of Medicine and University Hospital Carl Gustav Carus, Germany
[5] Department of Radiation Oncology (MAASTRO), GROW - School for Oncology and Developmental Biology, Maastricht, The Netherlands
[6] Department of Radiation Oncology, University Hospital Tübingen, Germany
[7] Department of Radiation Oncology, Faculty of Medicine and University Hospital Carl Gustav Carus, Dresden, Germany
[8] Institute of Radiooncology, Helmholtz-Zentrum Dresden-Rossendorf, Dresden, Germany

published in
Medical Physics 2016, 43: 4113-4121 [139]

Abstract

Purpose. To compare a dedicated simulation model for hypoxia PET against tumor microsections stained for different parameters of the tumor microenvironment. The model can readily be adapted to a variety of conditions, such as different human head and neck squamous cell carcinoma (HNSCC) xenograft tumors.
Material and methods. Nine different HNSCC tumor models were transplanted subcutaneously into nude mice. Tumors were excised and immunofloures-cently labeled with pimonidazole, Hoechst 33342, and CD31, providing information on hypoxia, perfusion, and vessel distribution, respectively. Hoechst and CD31 images were used to generate maps of perfused blood vessels on which tissue oxygenation and the accumulation of the hypoxia tracer FMISO were mathematically simulated. The model includes a Michaelis–Menten relation to describe the oxygen consumption inside tissue. The maximum oxygen consumption rate M_0 was chosen as the parameter for a tumor-specific optimization as it strongly influences tracer distribution. M_0 was optimized on each tumor slice to reach optimum correlations between FMISO concentration 4 h postinjection and pimonidazole staining intensity.
Results. After optimization, high pixel-based correlations up to $R^2 = 0.85$ were found for individual tissue sections. Experimental pimonidazole images and FMISO simulations showed good visual agreement, confirming the validity of the approach. Median correlations per tumor model varied significantly ($p < 0.05$), with R^2 ranging from 0.20 to 0.54. The optimum maximum oxygen consumption rate M_0 differed significantly ($p < 0.05$) between tumor models, ranging from 2.4 to 5.2 mm Hg/s.
Conclusions. It is feasible to simulate FMISO distributions that match the pimonidazole retention patterns observed in vivo. Good agreement was obtained for multiple tumor models by optimizing the oxygen consumption rate, M0, whose optimum value differed significantly between tumor models.

4.1 Introduction

As tumor cell hypoxia reduces radiation sensitivity compared to normoxic cells [21], it is a negative prognostic factor in anticancer treatment approaches including radiotherapy (RT) [22, 23]. Therefore, its identification and quantification is a subject of on-going research, as it is a requirement for future individualized RT adjustments aimed at counteracting hypoxiainduced radioresistance. This is important to help increase local tumor control and hopefully survival in patients with highly hypoxic tumors. Possible treatment approaches include increasing tissue oxygenation during therapy by breathing high oxygen content gas [76] the administration of radiosensitizers that selectively target hypoxic cells [140], or escalating the delivered radiation dose to the GTV [23, 141] or hypoxic parts of the tumor. This last approach is often referred to as dose painting [142]. Due to the high-precision RT techniques developed in recent years, such an approach could easily be implemented in clinical practice as soon as its benefits for the patients are conclusively shown [31, 143].

All these methods, however, require a quantification of hypoxia prior to treatment, as research indicates that patients with hypoxic tumors may benefit the most from these treatment modifications. Particularly for dose painting,a precise 3D spatial quantification of hypoxia is necessary for individualized RT treatment planning. The gold-standard for measuring hypoxia, the oxygen probe, is invasive and does not give 3D images of O_2 distribution [23]. A noninvasive alternative is the use of dedicated tracers for positron emission tomography (PET) which accumulate specifically in hypoxic tissue areas,and have the potential to provide a spatially resolved surrogate image of tissue oxygenation. Possible tracers include [18F]-fluoromisonidazole (FMISO) [18, 144, 145], [18F]-fluoroazomycinarabinoside (FAZA) [72, 146], and [18F]-flortanidazole (HX4) [35, 136], which are [18F]-labeled nitroimidazole compounds, and 64Cu(-II)-diacetyl-bis(N4- methylthiosemicarbazone (Cu-ATSM) [147].

Up to now, many factors influencing hypoxia tracer retention and binding dynamics remain poorly understood, making it difficult to directly deduce oxygen content from hypoxia PET images. In simulations, it may be possible to analyze the impact of a specific parameter on the final image quality by selectively varying tracer- and tissue-specific parameters, which can be a useful tool to help with interpreting the results of clinical and preclinical imaging studies. Therefore, simulations can be used as one possible tool to study the effects of acute hypoxia, perfusion, and tracer clearance, as well as their consequences on important image features.

Any simulation tool used to study hypoxia PET imaging requires two steps: a simulation of oxygen distribution in tissue, which then serves as input for simulation of oxygen-dependent tracer retention. Usually, the approaches for simulating oxygen and tracer distribution are very similar as they are both based on a reaction–diffusion model. Several approaches have been proposed to simulate oxygen and/or tracer distribution in cancerous tissue. These were performed on ves-

sel maps that are either based on tumor sections [39, 40, 70] or artificial vessel maps [38, 43, 110] and results as well as comparisons have been published for several tracers: FMISO [39,42,44,148], FAZA [148], HX4 [148], and CuATSM [43,44]. While some of these models reproduce observations made in preclinical or clinical experiments, such as matching shapes of tracer time activity curves [39] or similar oxygen distribution histograms [44], a thorough experimental validation by directly comparing the simulation results to hypoxia stainings has not been performed yet.

To make simulation results a more reliable tool for interpreting experimental results, a thorough experimental validation is necessary to confirm that the simulation is capable of reproducing results seen in vivo. The goal of this study is to take an important step toward validation of a simulation model for nitroimidazole-based tracers against experimental data based on immunoflourescence images of microsections from a variety of HNSCC tumor models. Particularly the influence of the various parameters on the robustness of the simulation and the correlation with the experimental data were investigated in this study. Furthermore, inter cell line differences in hypoxia PET tracer retention were investigated.

4.2 Material and Methods

4.2.1 Tumor microsections

A total of n = 73 tumors from nine different HNSCC tumor models were used, as listed in Table 4.1. The experimental procedures to obtain the tumor microsections have previously been described in detail [69]. Briefly, tumors were transplanted into the right hind-leg of anaesthesized NMRI nude mice. One hour before tumor excision, animals were injected with the hypoxia marker pimonidazole, followed by the perfusion marker Hoechst 33342 1 min before tumor excision. After excision, tumors were shock frozen in liquid nitrogen and stored at -80 °C. Five to seven consecutive sections from the tumor centre with an intersection distance of about 200 μm were cut and stained with pimonidazole and CD31 antibodies. Antibody binding was detected by immunofluorescence [69] using FITC-conjugated and TRITC-conjugated polyclonal secondary antibodies, respectively. For this, tumor sections were scanned for Hoechst 33342, FITC, and TRITC fluorescence signals with a Zeiss Axioplan 2 fluorescence microscope equipped with a monochrome digital camera (AxioCamMRm, Carl Zeiss, Jena, Germany) and a motorized scanning stage (Maerzhaeuser,Wetzlar, Germany), using the objective with a ten-fold magnification. For the scanning process and subsequent image analysis, the KS300 image analysis software, version 3 (Kontron Elektronik, Eching, Germany), was used.

After immunofluorescence scanning, the sections were stained with haematoxylin and eosin (HE). Based on these stainings, viable tumor area was manually delineated excluding mouse epidermis and surrounding stroma, cutting and processing artifacts as well as nonviable tumor regions defined by morphological

criteria from the HE stainings.

Table 4.1: HNSCC cell lines analyzed in this study together with the number of tumors and available slices per cell line.

Cell line	Number of tumors	Number of tumor sections in total
CAL-33	8	34
FaDu	10	47
SAS	6	24
UT-SCC-14	10	55
UT-SCC-5	5	23
UT-SCC-8	8	26
UT-SCC-15	8	32
UT-SCC-45	9	33
HSC-4	9	35

4.2.2 Generation of vessel maps

Immunofluorescence images of CD31 and Hoechst 33342 staining were automatically thresholded based on their histogram shape to generate preliminary blood vessel and perfusion maps. The resulting binary images were postprocessed with a morphological closing operation to reduce noise. Blood vessels outside perfused or viable tumor areas were excluded from the final vessel map. As the inter-section distance of 200 μm was too large to generate 3D vessel maps, all simulations were carried out in 2D.

4.2.3 Simulation of oxygen consumption, diffusion and PET tracer binding

Simulations were performed using a previously described model [39, 148] which will be briefly introduced here. Further details are outlined in the Appendix.

Vessel maps generated in the previously described step were used as input for simulation of steady-state oxygen distributions. This was modeled by a reaction–diffusion equation, where oxygen consumption was described as a Michaelis–Menten relationship,

$$\frac{\partial P}{\partial t} = D_{O_2} \nabla^2 P - \frac{M_0 \cdot P}{P + P_0} \tag{4.1}$$

where P is the local oxygen partial pressure, P_0 is the Michaelis–Menten coefficient of oxygen consumption, D_{O_2} is the diffusion coefficient of oxygen in tumor tissue, and M_0 is the maximum oxygen consumption rate.

Briefly, the resulting oxygenation map was used to calculate local cell viability and tracer affinity for each pixel. This information is included in function $K(P)$, the oxygen dependent tracer binding rate. All in all, the simulation of tracer

distribution followed similar reaction–diffusion dynamics,

$$\frac{\partial C_f}{\partial t} = D_T \nabla^2 C_f - K(P) \cdot C_f \tag{4.2}$$

with

$$K(P) = \frac{K_{max} P_1}{P + P_1} \cdot (\frac{P}{P + P_2})^k \tag{4.3}$$

Here, C_f denotes the concentration of free, i.e., unbound tracer, and D_T the diffusion coefficient of FMISO.

$K(P)$ defines the net tracer binding rate, which is a product of tracer binding, increasing with lower oxygen partial pressure, and cell vitality, as tracer binding takes place only in vital cells. Kmax is the maximum binding rate under anoxia, P_1 represents the oxygen partial pressure at which tracer binding is half-maximal, and P_2 gives the partial pressure at which 50% of cells are necrotic.

Simulations cover a time period of 4 h p.i. with a spatial resolution of 10 μm and a temporal resolution of 1 s. C_f changes over time as the supply of free tracer in the blood varies during this 4 h duration. Blood activity was defined by an average blood input function as determined from ten clinical FMISO PET data sets.26

All simulation steps were implemented in MATLAB R2009b. Further simulation details and parameters are outlined in the Appendix (Table 4.3).

4.2.4 Optimization of simulation parameters

Simulations were performed with different values of the parameters M_0, P_0, and P_1. The range of the respective parameters was chosen according to experimental values found in previously published experimental studies (Table 4.2). Additionally, the blood oxygen content was varied over a range between 30 and 50 mmHg. Image resolution was decreased to a pixel size of 40×40 μm^2 for both the simulation and the pimonidazole image and the correlation between the two was determined. For this, simulation results were compared to pimonidazole staining by means of the coefficient of determination R^2, the square of the Pearson correlation coefficient, for assessing pixel-wise correlation. The objective was to find the M_0 leading to the highest R^2 for each section.

During a preliminary analysis, the sensitivity of the simulation to variations in each parameter was assessed by repeating simulations over the entire range of values given in the literature and determining correlation between experimental data for four randomly chosen sections. The parameter with the highest impact on correlation was chosen for subsequent optimization using a slightly extended parameter range for all tumor sections in order to achieve optimal correlation for each section.

The mean values of the optimized parameters over all sections for each cell line were compared using a Wilcoxon rank-sum test in MATLAB R2009b. P-values equal to or lower than 0.05 were considered significant.

Table 4.2: Overview of three model parameters M_0 (max. oxygen consumption rate), P_0 (Michaelis–Menten constant), and P_1 (pO_2 for half max. tracer affinity) with the previous default settings [39] and experimental values found in the literature.

Parameter	Previous default settings	Reference	Experimental values	References
M_0 (mmHg/s)	15(*in vitro*)	[123]	2.7-11.1 (*in vivo*)	[124]
			8.6-33.5 (*in vitro*)	[123]
P_0 (mmHg)	2.0 (*in silico*)	[118]	0.5-2.5 (*in silico*)	[108, 118]
			4.8 (*in vitro*)	[126]
P_1 (mmHg)	1.5 (*in vitro*)	[127]	0.8 - 1.5 (*in vitro*)	[127]

4.3 Results

Figure 4.1 shows the impact of the four investigated parameters maximum oxygen consumption M_0, Michaelis–Menten constant P_0, pO_2 at 50% of maximum tracer affinity P_1, and blood oxygen content on correlation with experimental data for four randomly selected sections of different tumor models. For each graph, one parameter was changed while the others were kept at their default settings (cf., Table 4.2). All parameter changes have an impact on observed correlations, the largest effect being observed for M_0. Changes in blood oxygen content did not compensate for changes in M_0 (cf., Fig. 1). Thus, M_0 was subsequently optimized in the following simulations for all available tissue sections.

Figure 4.2 shows the changes of R^2 for different time points post injection. Tumor-to-background ratio increases with simulation time, as does R^2 between simulation and staining. R^2 shows a steep increase at early simulation time points between 0.5 and 3 h postinjection. At 4 h p.i., which is the typical time point of clinical static FMISO imaging, a close-to-optimal value for R^2 is achieved.

Representative examples for experimental pimonidazole staining and simulated FMISO binding are given in Fig. 4.3, including a large variation of resulting correlation coefficients, ranging from $R^2 = 0.2$–0.8. The examples show that despite low R^2, a good visual agreement between experimental staining and simulation may be observed. This observation is due to the high gradients observed in some experimentally stained tumors which could not entirely be reproduced by the simulation and hence led to a low correlation coefficient.

A summary of the optimization results is given in Fig. 4.4, which shows box plots for maximum oxygen consumption M_0 and the corresponding R^2 for each cell line. Simulated median M_0 ranged from 2.2 to 4.5 mm Hg/s, which is at the lower end of the literature range (2.7–11.7 mm Hg/s). Observed median correlations ranged from 0.20 to 0.54. Differences in median between tumor models tested significant both for M_0 and R^2 for most models (cf., Tables 4.4 and 4.5). The mean variance of M_0 for sections taken from the same tumor implant was 30.3% (range 15.6%–47.5%) lower than the variance of all sections of the same tumor

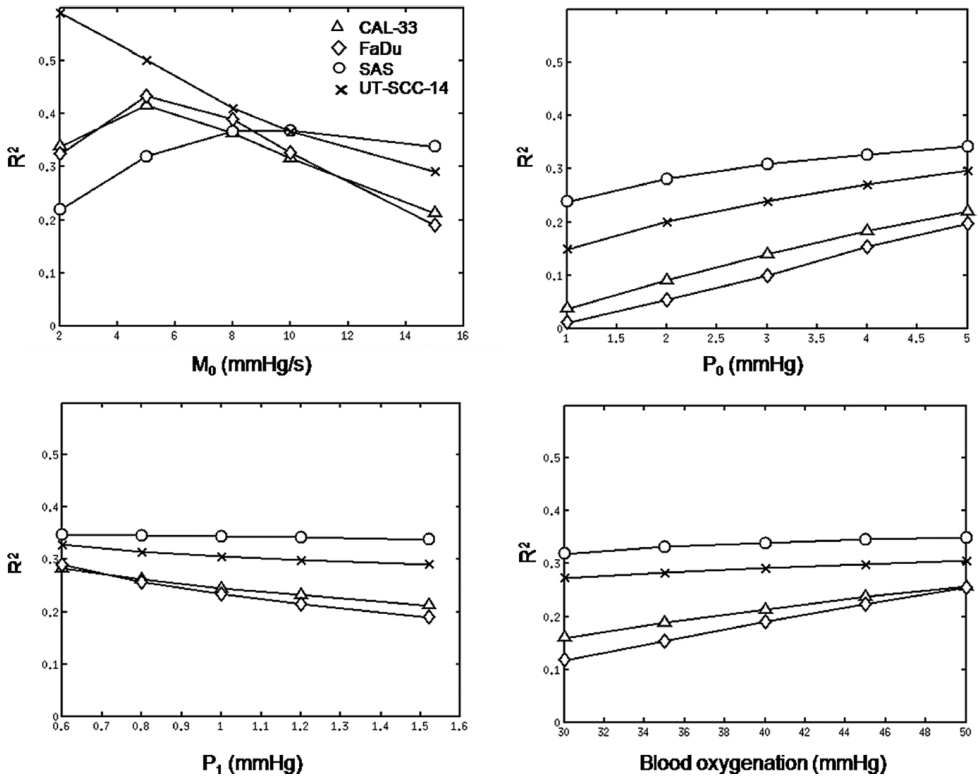

Figure 4.1: Impact of maximum oxygen consumption M_0, Michaelis–Menten constant P0, the pO_2 for half-maximum tracer affinity (P_1), and blood oxygenation on correlation (R^2) between simulation and experimental pimonidazole staining. Results are shown for four randomly selected slices of four different cell lines.

model.

4.4 Discussion

In this study, we have assessed a method for simulating the spatial accumulation and retention of FMISO in tumor tissue. Our findings reveal that hypoxia tracer distributions several hours p.i. can be simulated on a microscopic scale with reasonable accuracy, as our comparison of simulation results and experimental pimonidazole stainings revealed significant correlations. Even in cases of low correlation coefficients, a good visual agreement between simulation and experimental staining for hypoxia was observed.

However, the method is subject to a number of limitations. In this study, all simulations were carried out in 2D. Therefore, only radial diffusion was accounted for in the model, neglecting diffusion in out-of-plane direction. Nevertheless, the

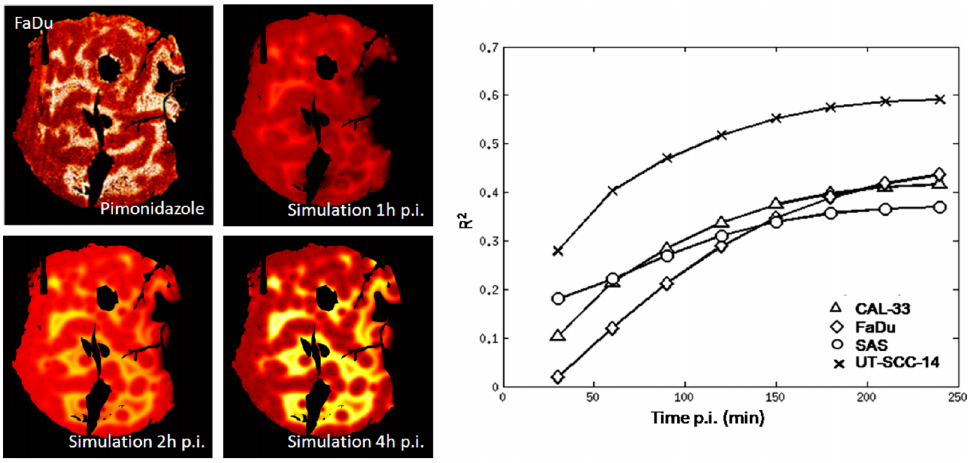

Figure 4.2: Simulation results and changes of correlation (R^2) between pimonidazole stainings and optimized simulation over the simulated time course of 4 h p.i.

model can easily be expanded to 3D simulation. Realistic 3D reconstructions of tumor vasculature with a high spatial resolution of 20–30 μm are an essential prerequisite to perform the respective simulations in 3D. However, previous publications have shown that simulations in 2D are a valid approximation, with results comparable to a full 3D simulation [110].

Additionally, the input functions used for the simulations reflect clinical FMISO imaging, as they were derived from patient blood activities. The experimental data were collected in mice using pimonidazole, which show different clearance and diffusion properties that might affect comparability [148, 149]. Particularly, pimonidazole shows a faster clearance than clinically used nitroimidazole tracers such as FMISO or FAZA, which was one of the reasons why a simulation time of 4 h was chosen for final comparison. However, the finding that R^2 reaches a stable optimum after approximately 4 h p.i. further corroborated this decision.

The simulations were carried out assuming that the maximum oxygen consumption M_0 is homogeneous over the entire tissue section. The fact that considerable differences in optimized M_0 were observed between different sections of the same tumor indicates that this might not be the case, suggesting that the optimized M_0 value is probably an average value of M_0 over one tumor slice. Also, variations in blood oxygen partial pressure were neglected aside from excluding unperfused vessels. Furthermore, optimization of oxygen partial pressure for each individual blood vessel was not feasible as the introduction of too many degrees of freedom would render the parameter optimization unstable.

While good visual agreement and correlations were obtained for staining patterns, validating the overall simulation approach, verification in terms of simulating absolute PET activities could not be realized as the experimental data

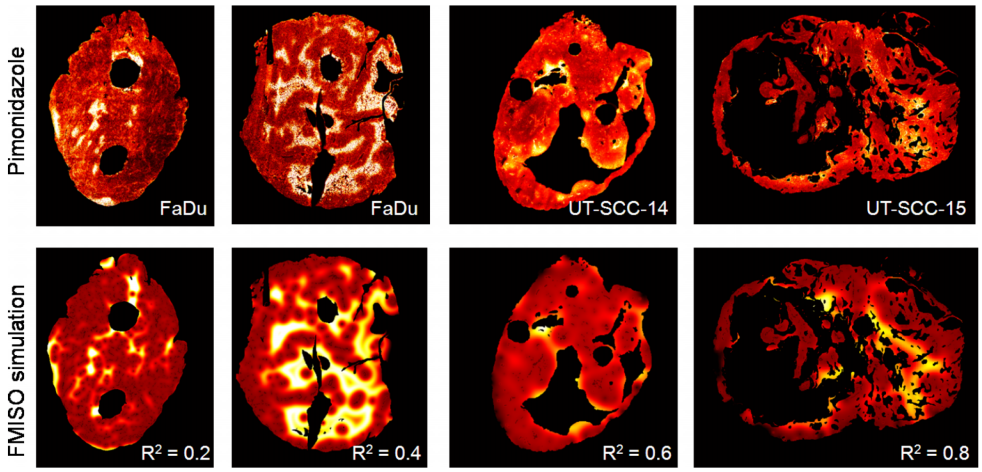

Figure 4.3: Representative pimonidazole stainings showing various levels of pixel-based correlation (coefficient of determination, R^2) with their corresponding simulations.

lack the necessary information. A small-animal PET acquisition prior to tumor excision could be a potential approach to quantify tracer activity experimentally.

Preliminary data revealed that the selection of the maximum oxygen consumption rate M_0 is critical for the accuracy of the simulation. The improved correlation between simulation and experimental data was indeed a result of M_0 optimization, as similar correlations could not be achieved by increasing the blood oxygenation or altering tracer binding parameters. The same was true for the Michaelis–Menten constant P_0, which was shown to be a robust parameter after optimization of M_0 over a large part of its literature range. After optimization, the simulation results were robust to changes in the other parameters, usually affecting R^2 by less than 5% over the literature range once the simulation was optimized for M_0, rendering optimization of other parameters unnecessary.

The observed correlation varied greatly between tumor sections for several reasons. For one, largely normoxic tumors with a few severely hypoxic spots tended to give poorer correlations due to the steep gradients at the edges of these spots, an example of which is shown in Fig. 4.3. In these cases, good visual agreement was still observed. In other cases of low R^2, little to no visual correlation could be observed. This was usually caused by faulty vessel maps, which seemed to be caused by the animal being sacrificed before the perfusion marker had reached all areas of the tumor. This resulted in too many blood vessels being excluded from the final vessel map. A resimulation including vessels generally resulted in a higher R^2. Nonetheless, these tumor sections were excluded from the final analysis.

Optimum M_0 values as well as the coefficient of determination R^2 were cell-line dependent, with differences in median testing significant for a majority of

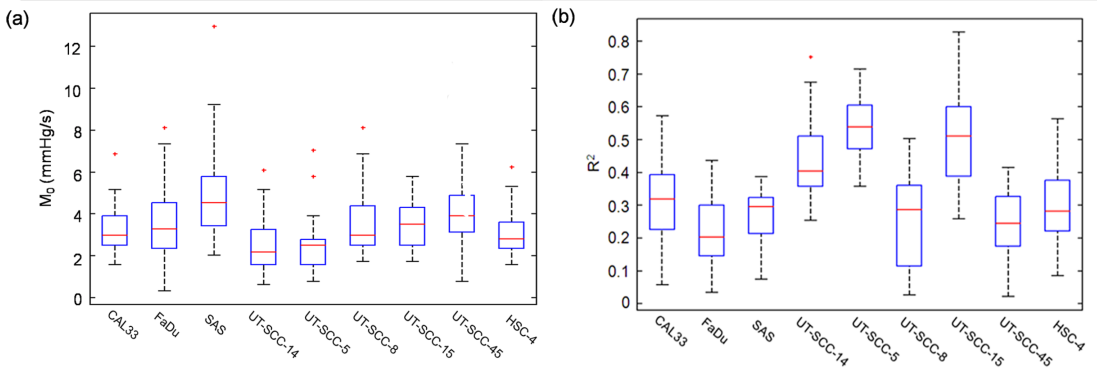

Figure 4.4: Observed distributions of (a) optimized M_0 and (b) resulting coefficient of determination (R^2) for all tumor sections of each cell line after optimization for M_0. The red stars indicate outliers

the cell lines. The optimized M_0 values covered the entire literature range for in vivo data, however, the majority of results were at the lower end of the literature range. This might be due to the different cell lines used in this study, as well as the fact that literature only provided three in vivo values for maximum oxygen consumption, [123, 124] so the actual range might be even larger. Also, the 2D simulation method might lead to an underestimation of tissue oxygenation as blood vessels outside of the 2D plane are not considered. Sections from the same tumor showed a smaller variance in M_0 compared to the sections of all tumors of the same cell line pooled together, a possible indication that intertumor variance is greater than intratumor variance.

4.5 Conclusion

In this study a model for the simulation of FMISO distributions in tumor tissue was shown to provide similar hypoxia PET tracer binding patterns as experimental pimonidazole stainings observed in vivo. Furthermore it could be shown that a tumor model dependent optimized value for maximum oxygen consumption M_0 of the tumor is necessary in order to achieve good agreement between simulation and experimental findings.

Declaration of interest: None of the authors have any conflict of interest related to this work.

4.6 Appendices

Appendix A: Simulation model

Simulations were carried out following the method described in Ref. [39], with a few minor changes. The diffusion term of the reaction diffusion Eq. 4.1 was modeled using a Gaussian fundamental solution,

$$G_{O_2}(x, y, t) = k_{O_2} \cdot t^{-1} \cdot \mathrm{e}^{\frac{x^2+y^2}{4D_{O_2} \cdot t}} \tag{4.4}$$

with D_{O2} being the diffusion coefficient of oxygen in tissue and k_{O2} a normalization factor meeting the following criterium:

$$\int_0^\infty \int_0^\infty G_{O_2}(x, y, t) dx dy = 1 \tag{4.5}$$

The model was iteratively repeated with time steps of 0.01 s as proposed in Ref. [70]. After each step, oxygen consumption was subtracted and the oxygen content of the blood vessels was reset to 40 mm Hg. The simulation was continued until a steady state was reached, which was defined as a change of less than 0.1% between two iterations.

For the simulation of tracer distribution and uptake, a similar approach was chosen, once again applying a Gaussian fundamental solution to Eq. 4.2,

$$G_T(x, y, t) = k_T \cdot t^{-1} \cdot \mathrm{e}^{\frac{x^2+y^2}{4D_T \cdot t}} \tag{4.6}$$

with time steps of 1 s. A small correction was included to account for the source–sink behavior of the blood vessels. We used smaller time steps (0.1 s) to calculate a tracer diffusion kernel only for the region around a blood vessel with the size of 1 pixel and a tracer concentration of 1 kBq/ml for a time of 1 s. A "source-map" was then created by convolving the vessel map with the kernel above, effectively approximating a Dirichlet boundary condition. After each iteration, the concentration gradient between input function and each pixel was calculated and then multiplied with the previously created source-map, and this value was added to the total activity in each pixel.

Appendix B: Blood activity curves

Blood activity curves from ten clinical PET data sets were used to generate the input function. The change of tracer concentration of six voxels in the heart or a major blood vessel was determined over a time period of 4 h p.i. The results were fitted to the following function:

$$A(t) = A_1 \mathrm{e}^{\frac{-t}{\tau_1}} + A_2 \mathrm{e}^{\frac{-t}{\tau_2}} \tag{4.7}$$

where τ_1 is the tracer distribution in the blood stream immediately after injection, and τ_2 the clearance rate. After the fit, the average was taken over all patients for each parameter to obtain the final parameters for the average input function.

Appendix C: Simulation parameters

Table 4.3: A list of the parameters used for the simulation.

	Meaning	Value	References
D_{O_2}	O_2 diffusion coefficient	$2 \times 10^{-9}\,\mathrm{m}^2/\mathrm{s}$	[123]
M	Molecular weight (FMISO)	189.14	Pubchem database
D_T	FMISO diffusion coefficient ($\times 10^{-11}$ $\mathrm{m}^2$7s)	7.90	[120, 121]
P	FMISO partition coefficient	0.41	[135]
P_1	pO_2 inhibiting binding by 50%	0.8 - 1.5 mmHg	[39]
K_{max}	Maximumg binding rate (anoxia)	$1.7 \times 10^{-4}\mathrm{s}^{-1}$	[39]
P_2	pO_2 inducing 50% necrosis	0.1mmHg	[39]
k	Determines step width at P_2	0.3	[39]

Appendix D: Significance levels for differences in M_0 and R^2

Table 4.4: Overview of the significance levels regarding the differences in median for M_0 between cell lines. Note: *: $p < 0.05$, **: $p < 0.01$, —: n.s.

	CAL33	FaDu	SAS	UT-SCC-5	UT-SCC-8	UT-SCC-14	UT-SCC-15	UT-SCC-45	HSC-4
CAL33		-	**	**	-	**	-	**	-
FaDu	-		**	*	-	**	-	*	-
SAS	**	**		**	**	**	**	-	**
UT-SCC-5	**	*	**		**	-	**	**	*
UT-SCC-8	-	-	**	**		**	-	*	-
UT-SCC-14	**	**	**	-	**		**	**	**
UT-SCC-15	-	-	**	**	-	**		-	-
UT-SCC-45	**	*	-	**	*	**	-		**
HSC-4	-	-	**	*	-	**	-	**	

Table 4.5: An overview of the significance levels regarding the differences in median for R^2 between cell lines. Note: *: $p < 0.05$, **: $p < 0.01$, —: n.s.

	CAL33	FaDu	SAS	UT-SCC-5	UT-SCC-8	UT-SCC-14	UT-SCC-15	UT-SCC-45	HSC-4
CAL33		**	-	**	-	**	**	*	-
FaDu	**		*	**	-	**	**	-	**
SAS	-	*		**	-	**	**	-	-
UT-SCC-5	**	**	**		**	**	-	**	**
UT-SCC-8	-	-	-	**		**	**	-	-
UT-SCC-14	**	**	**	**	**		**	**	**
UT-SCC-15	**	**	**	-	**	**		**	**
UT-SCC-45	*	-	-	**	-	**	**		-
HSC-4	-	**	-	**	-	**	**	-	

5 Part II: Three-dimensional simulation of [^{18}F]FMISO diffusion and retention in a realistic microscopic vessel architecture: A performance evaluation

Linda J. Wack[1], David Mönnich[1], Apolstolos Menegakis[2], Simon Boeke[2], René Winter[1], Katrin Trautmann[3], Aline Leun[1], Gregory Bowden[4], Jonathan Cotton[4], Marcel Krueger[4], Bernd Pichler[4], Daniel Zips[2], Daniela Thorwarth[1]

[1] Section for Biomedical Physics, Department of Radiation Oncology, University Hospital Tübingen, Germany

[2] Department of Radiation Oncology, University Hospital Tübingen, Germany

[3] Department of Pathology and Neuropathology, University Hospital Tübingen, Germany

[4] Department of Preclinical Imaging and Radiopharmacy, Werner Siemens Imaging Center, Tübingen, Germany

submitted to
Physics in Medicine and Biology

Abstract

We developed a three-dimensional (3D) mathematical model of [^{18}F]FMISO tracer diffusion and retention based on realistic 3D microscopic tumour architecture and evaluated the simulation performance with experimental data. Furthermore, this study aims at comparing the performance of this 3D simulation results with widely used two-dimensional approaches. For this, PET/MR imaging using the hypoxia tracer [^{18}F]FMISO was acquired on two FADu xengraft tumours, before they were excised and histologically analyzed. Information on hypoxia, perfusion and vessel distribution was obtained by immunofluorescence labelling. Images were rigidly registered, manually adjusted and thresholded to generate 3D perfused vessel maps. Tissue oxygenation and resulting [^{18}F]FMISO diffusion and retention was mathematically simulated in 3D and 2D. Simulated [^{1}8F]FMISO distribution was subsequently compared pimonidazole staining and simulated time-activity curves to preclinically measured PET data. [^{1}8F]FMISO hypoxic fractions (HF) simulated in 3D were comparable to pimonidazole HF with 0.35 ± 0.11 vs. 0.37 ± 0.07 (p = n.s.) for tumour 1 and 0.28 ± 0.03 vs. 0.30 ± 0.03 (p = n.s.) for tumour 2. Simulations in 2D resulted in comparable HFs for tumour 1 with 0.34 ± 0.05, but significantly different results for tumour 2 (0.24 ± 0.04, $p = 0.001$). Sensitivity and specificity were about 50% and 15% higher in 3D than in 2D simulations, respectively. Visually, similar spatial [^{1}8F]FMISO distribution patterns as in pimonidazole staining were observed in 3D simulations only. Compared to dynamic PET measurements of the same tumour, both simulations showed similar overall activities (mean difference 3D: 8.3%, 2D: 17.9%). Consequently, we conclude that realistic 3D vascular models accounting for out-of-plane diffusion must be used to obtain more reliable tracer accumulation patterns when studying the complex image formation processes during hypoxia imaging.

5.1 Introduction

Tumour hypoxia is known to increase radioresistance of tumour cells, and consequently, negatively affect the prognosis after radiotherapy [21, 22]. Beyond its use as a prognostic factor, assessing and quantifying tumour hypoxia has become a target in the on-going efforts for individualized radiotherapy strategies to help improve treatment outcome. Aside from methods aiming to increase tumour oxygenation [76] or administration of radiosensitizers to counteract hypoxia-induced radioresistance [140, 150] better treatment outcomes might be achieved by selectively escalating delivered dose to hypoxic sub-volumes of the tumour, an approach referred to as "dose painting" [31,151]. With the establishment of high-precision imaging modalities and radiotherapy delivery techniques in the clinical routine, implementation of dose painting during treatment delivery is technically and clinically feasible, and therefore a subject of on-going clinical studies attempting to assess its benefits on treatment outcome [92].

Hypoxia dose painting in particular requires a precise, 3D spatial quantification of hypoxia in order to make the necessary treatment adjustments. Invasive techniques, such as polarographic or optical oxygen sensing probes, are considered the gold-standard for measuring hypoxia, but do not provide 3D resolution [23]. Positron-emission tomography (PET) using radiolabelled nitroimidazoles as a non-invasive alternative has been the subject of intensive research over the past years, both for quantification of hypoxia and for prediction of radiotherapy outcome [18,27,72,73]. Along with the well-established and widely used tracer [^{18}F]-Fluoromisonidazole ([^{18}F]FMISO) [18, 144, 145, 152], other nitroimidazole-based tracers have been developed and used in clinical and preclinical studies, such as [^{18}F]-Fluoroazomycinarabinoside ([^{18}F]FAZA) [72, 153], and [^{18}F]HX4 [100]. These tracers show the similar binding properties as [^{18}F]FMISO, while different pharmacokinetic properties are modified to achieve faster clearance and higher image contrast.

However, the exact quantitative relationship between signal formation in hypoxia PET imaging and microscopic tumour oxygenation is not yet fully understood [154], making it difficult to deduce oxygen content directly from the image signal. A better understanding of the exact dynamics of tracer diffusion and retention may improve interpretation of the image information and thus enhance potential therapeutic benefits. In this concept, mathematical modelling techniques are used to provide additional insights, as they allow quantification of the individual parameters' impact on image signal, such as tracer clearance, diffusion, and perfusion variations leading to acute hypoxia. These simulation studies are a valuable additional tool for the planning of pre-clinical and clinical studies, as well as for the evaluation of imaging protocols.

Several models for simulation of tissue oxygenation or hypoxia PET tracer accumulation have been presented in the past. While the algorithms differ, usually they have a similar approach, which was first presented in 2006 by Kelly and Brady [38]. In a first step, oxygen distribution in tissue is simulated. If a simula-

tion of PET tracer is included, the oxygen distribution is then used to determine local tracer binding rates. As both processes are described by a reaction-diffusion equation, they are usually treated numerically using similar approaches. The exact numerical methods differ between implementations, using finite difference and finite-element methods [39, 40, 108, 155], Green's function or the heat kernel [70].

However, a thorough validation is necessary for any of these simulation models in order to be utilized as a clinical and practical research tool. Unfortunately, evidence of actual validation is sparse. Bowen *et al* showed that simulated oxygen histograms agree well with measurements of tissue oxygenation using Eppendorf probes [44]. The [^{18}F]FMISO simulation model proposed by Mönnich itet al generated time activity curves (TACs) comparable to those found in clinical PET images [39]. Lately, we demonstrated that high correlation between 2D-simulated hypoxia tracer uptake and *in vivo* uptake of the chemically similar substance pimonidazole can be achieved if oxygen consumption parameters are optimized [139]. However, a thorough validation both against immunofluorescence staining or autoradiography on a microscopic level as well as against measured PET activities on the macroscopic level is still missing. Also, the impact of missing out-of-plane diffusion on oxygen distribution in the 2D model is still unclear. While some studies suggest that 2D and 3D models give comparable results on artificial vessel maps [45,110], other studies indicate that this might not be the case for realistic vessel distributions [112]. To our knowledge, no 3D model of tracer diffusion-retention dynamics based on realistic vascular information has been published so far.

The goal of this study is to develop a 3D mathematical model to simulate oxygen distribution, [^{18}F]FMISO diffusion and accumulation on realistic 3D vessel maps and to evaluate its accuracy, both by direct comparison of [^{18}F]FMISO accumulation patterns to pimonidazole immunofluorescence staining as well as by comparing simulated activities to experimentally measured [^{18}F]FMISO PET time activity curves in the same tumour. Additionally, the method's performance will be compared to that of widely used 2D approaches.

5.2 Material and Methods

An overview of the workflow and analysis strategies used in this study including data preparation, pre-processing and subsequent simulation is presented in Figure 5.1. Briefly, fluorescence images of consecutive tumour sections of 10 μm thickness are obtained to gain information on vessel distribution, perfusion and hypoxia. Images are registered, masks are drawn to distinguish vital tumour from mouse stroma and necrosis, and vessel maps are generated based on the vascularization and perfusion immunofluorescent signals. 2D vessel maps of consecutive sections are then combined to form 3D vessel maps based on actual tumour vessel architecture. These can be used as input to simulate oxygen distribution and subsequently, [^{18}F]FMISO diffusion and retention (Figure 5.1).

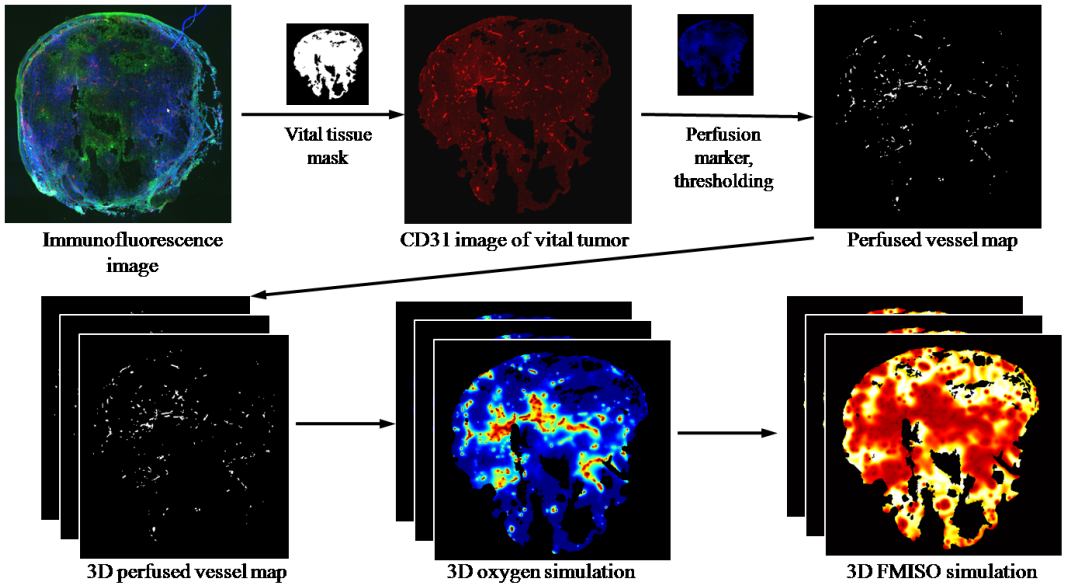

Figure 5.1: Overview of the simulation method. After PET imaging, tumour sections were labelled for endothelial marker CD31, perfusion marker Hoechst 33342 and hypoxia marker pimonidazole. Information obtained from the CD31 and Hoechst 33342 were used to reconstruct 3D models of vascular architecture, on which oxygenation and FMISO accumulation was simulated.

5.2.1 PET/MR imaging, immunofluorescence microscopy

The animal facilities and all experiments were approved according to the institutional guidelines and the German animal welfare regulations. 4-6-week-old immune-deficient female nude mice (NMRI nu/nu, Charles River Laboratories, Wilmington, USA) received a 4 Gy total body irradiation to further suppress the residual immune system 2 to 5 days prior to tumour cell injection into the hind leg. The injected tumour cells belonged to the cell line FaDu, a tumour model for human squamous cell carcinomas of the head and neck (HNSCC) [69]. 4-6 weeks after cell-injection simultaneous PET/MR imaging was performed on a 7T scanner (Bruker, Ettlingen, Germany) with technical specifications similar to the PET-insert described in [156]. The imaging protocol included a 90 min dynamic [^{18}F]FMISO PET acquisition, anatomical T2-weighted and diffusion-weighted (DW) magnetic resonance imaging (MRI) as well as dynamic contrast enhanced (DCE) MRI. Animals were anesthetized with 1.5% isoflurane (Abbott, Wiesbaden, Germany) evaporated in breathing air at a flow of 0.5 L/min, and body temperature was maintained at 37 °C. After imaging, the hypoxia marker pimonidazole (Hypoxyprobe, Burlington, USA; 0.1 mg/g body weight, dissolved at 10 mg/ml in 0.9% NaCl, i.p.) was injected 1h prior to tumour excision as well as the perfusion marker Hoechst 33342 (Sigma Aldrich, Deisenhofen, Germany; 15 mg/kg body weight, dissolved in 0.05 ml PBS, i.v.) 1 min before tumour

excision. Tumours were snap frozen in liquid nitrogen and stored at -80 °C until cutting.

For immunofluorescence labelling, 120 serial sections with a thickness of 10 μm each were cut from the tumour centre. Immunofluorescence labelling following the protocol outlined in Yaromina *et al* [69] was performed. Sections were air-dried at room temperature for 30 min, fixed in 4 °C acetone for 10 min and rehydrated in phosphate-buffered saline (PBS). Subsequently they were incubated over night with both antibodies at 4 °C, namely a rabbit polyclonal antibody against pimonidazole (1:2500, Hypoxyprobe, Burlington, USA) and a monoclonal rat anti-mouse CD31 antibody (1:500, BD Biosciences, Franklin Lakes, USA). Washing in PBS was followed by incubation with combined application of TRITC-conjugated anti-rat IgG and FITC-conjugated anti-rabbit IgG polyclonal antibodies (Dianova, Hamburg, Germany) for 1 h at room temperature. After this, slides were washed in PBS and mounted in DAKO fluorescent mounting medium (DAKO, Glostrup, Denmark). Tumour sections were then scanned on a Zeiss Axiovert fluorescene microscope (ZEISS, Jena, Germany) using a motorized stage, signal was acquired with amonochrome digital camera (AxioCamMRm, Carl Zeiss, Jena, Germany; motorized scanning stage, Maerzhaeuser, Wetzlar, Germany, 400_ EC Plan Neofluar) using Axiovision 4.9.2 software to detect Hoechst 33342, FITC, and TRITC fluoresence signals, under an objective with a 10x magnification. The available data for each tumour is summarized in Table 5.1.

Table 5.1: Available experimental data for both analyzed tumours

	Tumour 1	Tumour 2
Tumour model	FaDu (HNSCC)	FaDu (HNSCC)
Tumour diameter (mm)	15	3
No. of sections (10 μm)	120	120
CD31 staining	yes	yes
Pimonidazole staining	yes	yes
Hoechst	yes	yes
Percentage of tumour volume included in the 3D vessel map	$\sim$ 1.5%	$\sim$ 30%
Dynamic [^{18}F]FMISO PET	No (error during acquisition)	yes

5.2.2 Generation of tissue masks, registration and reconstruction of vessel maps

After fluorescence scanning, each section was stained with haematoxylin and eosin (HE) to delineate viable tumour tissue and exclude mouse stroma and necrotic areas. Rigid registration of fluorescence images was performed, and manual adjustments were made using Adobe Photoshop (Adobe Systems Incorporated, San Jose, USA) where necessary to reduce the impact of distortions due the cutting process.

Immunofluorescence images of CD31 were automatically segmented by thresholding based on their histogram shape to generate preliminary blood vessel maps. Post-processing with a morphological closing operation was performed to reduce noise. Hoechst 33342 images were segmented using a similar approach, but automatically suggested thresholds were adjusted according to visual appearance if necessary. Post-processing of Hoechst images included also a morphological closing operation followed by a dilation to expand perfusion-positive areas beyond the stained cell nuclei. Blood vessels from the processed CD31 images that were found to be outside of perfused areas were excluded from the final vessel maps. Combination of these 2D vessel maps resulted in 3D vessel maps with a total size of $3 \times 3 \times 1.2$ mm^3 for each tumour.

5.2.3 Simulation

3D simulations of oxygen distribution and [^{18}F]FMISO diffusion and uptake were implemented in MATLAB 2009b (Mathworks, Natick, USA), using the approach outlined by Mönnich *et al* [39]. The simulation is implemented in a two-step process: First, a steady-state oxygen distribution is simulated where diffusive transport of oxygen is in equilibrium with cellular oxygen consumption, with a resolution of 5 μm. Secondly, [^{18}F]FMISO diffusion and retention is modelled based on blood input functions derived from PET scans and binding rates calculated as a function of the previously simulated local oxygen concentrations with a resolution of 10 μm. A detailed description of the simulation method including highlighting of adjustments in the 3D simulations compared to the earlier published 2D approach is given in the supplementary material.

5.2.4 Comparison of simulation results with experimental data

For comparison of microscopic [^{18}F]FMISO simulation to pimonidazole staining, ten sections of each tumour were randomly chosen and pimonidazole-positive tumour areas were manually delineated to distinguish hypoxic from normoxic areas. These binary images were used as gold-standard and compared to thresholded simulation results to determine overlap, sensitivity and specificity as well as mean distance to agreement (DTA) to pimonidazole-positive areas of 2D and 3D simulations. The threshold for the simulated [^{18}F]FMISO images was set to the mean value of maximum and minimum simulated activity, with activity including signal from bound and unbound tracer. DTA was defined as the mean distance of false-positive simulated voxels to the nearest pimonidazole-positive voxel. Pixels/voxels less than 150 μm away from the tumour edge were excluded to avoid effects caused by the lack of vessel information outside the tumour boundaries. Results were tested for significance using a t-test for paired samples.

Average activity over the entire tumour was determined from a dynamic PET scan of the tumour over 90 minutes post-injection (p.i.) taken right before excision and compared to simulations over the same duration. To make simulation results

comparable, the simulated images were processed to account for partial volume effects due to the lower spatial resolution of the PET scanner. In a first step, the activity in the stroma surrounding the tumour was set to that of the blood input function at the given time point. Simulated signal from necrotic areas was not excluded for sake of comparability as there was no way to exclude it from the PET measurement. The images were filtered with a Gaussian filter ($\sigma = 300$ μm, FWHM: 0.72mm) approximating the blur expected to occur in a PET scanner with a resolution of about 1 mm and a voxel size of 0.7x0.7x0.8 mm^3. Then the average activity in the tumour was determined for all 21 simulated time points and compared to the measured PET data.

5.3 Results

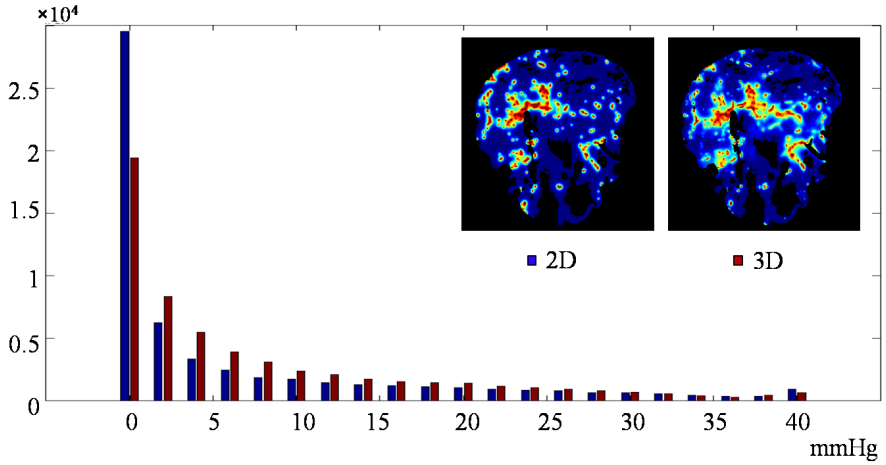

Figure 5.2: Changes in oxygen distributions and the resulting histogram on a representative sample. The small images show the simulated oxygen distributions for the 2D and 3D vessel map, respectively, with oxygen levels ranging from 40 mmHg (red) to 0 mmHg (dark blue).

The comparison of full 3D simulations of steady-state oxygen-distribution to 2D simulations revealed that due to the lack of out-of-plane diffusion, the 2D scenario resulted in steeper oxygen gradients. This led to an overestimation of the extent of severely hypoxic regions, as shown by the oxygen histogram in Figure 5.2. 45.5% and 26.7% of the analyzed tumour volume presented an oxygen partial pressure (pO_2) of less than 1 mmHg for 2D and 3D, respectively.

The consequences resulting from these changes in the pO_2 distribution for the simulated [^{18}F]FMISO distributions are presented in Figure 5.3, showing the experimental pimonidazole staining, the 2D and 3D simulations, in addition to the resulting overlaps for the same section, with a sensitivity of 0.56 and specificity of 0.79 for the section shown. Visually, the 3D simulation shows better agree-

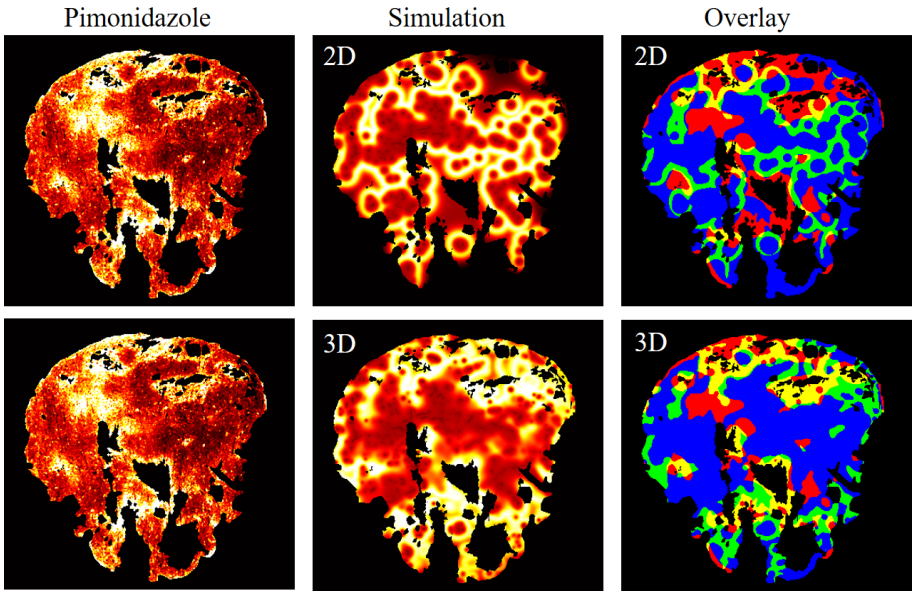

Figure 5.3: Representative comparison of an experimental pimonidazole staining (white: high retention, dark red: low retention), with the simulated [^{18}F]FMISO accumulation (white: high simulated FMISO activity, dark red: low simulated activity) and the resulting overlay: normoxic (blue), pimonidazole-positive (staining, red), [^{18}F]FMISO-positive (simulation, green), and hypoxic in simulation and staining (yellow).

ment between [^{18}F]FMISO and pimonidazole hypoxic fractions compared to the 2D simulation. While the 2D simulation leads to only overlap between simulated and pimonidazole-hypoxic fractions, the 3D model results in accumulation patterns similar to those observed on the pimonidazole staining.

Figure 5.4 shows the median hypoxic fractions measured via pimonidazole staining, in 2D and 3D simulations, respectively, for all analyzed tumour sections. Hypoxic fractions from the pimonidazole stainings agreed well with 3D simulated hypoxic fractions, non-significant differences for both tumours, which were 0.37 ± 0.07 vs. 0.35 ± 0.11 and 0.30 ± 0.03 vs. 0.28 ± 0.03 for tumour 1 and 2, respectively. For the 2D simulation, a significant difference between hypoxic fraction was found for tumour 2 with a simulated hypoxic fraction of 0.24 ± 0.04 ($p = 0.001$, Figure 5.4a), whereas tumour 1 shared comparable hypoxic fractions in the 2D model as well.

The 3D simulation also consistently performed much better in terms of sensitivity and specificity. This was shown for both performance measures and in both tumours (Figure 5.4b,c). Mean sensitivity for both tumours was 0.55 for the 3D and 0.36 for the 2D approach ($p < 0.001$), while the mean specificity was 0.68 and 0.76 for 2D and 3D, respectively ($p < 0.001$).

Also, mean DTA was much lower for the 3D simulation. The mean distance of

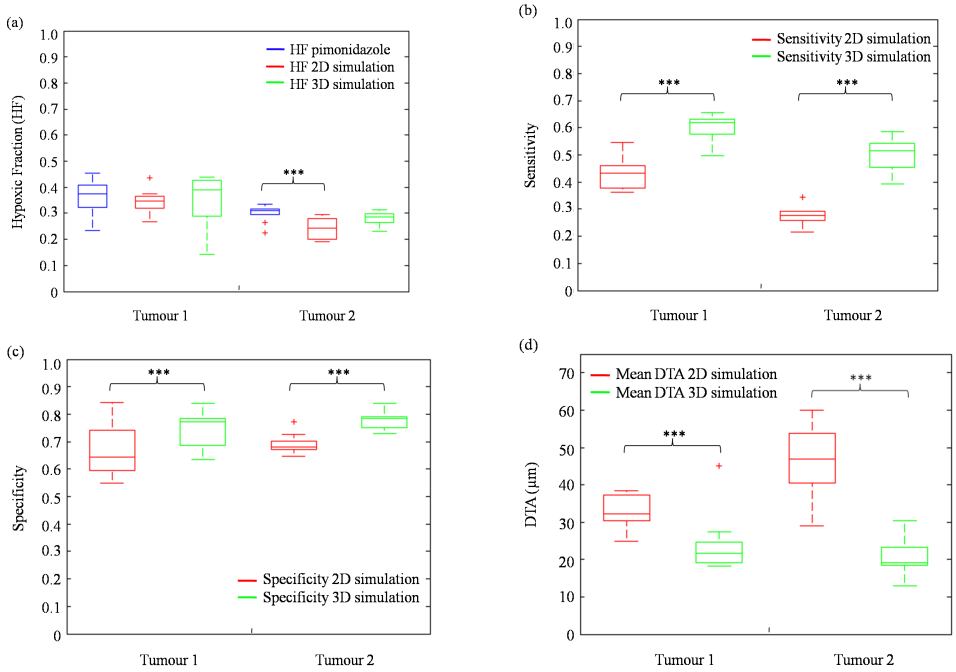

Figure 5.4: Results for hypoxic fraction (a), sensitivity (b), specificity (c) and mean distance to agreement for false-positive voxels (d). Three asterisks indicate a significance level of $p < 0.001$.

a false-positive voxel to hypoxic areas (as defined by pimonidazole) was 22 μm, as compared to 42 μm for the 2D simulation ($p < 0.001$, Figure 5.4d).

When the average simulated time activity curve over all sections in 2D and 3D was compared to the dynamic [^{18}F]FMISO PET in the tumour, both simulations gave activities and slopes close to the measured PET activities. The 3D approach performed better with respect to the measured PET activity, yielding a mean error of $8.2 \pm 13.7\%$, when compared to the 2D simulation with an average deviation of $17.9 \pm 15.4\%$ was observed (Figure 5.5). Results showed a mismatch in the early wash-in phase, where the simulations did not adequately model the perfusion peak observed in the PET scan. However, the accuracy was improved during the retention phase, with average errors of 3.0% and 13.4% between 35 and 90 min p.i., for 3D and 2D simulations, respectively.

5.4 Discussion

The results shown here support the approach that [^{18}F]FMISO retention patterns similar to those observed *in vivo* can be simulated based on reaction-diffusion equations. The simulation results shown here were performed on realistic 3D vascular maps using established literature values. The model presented here is easy to implement and can be run on commonly available desktop PCs with a

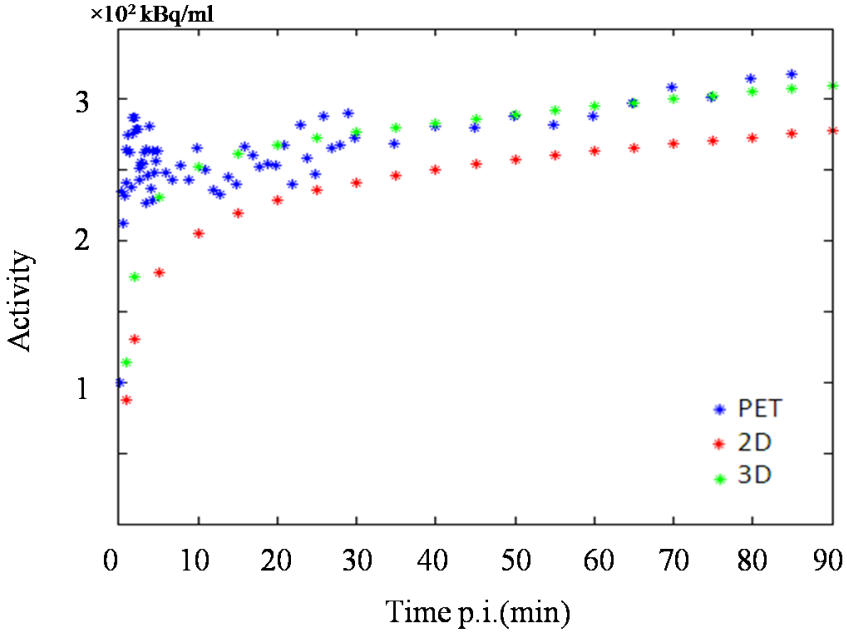

Figure 5.5: Activity concentration in tumour measured in the PET system dynamically over 90 min p.i., compared to simulated activities in the $3 \times 3 \times 1.2$ mm^2 tumour area for the 2D and 3D simulation approach.

computation time of about 2 min for a 2D 3×3 mm^2 section and about 4h for a $3 \times 3 \times 1.2$ mm^3 3D vascular map.

The main cause for the different accumulation patterns in the two simulation approaches lies in the out-of-plane diffusion, whose inclusion results in a more homogeneous distribution of oxygen in the 3D model, while it is not taken into account in the 2D model (cf. Figure 5.6). Changes in oxygen distribution caused by including out-of-plane diffusion into the model affects the tracer binding rate (Equation 5.4). The differences in the resulting tracer binding rates comparing 2D to 3D simulation are shown in Figure 5.6a. The figure visualizes the change in binding rates caused by the extension of the model to three dimensions, normalized to the maximum binding rate. The figure demonstrates that the inclusion of out-of-plane diffusion in the 3D model effectively results in [^{18}F]FMISO accumulation in a larger distance to the blood vessels. These findings agree well with simulations performed by Grimes *et al* [112], who found that when simulating on realistic vessel distributions, 2D approximations are generally inadequate representations of 3D oxygen distribution, as they tend to overestimate hypoxia and anoxia. In the past, studies have suggested that 2D simulations of oxygenation and [^{18}F]FMISO accumulation might give realistic results, but these studies had been performed on artificial vessel maps with perpendicular vessels, and only histogram shape was compared [45, 110].

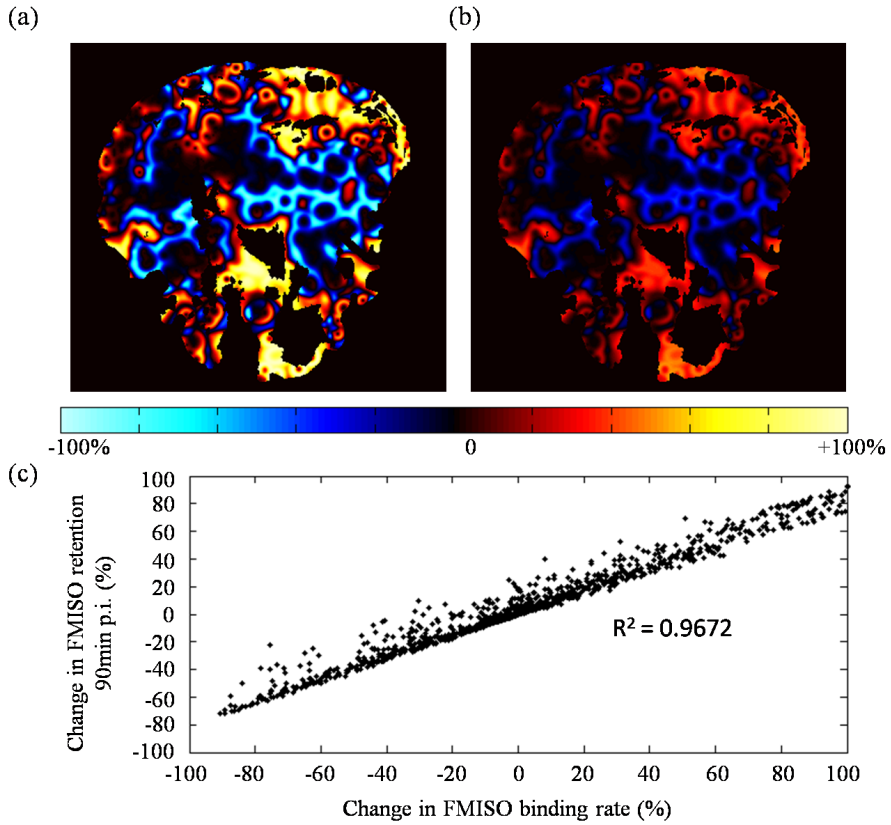

Figure 5.6: Changes in [^{18}F]FMISO binding rate (a), and observed [^{18}F]FMISO tracer retention (b) after extension of the model to 3D, in percent of the maximum binding rate and maximum tracer retention, respectively. A linear correlation between the changes in binding rate and [^{18}F]FMISO retention is observed (c).

The observed differences in terms of spatial oxygen distribution results in lower binding rates in the 3D model in close proximity to perfused areas, and higher binding rates with increasing distance from the blood vessels, as the percentage of vital hypoxic cells is still high enough for tracer binding to occur (Figure 5.6a). The quantitative changes in tracer binding rate closely mirror the differences seen in the simulated tracer uptake for 2D and 3D (Figure 5.6b, changes are plotted as percent of maximum uptake). Consequently, a high linear correlation between differences in binding rate and changes in tracer uptake is observed (R = 0.983, Figure 5.6c). This indicates that the differences in simulated oxygen distribution are the main cause for the observed differences in tracer distribution. A diffusion limitation of [^{18}F]FMISO binding over the 90 min simulation time is another, though minor, contributing cause in regions far away from the blood vessels.

However, the quality of 3D models is highly dependent on the quality of the

vessel maps. Inadequate spatial registration of consecutive sections may result in non-overlapping vessels in z-direction. As a consequence, the contribution of out-of-plane diffusion is strongly overestimated, which leads to an underestimation of hypoxia and [^{18}F]FMISO accumulation.

Aside from its higher sensitivity and specificity, the DTA is another measure that indicates that the 3D simulation is better capable of reproducing *in vivo* pimonidazole patterns than the 2D model. In the 3D model, many false-positive voxels are located closely to pimonidazole-positive regions, with an average distance of 22 μm. About 25% of false-positive voxels are located directly adjacent to pimonidazole positive areas. Similar results were observed for the distance of false-negative voxels to [^{18}F]FMISO-positive simulated voxels (data not shown).

In a previous publication, we had observed good correlations between 2D simulations and pimonidazole staining [139] . However, these simulations had been optimized by adjusting the maximum oxygen consumption, with optimum values ranging below the standard value of 15 mmHg/s, therefore compensating for the overestimation of anoxia observed in 2D under standard conditions. As we have shown here, these low values are the result of an inherent systematic shift of 2D simulations. The value of 15 mmHg/s used here is in perfect agreement with commonly used literature values [38, 40, 108].

5.5 Conclusion

We demonstrate that simulating [^{18}F]FMISO diffusion and retention on three-dimensional realistic vessel maps using established parameter values is feasible and yields results comparable to those observed *in vivo*. Comparison with 2D simulation approaches revealed that two-dimensional models are not adequate due to their missing out-of-plane diffusion, performing worse with respect to sensitivity and specificity. Both the [^{18}F]FMISO time-activity curves simulated with the 2D and 3D approach agreed well with the experimental PET measurement performed in the same tumour, with the 3D method yielding slightly superior results.

5.6 Acknowledgments

The research leading to these results has received funding from the European Research Council under the European Union's Seventh Framework Program (FP/2007-2013)/ERC Grant Agreement n. 335367.

We thank the Department of Neuropathology, University Hospital Tübingen, for allowing us access to the cryotome, and the Department of Experimental Ophthalmology, University Hospital Tübingen, for allowing us access to their Zeiss Axiovert fluorescence microscope. We thank the Department of Urology, University Hospital Tübingen, for help with the HE staining.

5.7 Appendices

Simulation of steady-state oxygen distributions

Oxygen in tissue was modelled by a reaction-diffusion equation of oxygen diffusion along the concentration gradient and cellular oxygen consumption, the latter being described by a Michaelis-Menten relationship:

$$\frac{\partial P}{\partial t} = D_{O_2}\nabla^2 P - \frac{M_0 \cdot P}{P + P_0} \tag{5.1}$$

With P as the local oxygen partial pressure, P_0 as the Michaelis-Menten coefficient of oxygen consumption, D_{O_2} as the oxygen diffusion coefficient in tissue, and M_0 being the maximum oxygen consumption rate. While Mönnich *et al* used a finite elements approach to solve this partial differential equation [39], we used the Gaussian fundamental solution outlined in Lagerlöf *et al* [70], as this approach is computationally more efficient and easy to implement both in 2D and 3D:

$$G_{O_2}(x, y, z, t) = k_{O_2} \cdot t^{\frac{-n}{2}} \cdot \mathrm{e}^{\frac{x^2+y^2+z^2}{4D_{O_2}\cdot t}} \tag{5.2}$$

Here, D_{O_2} is the same diffusion coefficient as above, n is the number of simulated dimensions and k_{O_2} is a normalization factor meeting the following condition:

$$\int_0^\infty \int_0^\infty \int_0^\infty G_{O_2}(x, y, t)dxdydz = 1 \tag{5.3}$$

The assumption of the Gaussian fundamental solution is that the initial distribution at $t = 0$ can approximatively be described as a δ-function. As each voxel on the vessel map is regarded as a separate source of a size of $5 \times 5 \times 10$ μm^3 , which is much small compared to the distance of hypoxic regions from the vessels. The diffusion at any point in time can be determined by convolving the initial oxygen distribution with the diffusion kernel from Equation 5.6. For simulations in 2D, dimension z is set to zero.

Appendix B: Simulation of hypoxia tracer diffusion and uptake

The diffusion and retention of [^{18}F]FMISO was simulated by numerically solving a reaction-diffusion equation similar to the one in the previous step [39].

$$\frac{\partial C_f}{\partial t} = D_T\nabla^2 C_f - K(P) \cdot C_f \tag{5.4}$$

with

$$K(P) = \frac{K_{max}P_1}{P + P_1} \cdot (\frac{P}{P + P_2})^k \tag{5.5}$$

Here, Cf is the concentration of freely diffusing, unbound tracer. $K(P)$ is the net tracer binding rate as calculated from the previously simulated steady-state oxygen distribution and cell viability. Here, K_{max} is the maximum binding rate

under anoxia, P_1 gives the oxygen partial pressure at which tracer binding is half-maximal, and P_2 represents the partial pressure at which 50% of cells are necrotic. The parameter k determines the step width of the cell vitality function at P_2. As nitroimidazoles are transported in the tissue predominantly by diffusion, the fundamental solution was also applied here, adjusted for the tracer diffusion coefficient D_T, with time steps of 1 s:

$$G_T(x, y, z, t) = k_T \cdot t^{-\frac{-n}{2}} \cdot \mathrm{e}^{\frac{x^2+y^2+z^2}{4D_T \cdot t}} \tag{5.6}$$

The method has been used in previous publications [139, 148] and gives results comparable to the computationally less efficient finite-element method previously used by Mönnich *et al* [39]. Computation times for each simulation step are about two minutes for 2D and three hours for the entire 3D $3 \times 3 \times 1.2$ mm^3 vessel maps on an ordinary desktop PC (Fujitsu Esprimo P910, Intel Core i7-3770, 16 GB RAM).

Appendix C: Blood activity curves

Blood input functions determined from the [^{18}F]FMISO PET scans were used as input for the second simulation step. As the heart was outside of the field of view in both PET scans, the activity in well-perfused tissue was used, as it is expected to closely follow the blood activity. Specifically, the activity was determined at 65 different time points between 0 and 90 min post-injection (p.i.) by taking the average activity over a ROI in muscle tissue. The following function was fitted to the determined data:

$$A(t) = A_1 \mathrm{e}^{\frac{-t}{\tau_1}} + A_2 \mathrm{e}^{\frac{-t}{\tau_2}} \tag{5.7}$$

with four open parameters A_1, A_2, τ_1, and τ_1. For tumour 2, an error occurred during the [^{18}F]FMISO PET acquisition, resulting in injection of another [^{18}F]FMISO bolus 40 min pi.i., resulting in unfittable data. Its activities were therefore excluded from the analysis. Instead, a population-based blood input function using the same fitting function was determined from the activities in the left ventricle from a previous series of experiments. However, a comparison between PET measurement and simulated activities was not possible.

Appendix D: Parameters

Parameters used for oxygen and [^{18}F]FMISO simulations are established parameters used in previous publications. They are listed in Table 5.2 and 5.3.

Table 5.2: Simulation parameters used for calculation of the steady state oxygen distribution. Bold font indicates the value chosen for this simulation out of a range of value

Symbol	Meaning	Value	Reference
P_{ie}	Intraerythrocyte pO_2 in tumours	40 mmHg	[39, 108]
D_{O_2}	O_2 diffusion coefficient	2×10^{-9} m^2/s	[123]
M_0	Maximum O_2 consumption rate	15 mmHg/s	[39, 108]
P_0	Michaelis-Menten coefficient of oxygen consumption	**2.0** - 2.5 mmHg	[39, 108]
t	Time used to calculate Gaussian kernel	0.01 s	[70]

Table 5.3: Simulation parameters used for hypoxia PET tracer uptake and diffusion simulation. Bold font indicates the value chosen this simulation out of a range of values

Symbol	Meaning	Value	Reference
M	Molecular weight (FMISO)	189.14	Pubchem
D_T	FMISO diffusion coefficient ($\times 10^{-11}$ m^2/s)	$7.90 \times 10^{1}{}^{1}$ m^2/s	[148] from [121] and [120]
P_1	pO_2 inhibiting binding by 50%	0.8 - **1.5** mmHg	[39]
K_{max}	Maximumg binding rate (anoxia)	4.4×10^{-4}s^{-1}	[45]
P_2	pO_2 inducing 50% necrosis	0.1mmHg	[39]
k	Determines step width at P_2	0.3	[39]
t	Time step used to calculate Gaussian kernel	0.01 s	[70]

6 Part III: Comparison of [18F]-FMISO, [18F]-FAZA and [18F]-HX4 for PET imaging of hypoxia – a simulation study

Linda J. Wack[1], David Mönnich[1], Wouter van Elmpt[2], Catharina M. L. Zegers[2], Esther G. C. Troost[2,3], Daniel Zips[4], Daniela Thorwarth[1]

[1] Section for Biomedical Physics, Department of Radiation Oncology, University Hospital Tübingen, Germany
[2] Department of Radiation Oncology MAASTRO, GROW - School for Oncology and Developmental Biology, Maastricht, The Netherlands
[3] Institute of Radiooncology, Helmholtz-Zentrum Dresden-Rossendorf, Dresden, Germany
[4] Department of Radiation Oncology, University Hospital Tübingen, Germany

published in
Acta Oncologica 2015, 54: 1370-1377 [148]

Abstract

Objective. To investigate the effect of hypoxia tracer properties on positron emission tomography (PET) image quality for three tracers [18F]-fluoromisonidazole (FMISO), [18F]-fluoroazomycinarabinoside (FAZA) and [18F]-flortanidazole (HX4), using mathematical simulations based on microscopic tumor tissue sections.
Material and methods. Oxygen distribution and tracer binding was mathematically simulated on immunohistochemically stained cross-sections of tumor xenografts. Tracer diffusion properties were determined based on available literature. Blood activity and clearance over a four-hour period post-injection (p.i.) were derived from clinical dynamic PET scans of patients suffering from head and neck or bronchial cancer. Simulations were performed both for average patient blood activities and for individual patients, and image contrast between normoxic and hypoxic tissue areas was determined over this four-hour period p.i.
Results. On average, HX4 showed a six-fold higher clearance than FMISO and an almost three-fold higher clearance than FAZA based on the clinical PET data. The absolute variation in clearance was significantly higher for HX4 than for FMISO (standard deviations of 5.75×10^{-5} s^{-1} vs. 1.55×10^{-5} s^{-1}). The absolute tracer activity in these scans at four hours p.i. was highest for FMISO and lowest for HX4. Simulated contrast at four hours p.i. was highest for HX4 (2.39), while FMISO and FAZA were comparable (1.67 and 1.75, respectively). Variations in contrast of 7–11% were observed for each tracer depending on the vascularization patterns of the chosen tissue. Higher variations in clearance for HX4 resulted in an increased inter-patient variance in simulated contrast at four hours p.i.
Conclusions. In line with recent experimental and clinical data, the results suggest that HX4 is a promising new tracer that provides high image contrast four hours p.i., though inter-patient variance can be very high. Nevertheless, the widely used tracer FMISO provides a robust and reproducible signal four hours p.i., but with a lower contrast. The simulations revealed tracer clearance to be the key factor in determining image contrast.

6.1 Introduction

Tumor cell hypoxia causes radiation resistance compared to normoxic cells resulting in a negative impact on outcome of anticancer treatments, including radiotherapy [22]. Assessment of presence, quantity and localization of hypoxia prior to and during treatment has been a subject of ongoing research [143]. These studies do not only investigate its value as a prognostic factor, but also as a predictive factor for allowing for patient stratification and treatment adjustments that could potentially overcome hypoxia-induced radioresistance. These modifications include treatment approaches, such as increasing the oxygen supply to tumor cells, e.g. through hyperbaric oxygen or carbogen breathing, or administering hypoxic cell radiosensitizers, such as nimorazole [23]. Another frequently suggested option is escalating delivered radiation dose specifically to hypoxic subvolumes inside the tumor, a process referred to as dose painting. The establishment of intensity-modulated radiotherapy and other high-precision radiotherapy techniques in routine clinical practice has made such an approach technically feasible [143].

However, there is no clinically validated gold standard to non-invasively identify tumor hypoxia at present [23]. Frequently, dedicated tracers for positron emission tomography (PET) that accumulate specifically in hypoxic tissue volumes are used for non-invasive hypoxia imaging. In contrast to most invasive methods, hypoxia PET imaging provides a spatially resolved quantitative image of tissue oxygenation [138].

Many of the hypoxia-related PET tracers are [18F]-labeled nitroimidazole compounds, including [18F]-fluoromisonidazole (FMISO), which has been used in many clinical and pre-clinical studies [18,144]. Due to the low signal-to-background ratios of FMISO PET, alternative hypoxia tracers have been proposed. One of them, [18F]-fluoroazomycinarabinoside (FAZA), is a focus of current research due to its higher clearance and has found its way into clinical trials [72, 146]. The tracer [18F]-flortanidazole, commonly referred to as HX4, is also a nitroimidazole compound. Similar to FAZA, it is more water-soluble than FMISO [136], and a first study in 12 head and neck squamous cell carcinoma (HNSCC) patients has shown better tumor-to-muscle ratio in HNSCC tumors compared to FMISO [35].

Attempts to quantify and compare the imaging properties for these tracers are ongoing, and several of them have been compared in preclinical and clinical studies [34–36]. However, the results of these studies are non-conclusive, and further investigations are warranted before deciding for the optimal tracer and to facilitate comparative analyses from studies using different tracers.

In addition to pre-clinical and clinical studies, mathematical simulations have been used as a more theoretical approach to investigate the imaging properties of hypoxia PET tracers under a variety of conditions [39]. For simulating oxygen and tracer distributions in the tumor microenvironment, several approaches have been used. These included methods using Green's function, finite difference and finite element methods [39, 108], or the heat kernel [70], carried out in two-dimensional

(2D) [39, 108] or 3D [70, 110].

The hypothesis of this study is that the imaging characteristics of hypoxia PET tracers vary according to their respective physical and chemical properties and can therefore be studied based on mathematical simulations. Major goal was to investigate the imaging properties of the tracers FMISO, FAZA, and HX4 by mathematically simulating their diffusion-retention properties on the basis of 2D models of tumor vasculature. Using this method, the interdependence between clearance, diffusion and image contrast was investigated.

6.2 Material and Methods

Dedicated hypoxia PET tracers are bound to cells depending on the local oxygen concentration. Therefore, to simulate hypoxia PET signals, a two-step process is used: 1) Simulation of the diffusive oxygen supply from blood vessels that is in equilibrium with cellular oxygen consumption (steady state); and 2) modeling of tracer diffusion and retention depending on its specific diffusion and clearance properties as well as the previously simulated oxygen distributions. In this work, a mathematical model has been used which has been described in detail before [39]. A brief description of the model is given here.

6.2.1 Simulation of steady-state oxygen distribution

Oxygen distribution is described as the steady-state of oxygen diffusion and consumption, which can be modeled by a reaction diffusion equation [13], where oxygen consumption was modeled by a Michaelis-Menten relationship:

$$\frac{\partial P}{\partial t} = D_{O_2} \nabla^2 P - \frac{M_0 \cdot P}{P + P_0} \tag{6.1}$$

where P is the local oxygen partial pressure, P_0 is the Michaelis-Menten coefficient of oxygen consumption, D_{O_2} is the diffusion coefficient and M_0 is maximum oxygen consumption rate. This diffusion problem can be solved by using a Gaussian fundamental solution [70]:

$$G_{O_2}(x, y, t) = k_{O_2} \cdot t^{-1} \cdot \mathrm{e}^{\frac{x^2+y^2}{4D_{O_2} \cdot t}} \tag{6.2}$$

where D_{O_2} is the diffusion coefficient and k_{O_2} is a normalization factor chosen in a way that

$$\int_0^\infty \int_0^\infty G_{O_2}(x, y, t) dx dy \equiv 1 \tag{6.3}$$

Using the fundamental solution of the diffusion equation assumes that the initial distribution at $t = 0$ can be described as a δ-function. As each pixel on the vessel map was regarded as a separate oxygen source of a size of approximately 2.5×2.5 μm^2 and thus much smaller than the distance of hypoxic regions from the vessels, this was judged to be a valid approximation [70]. Therefore, if the initial pO_2

distribution is known, pure diffusion at any point in time can be determined by convolving the initial oxygen distribution with the diffusion kernel.

However, since the oxygen consumption is a function of oxygen partial pressure, the model was run repeatedly with time steps of 10 ms, as proposed in a previous study [70]. Oxygenation was calculated iteratively for each pixel, taking into account the local oxygen consumption. Within blood vessels, the initial value of $P = 40$ mmHg was kept constant. The simulation was repeated until a steady state was reached, i.e. a change of less than 0.1% between two iterations was used as a convergence criterion.

Our simulations were carried out in 2D, therefore, the following equations are specific for 2D, but the model can easily be extended to perform 3D simulations [70].

6.2.2 Simulation of hypoxia tracer distribution and uptake

Similar to the oxygen distribution, the distribution and uptake of hypoxia PET tracers was simulated by a numerical solution of the respective reaction-diffusion equation [39], where C_f is the concentration of free tracer and $K(P)$ accounts for tracer binding depending on oxygen levels and cell viability:

$$\frac{\partial C_f}{\partial t} = D_T \nabla^2 C_f - K(P) C_f \tag{6.4}$$

Nitroimidazoles are transported through tumor tissue solely by diffusion. Therefore, the fundamental solution of the diffusion equation was also applied here to create a convolution kernel analogous to the oxygenation model, with time steps of 1 second:

$$G_T(x, y, t) = k_T \cdot t^{-1} \cdot \mathrm{e}^{\frac{x^2+y^2}{4D_T \cdot t}} \tag{6.5}$$

The method gave 2D results comparable to the well established but computationally more expensive finite element method that was used in [39].

6.2.3 Blood activity curves

The blood activity curves that were used as input functions for the simulations were derived from clinical dynamic PET images (FMISO: n= 10, FAZA: n = 3, HX4: n = 5).

FMISO and FAZA scans were acquired in a GE Advance scanner (GE Medical Systems, Milwaukee, WI, USA). Images were acquired in dynamic acquisition mode with a slice thickness of 4.25 mm, and a pixel spacing of 4.3 mm. Reconstruction was performed using OSEM 2D with four iterations and eight subsets. A scatter correction (convolution subtraction) was applied. The FMISO group included 10 patients aged 57–71 years, including seven men and three women, while the FAZA group consisted of three men aged 58–66 years, both suffering from HNSCC.

For HX4, five non-small cell lung cancer (NSCLC) patients were imaged in a Philips Gemini TF 64 PET/CT scanner (Philips Healthcare, Best, The Netherlands). The imaging parameters were set to an axial field of view of 18 cm, slice thickness of 4 mm, in plane pixel spacing of 4 mm, and a spatial resolution of approximately 5 mm FWHM. CT-based attenuation correction and scatter correction (SS-SIMUL) were performed. Image reconstruction was performed using 3D ordered-subset iterative time-of-flight reconstruction technique (BLOB-OS-TF) using three iterations and 33 subsets. The field-of-view for computed tomography (CT) and PET imaging was positioned on the primary tumor. The five patients imaged with HX4 were aged between 59 and 71 years.

From each scan, the tracer concentration in the blood was determined at 20–45 time points over a period of four hours post-injection (p.i.). Blood activity for a given time point was determined by averaging over the activity of six voxels in the heart or a major blood vessel for each patient. This was followed by fitting to the following function to the data:

$$A(t) = A_1 \mathrm{e}^{\frac{-t}{\tau_1}} + A_2 \mathrm{e}^{\frac{-t}{\tau_2}} \tag{6.6}$$

For each parameter, the average was taken over all patients of the same group to derive an average input function (AIP) for all three tracers individually. For the calculations of the standard deviation, the 95% confidence interval of each fit was taken into account.

6.2.4 Parameters

The oxygen and hypoxia PET tracer model parameters used for these simulations were derived from previous publications and are listed in Table 6.1.

Tracer diffusion coefficients were calculated as average of the two formulas presented by Pruijn et al. [120], which estimate the diffusion coefficient of tirapazamine analogs through multicellular layers based on their partition coefficient and molecular structure.

Partition coefficients were taken from literature, except for FAZA, for which published values varied by several orders of magnitude [36,37]. Therefore, we used the simulation softwares XLOGP3, ALOGPS 2.1, Molinspiration and LogKow and took the average of the simulated values as suggested in [133].

The parameter P_1, the pO_2 at which the FMISO binding rate is half-maximal, was taken from [39] and [127]. For FAZA and HX4, the same parameter was used as their uptake follows the same binding mechanism [23, 146].

6.2.5 Simulation details

All simulation steps were implemented in MATLAB R2009b.

Simulations were carried out on vessel maps derived from tumor xenografts which were immunohistochemically stained for CD31, a marker of endothelial tissue. Tissue sections were obtained as described before [138]. Based on this,

Table 6.1: Simulation parameters used for calculation of the steady state oxygen and tracer distribution. Bold font indicates the value chosen for this simulation out of a range of values.

Symbol	Meaning	Value		
P_{ie}	Intraerythrocyte pO_2 in tumors	40 mmHg [39, 108]		
D_{O_2}	O_2 diffusion coefficient	$2 \times 10^{-9}\,m^2/s$ [39]		
M_O	Maximum O_2 consumption rate	15 mmHg/s [39, 108]		
P_O	Michaelis-Menten coefficient of oxygen consumption	(**2.0** − 2.5) mmHg [39, 108]		
		FMISO	FAZA	HX4
M	Molecular weight	189.14	247.18	269.22
D_T	Tracer diffusion coefficient $[\cdot 10^{-11} m^2/s]$	7.90	2.99	3.55 [120]
P	Partition coefficient	0.41	0.30	0.20 [100, 136]
P_1	pO_2 inhibiting binding by 50%	(0.8 − **1.5**) mmHg [39, 127, 146]		

simulations of oxygen distributions and tracer diffusion-retention over a period of four hours p.i. were performed for six different vessel maps.

Vessel maps were divided into 1×1 mm^2 subsections. For each of those, the median pO_2 (mpO2) and tracer activity was determined. Sections with an mpO2 of 35 ± 0.2 mmHg and 2.5 ± 0.2 mmHg were chosen to represent normoxic and hypoxic tissue areas, respectively. Their mean tracer activities at different time points p.i. were then used to generate normoxic and hypoxic time activity curves (TACs). Image contrast ($K(t)$) was defined as the ratio between the mean signal in hypoxic tissue (S_{hyp}) and normoxic tissue (S_{norm}).

$$K(t) = \frac{S_{hyp}(t)}{S_{norm}(t)} \tag{6.7}$$

TACs and contrast results were compared using a Wilcoxon rank-sum test for median and a Levene test for variance using MATLAB R2009b. p-values equal or lower than 0.05 were considered significant.

6.3 Results

6.3.1 Blood activities

For all three investigated hypoxia PET tracers, the average fit parameters for the input functions are listed in Table 6.2. HX4 has the highest clearance rate ($\tau_{2,HX4} = 11.8 \cdot 10^{-5} s^{-1}$), followed by FAZA ($\tau_{2,FAZA} = 4.3 \cdot 10^{-5} s^{-1}$) and FMISO ($\tau_{2,FMISO} = 1.9 \cdot 10^{-5} s^{-1}$). Clearance is significantly different for all tracers. τ_1, the tracer wash-in, was significantly higher for HX4 than for FMISO ($p = 0.037$). HX4 also showed the highest inter-patient variation in clearance, which was significantly higher than for FMISO ($p = 0.047$). All other parameters were

not significantly different. The resulting AIPs with the respective 95% confidence intervals are presented in Figure 6.1.

Table 6.2: Average fit parameters for blood activity of the three tracers and their standard deviation.

	A_1 (kBq/ml)	τ_1 ($\times 10^{-3}$ s^{-1})	A_2 (kBq/ml)	τ_2 ($\times 10^{-5}$ s^{-1})
FMISO	18.11 ± 7.08	2.0 ± 0.71	10.92 ± 2.49	1.90 ± 1.55
FAZA	13.10 ± 4.50	1.30 ± 0.60	13.1 ± 3.70	4.27 ± 1.51
HX4	33.55 ± 12.81	3.10 ± 0.94	12.31 ± 3.27	11.78 ± 5.75

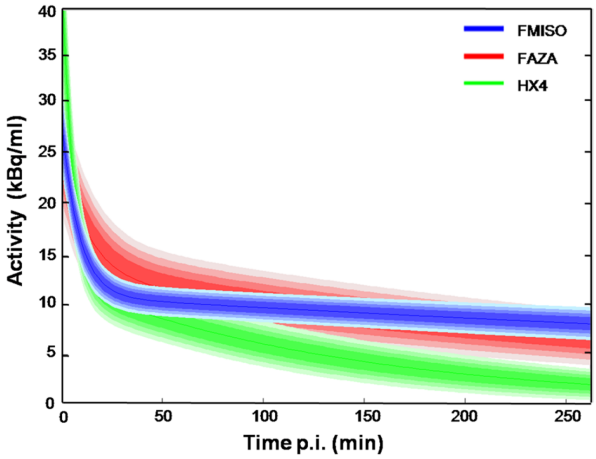

Figure 6.1: Average input function (AIP) for FMISO, FAZA and HX4 over an interval of 4 h post-injection (p.i.). At 4 h p.i., FMISO shows the highest blood activity, followed by FAZA and HX4, reflecting their respective clearance rates (Parameter τ_2). Shaded areas indicate the respective 95% confidence intervals.

6.3.2 Hypoxia contrast for AIPs

Figure 6.2 shows the simulated distributions for FMISO, FAZA and HX4 at two and four hours p.i. for the same xenograft tumor section.

Tracer retention in viable hypoxic tissue areas is already distinguishable at two hours p.i. for all tracers. The distribution patterns for FMISO and FAZA appear almost identical. In contrast, for HX4, the background activity is lower due to the fast tracer clearance. Consequently, less HX4 is retained than FMISO and FAZA, because less unbound HX4 was available during the uptake period. At four hours p.i.,the tracer wash-out caused a decrease in background signal, which is more pronounced for faster clearing tracers. Meanwhile, tracer binding

in hypoxic cells continued. This leads to a net increase of signal in viable hypoxic areas for FMISO, due to the larger supply of free tracer in the blood, and a constant signal for the faster-clearing tracer HX4.

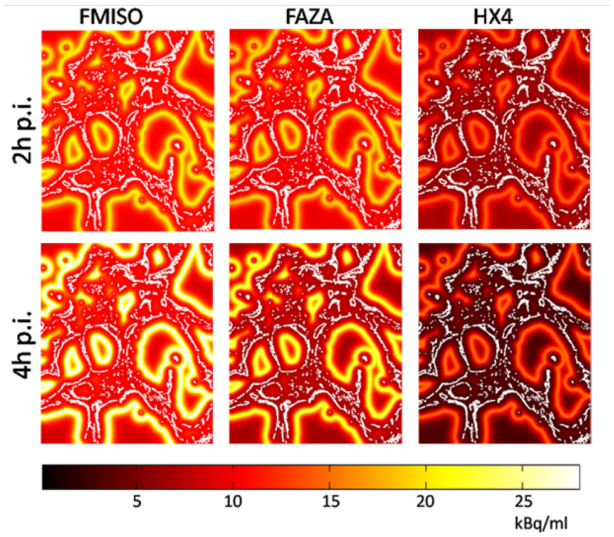

Figure 6.2: Representative simulated activity distributions using average input functions for FMISO, FAZA and HX4 on the same tissue section 2 and 4 h post-injection. Vessels are highlighted in white.

The simulated contrast K(t) of the image signal between hypoxic and normoxic tissue over time is shown in Figure 6.3. For the first hour p.i., there is little difference in contrast which may be due to a low overall effect of the difference in diffusivity of the tracer. For all tracers, contrast continues to increase over time. A faster increase can be observed for tracers with a higher clearance rate, due to a faster elimination of free tracer and a resulting decrease of background signal. In comparison to FMISO, HX4 and FAZA show an image contrast four hours p.i. that is 43% and 3% higher, respectively. Variations in the vascularization patterns of tissue sections with the same median pO2 can affect overall tracer retention in that section. This leads to a standard deviation for contrast at four hours p.i., which is smallest for FMISO (6.9%) and largest for HX4 (11.4%).

6.3.3 Patient-specific input functions

Furthermore, the influence of variations between patient-specific input functions on the resulting contrast four hours p.i. was investigated. Each input function results in a different simulated contrast. Contrast distributions for each tracer are shown in Figure 6.4.

HX4 shows the highest median contrast (2.08, range 1.87–2.73) over all patients, followed by FAZA (1.64, range 1.60–1.70) and FMISO (1.58, range 1.54–1.64), reflecting the clearance behavior of each tracer. The differences for the median

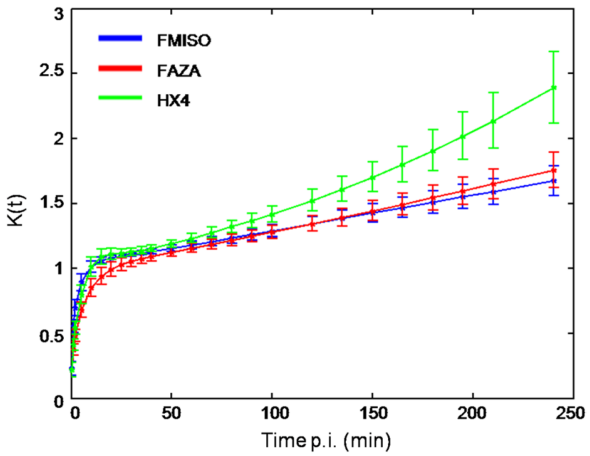

Figure 6.3: Simulated hypoxia (2.5 ± 0.2 mmHg) to normoxia (35 ± 0.2 mmHg) image contrast for the three tracers over an interval of 4 h post-injection. Error bars reflect variations due to different vascularization patterns in tissue sections with identical median oxygen partial pressure.

contrasts tested significant for FMISO and HX4 ($p = 0.001$), as well as FAZA and HX4 ($p = 0.036$), but not for FMISO and FAZA ($p = 0.161$).

Of all tracers, HX4 showed the largest absolute contrast range, which was significantly larger than for FMISO ($p = 0.025$). This reflects a larger inter-patient variation of clearance observed for HX4 which may be due to differences in renal and hepatic clearance between patients. Other significant range differences were not observed.

6.4 Discussion

In this study, we compared three nitroimidazole-based hypoxia PET tracers, which show similar binding properties in hypoxic cells but differ in their diffusion and clearance characteristics. We could show that both parameters have an impact on final image contrast. Based on blood input functions from clinical dynamic PET data, HX4 shows the highest clearance, followed by FAZA and FMISO. This corresponds well to previous clinical and preclinical studies, in which it was found that HX4 has a higher clearance than FMISO, which ultimately leads to higher image contrast [35, 100, 136]. Chen et al. [35] reported that image contrast for HX4 1.5 hours p.i. is the same as for FMISO two hours p.i.. This finding was corroborated by our simulations based on average patient input functions as shown in Figure 6.3.

Tracer uptake in hypoxic cell culture is the same for FMISO and FAZA, suggesting equal nitroreductase affinity for both tracers, which was one of the working assumptions for the simulations. Comparisons between FMISO and FAZA

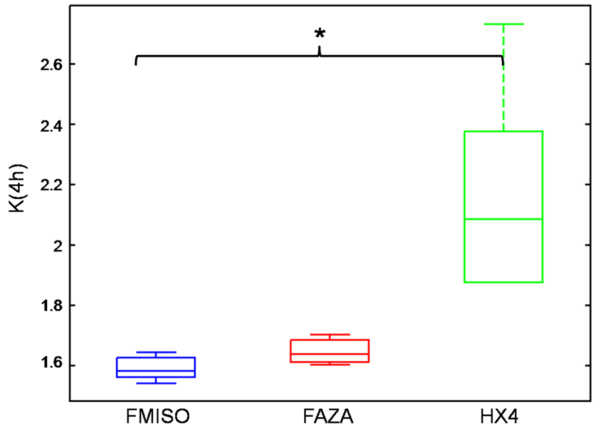

Figure 6.4: Boxplots representing the distributions of contrast 4 h post-injection. Contrast was simulated individually for each patient. The asterisk indicates significant differences in variation.

based on patient data are currently not available. However, overall activity is lower for FAZA than for FMISO in pre-clinical studies, indicating that mechanisms other than enzyme activity, such as tracer clearance and diffusion, are responsible for this observation [34, 36, 99]. The well established hypoxia tracer FAZA has been argued to show better imaging properties than FMISO due to its higher hydrophilicity and increased clearance, although results from earlier pre-clinical studies directly comparing the two tracers regarding better contrast behavior remain non-conclusive [36, 37].

Recently, two preclinical studies have been published that directly compared the imaging properties of the three tracers in the same tumor. Carlin et al. [34] showed a clear superiority of FMISO to HX4 and FAZA in murine models 90 minutes p.i. both in terms of contrast and SUV . Another study by Peeters et al. [99] conducted in rats three hours p.i. found HX4 to be the superior tracer with respect to image contrast, followed by FAZA and FMISO, which is in good agreement with our simulation study. HX4 also showed a faster elimination from the blood as well as lower overall activities and larger ranges compared to FMISO, and the TACs shown in the publication are similar to the simulated activities we observed.

Additionally, the study by Carlin et al. [34] showed good correlation between pimonidazole and all three hypoxia PET tracers, indicating that they accumulate in roughly the same areas and at similar levels of hypoxia, which agrees well with our assumption that the parameter P1, which defines the pO_2 inhibiting tracer binding by 50%, is roughly the same for all three tracers.

In the simulations presented here, contrast four hours p.i. between FMISO and FAZA showed differences of only a few percent despite the fact that FAZA has a significantly higher clearance. When actual patient input functions were used, no

significant difference in contrast four hours p.i. was observed. The lower diffusion coefficient of FAZA leads to a decrease in tracer binding that largely negates the positive influence of its higher clearance rate. The simulations showed that a higher clearance rate leads to lower absolute activities for both FAZA and HX4. Moreover, HX4 showed both the highest clearance and the largest contrast, but also the lowest absolute activity, both in normoxic and hypoxic tissue areas. This has a negative impact on the signal-to-noise ratio (SNR), particularly since hypoxia PET inherently suffers from a low SNR. One option to improve SNR could be to increase the injected activity, however, this would lead to a higher radiation dose to the patient. Another option could be to prolong acquisition time [100]. Diffusion coefficients were calculated using a previously published model. Our value for FMISO was reasonably close to the experimental value for the related compound misonidazole ($D05.5 \cdot 10^{-}11$ m^2/s) [39]. Consequently, it was assumed that the approach is valid for FAZA and HX4 as well. However, diffusion can vary significantly between different tumor types and even throughout a tumor volume [120]. Nonetheless, the simulation model is insensitive to changes in diffusion coefficient, with activity changes of less than 5% at two hours p.i. for variations of 50% in the diffusion coefficient. Therefore, any errors caused by the modeling of partition coefficients and, based on this, the diffusion coefficient, should have a negligible impact on the simulation results.

Regarding the use of parameters derived from literature, there is a large range of values particularly for the parameters used for the simulation of oxygen distribution. Most of this variation is likely to be caused by variation between cell lines. We found that while changes in these parameters sometimes have a visible impact on tracer retention and image contrast, they affect all tracers equally. This ultimately leads to no change in the ranking of tracers regarding image contrast and image contrast variation. Even though the simulations shown here were performed in 2D only, the method can easily be extended to 3D, and has originally been developed for this purpose [70]. Previous publications have shown that oxygen distributions do not strongly depend on whether simulations have been carried out in 2D or 3D [110]. This suggests that 2D comparison of hypoxia PET tracer simulations are an adequate and computationally far less expensive approximation. Two sources of signal uncertainties were investigated: variations of vascular patterns in tissue areas with approximately the same median pO2, and variations of blood activity curves between patients. Changes in the vascular pattern introduced absolute signal changes of 5–8%, which can lead to contrast variations of 7–11%. HX4 showed the highest susceptibility to these contrast changes, but the overall differences between tracers were too small to justify a preference for one tracer over the others. More relevant for clinical application is the inter-patient variability of clearance. FMISO is eliminated mostly through the entero-hepatic pathway, while HX4 and FAZA are also cleared via renal excretion [157]. HX4 clearance and, to a lesser extent, FAZA clearance is therefore also dependent on patient kidney function, and may hence affect the suitability for patients treated with (concurrent) nephrotoxic systemic agents. This adds

variability to the total rate at which the tracer is cleared from the system, resulting in larger absolute ranges of clearance rates. Consequently, the final contrast four hours p.i. between hypoxic and normoxic tissue areas varies much more for HX4 than for FMISO. This can be of concern for clinical imaging since the large differences between patients make it difficult to find a reliable threshold value to define tumor hypoxia.

Acquisition modes and patient collectives varied between institutions. This might affect the PET scans used for the determination of blood input functions. Only blood activity was determined from the scans, which should be mostly unaffected by patient gender or the type of tumor. Test runs showed that changes in relative signal which may result from different acquisition modes have no impact on the simulated contrast. Nonetheless, an impact on the results cannot be completely ruled out. Also, the number of patients in this study is rather small, particularly for FAZA and HX4. Therefore, a preclinical or even clinical validation of the simulation results by conducting PET imaging of all three tracers in the same test subject would be required to fully validate the results of this simulation study.

6.5 Conclusion

According to the simulations in this study, HX4 showed the highest clearance and image contrast and the lowest background signal, followed by FAZA and FMISO, but also the largest variance between patients, both in clearance and contrast. Differences in vascularization patterns are an additional source of signal variance, causing an uncertainty of 7–11%. HX4 is a promising tracer providing PET images with a higher contrast than FAZA and FMISO, whereas FMISO is a very reproducible hypoxia tracer, however with a lower image contrast. The results agree well with previously published preclinical data, showing that tracer clearance is the key factor in determining image contrast.

6.6 Acknowledgments

This project was financially supported by the German Research Foundation (DFG), grant no. TH 1528/1-1. HX4 PET data were provided by the Department of Radiation Oncology (MAASTRO), GROW – School for Oncology and Developmental Biology, Maastricht, The Netherlands, acquired with financial support from the CTMM framework (AIR FOR CE project), EU 6th and 7th framework program (ARTFORCE and METOXIA program).

Declaration of interest: The authors report no conflicts of interest. The authors alone are responsible for the content and writing of the paper.

7 Conclusion and outlook

Concluding discussion

Hypoxia imaging using nitroimidazole-based tracers such as FMISO is currently the most promising approach under investigation for the non-invasive, 3D-resolved detection of hypoxia in tumors. Nonetheless, the exact biochemical and pharmacokinetical processes resulting in the final image are complex and as of now, not thoroughly understood. In this thesis, the problem is approached on a microscopic scale, using a simulation tool that models tracer diffusion and retention on realistic tumor vessel maps in two- and three-dimensional tumor models. The model has been validated and used for the investigation of the impact that clearance and diffusion of various tracers have on resulting image contrast. In the following section, conclusions from the performed studies are summarized and their limitations and potential are discussed in more detail.

In part I, a first step towards validation is taken. The goal was to achieve good correlation between simulated FMISO retention and experimental parameter stainings by optimizing the parameter M_0, representing maximum oxygen consumption. The study showed that good correlation between FMISO simulation and pimonidazole staining can be achieved in many cases if an optimal M_0 is chosen. An additional finding was that the optimal M_0 differed significantly between cell lines, which is in good agreement with published literature [45, 123]. Also, we observed that correlation results improved if only vessels that were positive for perfusion marker Hoechst 33342 were included in the vessel map. In summary, this study showed that the simulation method can yield results close to those observed *in vivo*, which was a prerequisite to attempt a 3D validation.

A major shortcoming of this study was that most optimized values for M_0 were at the lower end of the literature range. Median optimized results for M_0 were located between 2.1-4.6 mmHg/s for the studied cell lines, while the literature range contained values ranging from 2.7-33.5 mmHg/s. The reason for this lies in the 2D simulation approach. As it does not include out-of-plane contributions to oxygen distribution, the total amount of hypoxia is over-estimated, an effect which has been corroborated by another study [112]. Therefore, optimization of maximum oxygen consumption rate for highest agreement with pimonidazole leads to an underestimation of M_0 in the 2D scenario.

A full 3D validation was performed in part II. Here, two xenograft tumors which had been imaged using preclinical FMISO PET were cut in 120 consecutive sec-

tions used to reconstruct the 3D vessel architecture and pimonidazole accumulation. Simulated and stained hypoxic fractions were compared for both tumors. Also, sensitivity and specificity were determined along with the mean distance to agreement for wrongly classified voxels. The results showed that the 3D simulation consistently fared better for all quality measures. The results revealed that the reason for the poorer performance of the 2D simulation was due to its underestimation of tissue oxygenation caused by missing out-of-plane diffusion. Simulated activity was confirmed using the preclinical PET imaging data, which was available for one tumor, showing good agreement for both simulation approaches.

These results are encouraging and suggest a high reliability of results produced by the 3D simulation approach. Being able to simulate tracer TACs on vessel maps that provide information on microscopic structure offers the chance to match TAC shape of subvolumes to certain histological features. This can be a promising approach to help interprete clinical PET images and may ultimately help improve imaging protocols. For this purpose, studying a higher number of tumors for additional verification is advisable.

An application of the simulation model is presented in part III. Here, three nitroimidazole-based tracers, FMISO, FAZA and HX4, were compared. Many tracers for the detection of hypoxia have been developed in the last decades in an attempt to improve image contrast, which is relatively low for the oldest tracer FMISO [23]. Therefore, attempts have been made to develop faster-clearing tracers to reduce background activity, leading to a higher signal-to-noise ratio [72, 100].

Blood activity curves for the simulation time of 4 h p.i. were obtained from clinical PET scans and revealed HX4 to be the fastest-clearing tracer. Consequently, it showed the highest contrast at 4 h p.i. due to its low level of background activity. However, it also showed the highest variation of clearance between patients, which is probably a result of varying patient kidney function. This results in a highly variable image contrast, which makes the selection of a fixed threshold to define hypoxia from static images questionable. The impact of tracer diffusion on image quality was negligible.

Despite being published before the validation studies, the conclusions drawn from the tracer comparison in part III are not invalid. The simulation used the same standard values as in part II, with the exception of K_{max}, for which an experimental literature value has been published only very recently [45].

The first major difference is the use of vessel maps. While the validation studies used vessel maps built to reflect actual perfusion status as closely as possible by removing unperfused vessels, this was not the case in part III. Here, one needs to keep in mind that while it is necessary for validation to reconstruct the tumor vasculature of a specific tumor as realistically as possible to reproduce pimonidazole patterns observed in that tumor, this is not necessary for tracer comparison. Here, the goal was to study the impact of tracer pharmacokinetics

on image contrast, for which the exact vessel architecture is secondary, as long as the same architecture is used for all tracers.

Figure 7.1 shows the impact of clearance on contrast for 2D and 3D simulations. The two curves are very similar. The clearance values chosen for these simulations are close to those observed for FAZA and HX4. As tissue areas with a pre-defined pO_2 rather than predefined tissue areas are compared, the error introduced to the oxygen distribution due to lacking out-of-plane diffusion has no impact on the results. Therefore, only tracer-intrinsic properties are compared, and tracer diffusion and retention is mostly independent on the mode of simulation chosen (Figure 5.6). Therefore, the conclusions drawn in part III are not invalidated by being based on 2D simulations only. Recently, a new value has been published

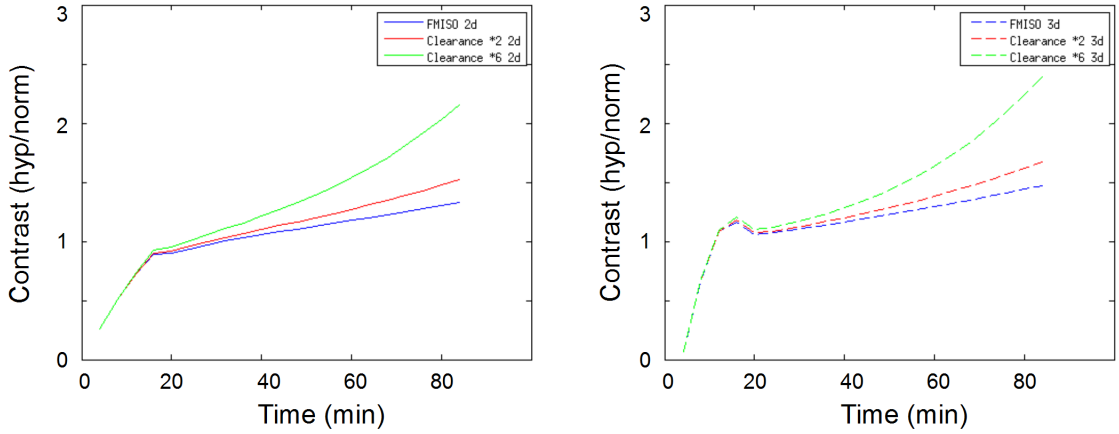

Figure 7.1: Graphs showing the impact of clearance on contrast between normoxic (30 mmHg) and hypoxic (2.5 mmHg) tissue sections, simulated in 2D (left) and 3D (right). The clearance rates are approximately equal to the clearance observed for FAZA (double FMISO clearance and HX4 (sixfold FMISO clearance).

for the parameter K_{max}, which gives the maximum tracer retention rate. The results presented in part III were obtained using the old value. This means that the results presented here likely underestimate overall retained activity, and the resulting contrast for each tracer. However, as this parameter change affects all tracers equally, the main observations, e.g. increased clearance resulting in higher image contrast, still hold true.

Whether a full 3D simulation on realistic vascular models is necessary or if a 2D simulation and/or artificial vessel maps will suffice, depends on the study goal. If the oxygen distribution plays a key role in the study design, such as for the investigation of the effects of acute hypoxia, a realistic 3D model is the better choice. However, if the problem under investigation is a tracer-intrinsic property that is mostly independent of the tumor vasculature, such as studying the impact of tracer clearance, 2D simulations, even on artificial vessel maps, will

be a sufficient and time-efficient alternative.

Outlook

PET imaging using nitroimidazole-based tracers like FMISO has been validated as a non-invasive method for hypoxia imaging in human tumors. In combination with other imaging modalities, such as PET/CT for treatment planning, there is great potential for it to become established as a foundation for biologically adaptive therapy approaches such as dose painting.

In combined PET/MRI systems, the information obtained from FMISO PET can be complemented with functional MR sequences, such as diffusion-weighted MRI. The combination of multiple functional imaging techniques offers a lot of promise for further stratification of patient subgroups and a greater individualization of cancer treatment.

There is a lot of future potential for the simulation tool presented here. Simulations can offer the missing link between microscopic oxygenation levels and the resulting macroscopic hypoxia PET image. The available information on simulated activity and microscopic tissue phenotype can be used to better understand PET image formation. The impact of changing tracer properties on the shape of TACs can be simulated, which can help develop dynamic imaging protocols for tracers beside FMISO in addition to clinical studies. The simulation model can be used in the planning phase of clinical and preclinical studies for study design and an estimatation of the results to be expected.

8 Bibliography

[1] Becker N WJ: *Krebsatlas der Bundesrepublik Deutschland 1981-1990: Fortschreibung im Internet: www.krebsatlas.de*. Springer, Berlin Heidelberg New York 1998, [[www.krebsatlas.de]].

[2] Delaney G, Jacob S, Featherstone C, Barton M: **The role of radiotherapy in cancer treatment: estimating optimal utilization from a review of evidence-based clinical guidelines**. *Cancer* 2005, **104**(6):1129–1137.

[3] Röntgen WC: *Ueber eine neue Art von Strahlen (Vorläufige Mittheilung)*. Stahel'sche K. Hof- und Universitätsbuch- und Kunsthandlung 1896.

[4] Cossmann PH: *Medizinische Strahlentherapie*. Springer-Verlag Berlin 2011. [Kapitel 33 589].

[5] Coutard H: **Principles of X Ray Therapy of Malignant Diseases**. *The Lancet* 1934, **224**:5784–5791.

[6] Regaud C: **The influence of the duration of irradiation on the changes produced in the testicle by radium**. *International Journal of Radiation Oncology • Biology • Physics* 1977, **2**:565 – 567.

[7] Frey H: **Experimentelle Untersuchungen Über Die Röntgensensibilität der Nebennieren**. *Acta Radiologica* 1928, **8**:23–53.

[8] Kerst DW: **Acceleration of Electrons by Magnetic Induction**. *Physical Review* 1940, **58**:841.

[9] Thwaites DI, Tuohy JB: **Back to the future: the history and development of the clinical linear accelerator**. *Phys Med Biol* 2006, **51**(13):R343–362.

[10] Bushberg JT, Seibert JA, Leidholdt EM, Boone JM: *The Essential Physics of Medical Imaging - Third Edition*. Lippincott Williams & Wilkins 2012.

[11] Alber M, Thorwarth D, Ganswindt U, Belka C: *Radioonkologie: Grundlagen, Volume 1, 2nd edition*, Zuckschwerdt, München 2009 chap. Fluenzmodulierte Strahlentherapie (IMRT), :189–201.

[12] Webb S: **The physical basis of IMRT and inverse planning**. *Br J Radiol* 2003, **76(910)**:678–689.

[13] Teoh M, Clark C, Wook K, Whitaker S, Nisbet A: **Volume modulated arc therapy: a review of current literatureand clinical use in practice**. *Br J Radiol* 2011, **84(1007)**:967–996.

[14] Budach V, Stuschke M, Budach W, Baumann M, Geismar D, Grabenbauer G, Lammert I, Jahnke K, Stueben G, Herrmann T, Bamberg M, Wust P, Hinkelbein W, Wernecke K: **Hyperfractionated accelerated chemoradiation with concurrent fluorouracil-mitomycin is more effeffect than dose-escalated hyperfractionated accelerated radiation therapy alone in locally advanced headand neck cancer: final results of the radiotherapy cooperative clinical trial group of the German Cancer Society 95-06 Prospective Randomized Trial**. *J Clin Oncol* 2005, **23**:1125–1135.

[15] Linge A, Lohaus F, Loeck S, Nowak A, Gudziol V, Valentini C, von Neubeck C, Jütz M, Tinhofer I, Budach V, Sak A, Stuschke M, Balermpas P, Rödel C, Grosu AL, Abdollahi A, Debus J, Ganswindt U, Belka C, Pigorsch S, Combs S, Mönnich D, Zips D, Buchholz F, Aust DE, Baretton G, Thames H, Dubrovska A, Alsner J, Overgaard J, Krause M, Baumann M: **HPV status, cancer stem cell marker expression, hypoxia gene signaturesand tumour volume identify good prognosis subgroups in patients with HNSCC after primary radiochemotherapy: A multicentre retrospective study of the German Cancer Consortium Radiation Oncology Group (DKTK-ROG)**. *Radiother Oncol* 2016, **In press**.

[16] Lambin P, Rios-Velazquez E, Leiijnaar R, van Stiphout R, Granton P, Zegers C, Gillies R, Boellard R, Dekker A, Aerts H: **Radiomics: extracting more information from medical images using advanced feature analysis**. *European Journal of cancer* 2012, **48**:441–446.

[17] Thorwarth D, Eschmann SM, Holzner F, Paulsen F, Alber M: **Combined uptake of [18F]FDG and [18F]FMISO correlates with radiation therapy outcome in head-and-neck cancer patients**. *Radiother Oncol* 2006, **80**:151–156.

[18] Zips D, Zöphel K, Abolmaali N, Perrin R, Abramyuk A, Haase R, Appold S, Steinbach J, Kotzerke J, Baumann M: **Exploratory prospective trial of hypoxia-specific PET imaging during radiochemotherapy in patients with locally advanced head-and-neck cancer**. *Radiother Oncol* 2012, **105**:21–28.

[19] Ljungkvist ASE, Bussink J, Kaanders JHAM, Rijken PFJW, Begg AC, Raleigh JA, van der Kogel AJ: **Hypoxic cell turnover in different solid tumor lines**. *Int. J. Radiat. Oncol. Biol. Phys.* 2005, **62**(4):1157–1168.

[20] Vaupel P: **Tumor microenvironment physiology and its implications for radiation oncology**. *Semin Radiat Oncol* 2004, **14(3)**:198–206.

[21] Gray LH, Conger AD, Ebert M, Hornsey S, Scott OCA: **The Concentration of Oxygen Dissolved in Tissues at the Time of Irradiation as a Factor in Radiotherapy**. *Br J Radiol* 1953, **26**(312):638–648, [[http://bjr.birjournals.org/content/26/312/638]].

[22] Nordsmark M, Bentzen SM, Rudat V, Brizel D, Lartigau E, Stadler P, Becker A, Adam M, Molls M, Dunst J, Terris DJ, Overgaard J: **Prognostic value of tumor oxygenation in 397 head and neck tumors after primary radiation therapy. An international multi-center study**. *Radiother Oncol* 2005, **77**:18–24.

[23] Horsman MR, Mortensen LS, Petersen JB, Busk M, Overgaard J: **Imaging hypoxia to improve radiotherapy outcome**. *Nat Rev Clin Oncol* 2012, **9**(12):674–687.

[24] Adams G, Cooke M: **Electron-affinic sensitization. I: A structural basis for chemical radiosensitizers in bacteria**. *Int J Radiat Biol Relat Stud Phys Chem Med* 1969, **15(5)**:457–471.

[25] Koh W: **Imaging of hypoxia in human tumors with [18F] fluoromisonidazole**. *Int J Radiat Oncol Biol Phys* 1992, **22**:199–212.

[26] Rasey J, Koh W, Evans M, Peterson L, Lewellen T, Graham M, Krohn K: **Quantifying regional hypoxia in human tumors with positron emission tomography of [18F]fluoromisonidazole: a pretherapy study of 37 patients**. *Int J Radiat Oncol Biol Phys* 1996, **36(2)**:417–428.

[27] Thorwarth D, Eschmann SM, Scheiderbauer J, Paulsen F, Alber M: **Kinetic analysis of dynamic 18F-fluoromisonidazole PET correlates with radiation treatment outcome in head-and-neck cancer**. *BMC Cancer* 2005, **5**:152.

[28] Hoskin P, Saunders M, Dische S: **Hypoxic radiosensitizers in radical radiotherapy for patients with bladder carcinoma: hyperbaric osygen, misonidazole,and accelerated raiotherapy, carbogen,and nicotinamide**. *Cancer* 1999, **86(7)**:1322–1328.

[29] Kumar S, Singh R, Meena R: **Emerging targets for radioprotection and radiosensitization in radiotherapy**. *Tumour Biology* 2016, **37(9)**:11589–11609.

[30] Ling CC, Humm J, Larson S, Amols H, Fuks Z, Leibel S, Koutcher JA: **Towards multidimensional radiotherapy (MD-CRT): biological imaging and biological conformality**. *Int. J. Radiat. Oncol. Biol. Phys.* 2000, **47**(3):551–560.

[31] Thorwarth D, Eschmann SM, Paulsen F, Alber M: **Hypoxia dose painting by numbers: a planning study**. *Int. J. Radiat. Oncol. Biol. Phys.* 2007, **68**:291–300.

[32] Galvin J, De Neve W: **Intensity modulating and other radiation therapy devices for dose painting**. *J Clin Oncol* 2007, **25**:924–930.

[33] Rajendran JG, Schwartz DL, O'Sullivan J, Peterson LM, Ng P, Scharnhorst J, Grierson JR, Krohn KA: **Tumor Hypoxia Imaging with [F-18] Fluoromisonidazole Positron Emission Tomography in Head and Neck Cancer**. *Clin Cancer Res* 2006, **12**(18):5435–5441.

[34] Carlin S, Zhang H, Reese M, Ramos NN, Chen Q, Ricketts SA: **A Comparison of the Imaging Characteristics and Microregional Distribution of 4 Hypoxia PET Tracers**. *J Nucl Med* 2014, **55**(3):515–521, [[http://jnm.snmjournals.org/content/55/3/515]].

[35] Chen L, Zhang Z, Kolb HC, Walsh JC, Zhang J, Guan Y: **[18F]-HX4 hypoxia imaging with PET/CT in head and neck cancer: a comparison with [18F]-FMISO**. *Nucl Med Commun* 2012, **33**(10):1096–1102.

[36] Sorger D, Patt M, Kumar P, Wiebe LI, Barthel H, Seese A, Dannenberg C, Tannapfel A, Kluge R, Sabri O: **[18F]Fluoroazomycinarabinofuranoside (18FAZA) and [18F]Fluoromisonidazole (18FMISO): a comparative study of their selective uptake in hypoxic cells and PET imaging in experimental rat tumors**. *Nucl. Med. Biol.* 2003, **30**(3):317–326.

[37] Piert M, Machulla HJ, Picchio M, Reischl G, Ziegler S, Kumar P, Wester HJ, Beck R, McEwan AJB, Wiebe LI, Schwaiger M: **Hypoxia-specific tumor imaging with 18F-fluoroazomycin arabinoside**. *J. Nucl. Med.* 2005, **46**:106–113.

[38] Kelly CJ, Brady M: **A model to simulate tumour oxygenation and dynamic [18F]-Fmiso PET data**. *Phys Med Biol* 2006, **51**(22):5859–5873.

[39] Mönnich D, Troost EGC, Kaanders JHAM, Oyen WJG, Alber M, Thorwarth D: **Modelling and simulation of [18F]fluoromisonidazole dynamics based on histology-derived microvessel maps**. *Phys Med Biol* 2011, **56**(7):2045–2057.

[40] Mönnich D, Troost EGC, Kaanders JHAM, Oyen WJG, Alber M, Thorwarth D: **Modelling and simulation of the influence of acute and chronic hypoxia on [18F]fluoromisonidazole PET imaging**. *Phys Med Biol* 2012, **57**(6):1675–1684.

[41] Mönnich D, Troost EGC, Kaanders JHAM, Oyen WJG, Alber M, Zips D, Thorwarth D: **Correlation between tumor oxygenation and 18F-fluoromisonidazole PET data simulated based on microvessel images**. *Acta Oncol* 2013, **52**(7):1308–1313.

[42] Dalah E, Bradley D, Nisbet A: **A mathematical approach towards simulating a realistic tissue activity curve of 64Cu-ATSM for the purpose of sub-target volume delineation in radiotherapy**. *Nuclear Instruments and Methods in Physics Research Section A: Accelerators, Spec-*

trometers, Detectors and Associated Equipment 2010, **619**(1-3):283–286, [[http://adsabs.harvard.edu/abs/2010NIMPA.619..283D]].

[43] Dalah E, Bradley D, Nisbet A: **Simulation of tissue activity curves of (64)Cu-ATSM for sub-target volume delineation in radiotherapy**. *Phys Med Biol* 2010, **55**(3):681–694.

[44] Bowen SR, van der Kogel AJ, Nordsmark M, Bentzen SM, Jeraj R: **Characterization of positron emission tomography hypoxia tracer uptake and tissue oxygenation via electrochemical modeling**. *Nucl. Med. Biol.* 2011, **38**(6):771–780.

[45] Warren DR, Partridge M: **The role of necrosis, acute hypoxia and chronic hypoxia in (18)F-FMISO PET image contrast: a computational modelling study**. *Phys Med Biol* 2016, **61**(24):8596–8624.

[46] Brem S, Brem H, Folkman J, Findelstein D, Patz A: **Prolonged tumor dormancy by prevention of neovascularization in the vitreous**. *Cancer Res* 1976, **36**:2807–2812.

[47] Vaupel P, Kallinowski F, Okunieff P: **Blood flow, oxygen and nutrient supply, and metabolic microenvironment of human tumors: a review**. *Cancer Res* 1989, **49(23)**:6449–6465.

[48] Dewhirst MW, Cao Y, Moeller B: **Cycling hypoxia and free radicals regulate angiogenesis and radiotherapy response**. *Nat Rev Cancer* 2008, **8**:453–437.

[49] Dewhirst MW: **Concepts of oxygen transport at the microcirculatory level**. *Semin Radiat Oncol* 1998, **8(3)**:143–150.

[50] Krogh A: **The number and distribution of capillaries in muscles with calculation of the oxygen pressure head necessary for supplying the tissue**. *J Physiol Lond* 1918, **52**:409–415.

[51] Krogh A: **The rate of diffusion of gases through animal tissues, with some remarks on the coefficient of invasion**. *J. Physiol. Lond.* 1918, **52**:391–408.

[52] Thomlinson RH, Gray LH: **The Histological Structure of Some Human Lung Cancers and the Possible Implications for Radiotherapy**. *Br J Cancer* 1955, **9**(4):539–549, [[http://www.ncbi.nlm.nih.gov/pmc/articles/PMC2073776/]].

[53] Chaplin D, Olive P, Durand RE: **Intermitttent blood flow in a murine tumor: radiobiological effects**. *Cancer Res* 1987, **47**:597–601.

[54] Kimura H, RD B, ET O, Hsu R, Secomb TW, Papahadjopoulos D, Hong K, Dewhirst MW: **Fluctuations in red cell flux in tumor mmicrovessels can lead to transient hypoxia and reoxygenation in tumor parenchyma**. *Cancer Res* 1996, **56(23)**:5522–5528.

[55] Bayer C, Shi K, Astner S, Maftei C, Vaupel P: **Acute versus chronic hypoxia: why a simplified classification is simply not enough**. *Int J Radiat Oncol Biol Phys* 2011, **80**:965–968.

[56] Denekamp J, Dasu A: **Inducible repair and the two forms of tumour hypoxia - time for a paradigm shift**. *Acta Oncol* 2007, **38**:903–918.

[57] Rofstad EK, Gaustad JV, Egeland TA, Mathiesen B, Galappathi K: **Tumors exposed to acute cyclic hypoxic stress show enhanced angiogenesis, perfusion and metastatic dissemination**. *Int J Cancer* 2010, **127**(7):1535–1546.

[58] Kirkpatrick J, Cardenas-Navia L, Dewhirst MW: **Predicting the effect of temporal variations in PO2 on tumor radiosensitivity**. *Int J Radiat Oncol Biol Phys* 2004.

[59] Alexander P, Charlesby A: **Energy transfer in macromolecules exposed to ionizing radiations**. *Nature* 1954, **273**:578–579.

[60] Johansen I, Howard-Flanders P: **Macromolecular repair and free radical scavenging in the protection of bacteria against X-rays**. *Radiat. Res.* 1965, **24**:184–200.

[61] Liu C, Lin Q, Yun Z: **Cellular and Molecular Mechanisms Underlying Oxygen-Dependent Radiosensitivity**. *Radiat. Res.* 2015, **183(5)**:487–496.

[62] Kim Y, Lin Q, Zelterman D: **Hypoxia-regulated delta-like I homologue enhances cancer stemnessand tumorigenicity**. *Cancer Res* 2009, **69**:9271–9280.

[63] Mathieu J, Zhou W, Xing Y, Sperber H, Ferreccio A, Agoston Z, Kuppusamy K, Moon R, Ruohola-Baker H: **Hypoxia-inducible factors have distinct and stage-specific roles during reprogramming of human cells to pluripotency**. *Cell Stem Cell* 2014, **14**:592–605.

[64] Graeber T, Osmanian C, Jacks T, Housman D, Koch C, Lowe S, Giaccia AJ: **Hypoxia-mediated selection of cells with diminished apoptotic potential in solid tumours**. *Nature* 1996, **379(6560)**:88–91.

[65] Parija SC: *Textbook of Microbiology and Immunology*. Elsevier Health Sciences 2014. [P. 116].

[66] Troost EGC, Laverman P, Kaanders JHAM, Philippens M, Lok J, Oyen WJG, van der Kogel AJ, Boerman OC, Bussink J: **Imaging hypoxia after oxygenation-modification: comparing [18F]FMISO autoradiography with pimonidazole immunohistochemistry in human xenograft tumors**. *Radiother Oncol* 2006, **80**(2):157–164.

[67] Olive PL, Aquino-Parsons C, Liao SY, Raleigh JA, Lerman MI, Stanbridge EJ: **Carbonic anhydrase 9 as an endogenous marker for hypoxic cells in cervical cancer**. *Cancer Res* 2001, **61(24)**:8924–8929.

[68] Airley RE, Loncaster J, Raleigh JA, Harris AL, Davidson SE, D HR, West CML, Stratford IJ: **GLUT-1 and CAIX as intrinsic markers of hypoxia in carcinoma of the cervix: Relationship to pimonidazole binding**. *Int J Cancer* 2003, **104**:65–91.

[69] Yaromina A, Thames H, Zhou X, Hering S, Eicheler W, Dörfler A, Leichtner T, Zips D, Baumann M: **Radiobiological hypoxia, histological parameters of tumour microenvironment and local tumour control after fractionated irradiation**. *Radiotherapy and Oncology* 2010, **96**:116–122, [[http://www.sciencedirect.com/science/article/pii/S0167814010002768]].

[70] Lagerlöf JH, Kindblom J, Cortez E, Pietras K, Bernhardt P: **Image-based 3D modeling study of the influence of vessel density and blood hemoglobin concentration on tumor oxygenation and response to irradiation**. *Medical Physics* 2013, **40**(2):024101, [[http://link.aip.org/link/?MPH/40/024101/1]].

[71] Höckel M, Schienger K, Aral B, Milze M, Schäffer U, Vaupel P: **Association between Tumor Hypoxia and Malignant Progression in Advanced Cancer of the Uterine Cervix**. *Cancer Res* 1996, **56**:4509–4515.

[72] Mortensen LS, Johansen J, Kallehauge J, Primdahl H, Busk M, Lassen P, Alsner J, Sørensen BS, Toustrup K, Jakobsen S, Petersen J, Petersen H, Theil J, Nordsmark M, Overgaard J: **FAZA PET/CT hypoxia imaging in patients with squamous cell carcinoma of the head and neck treated with radiotherapy: results from the DAHANCA 24 trial**. *Radiother Oncol* 2012, **105**:14–20.

[73] Kikuchi M, Yamane T, Shinohara S, Fujiwara K, Hori Sy, Tona Y, Yamazaki H, Naito Y, Senda M: **18F-fluoromisonidazole positron emission tomography before treatment is a predictor of radiotherapy outcome and survival prognosis in patients with head and neck squamous cell carcinoma**. *Ann Nucl Med* 2011, **25**(9):625–633.

[74] Evans J, PJ C: **Clinical trial of atmospheric oxygen breathing during radiotherapy for cancer of the oropharynx**. *Radiol Clin (Basel)* 1975, **44**:210–213.

[75] Henk J, Kunkler P, Smith C: **Radiotherapy and hyperbaric oxygen in head and neck cancer. Final report of the first concontrol clinical trial**. *Lancet* 1977, **2**:101–103.

[76] Overgaard J: **Hypoxic modification of radiotherapy in squamous cell carcinoma of the head and neck–a systematic review and meta-analysis**. *Radiother Oncol* 2011, **100**:22–32.

[77] Alber M, Paulsen F, Eschmann SM, Machulla HJ: **On biologically conformal boost dose optimization**. *Phys Med Biol* 2003, **48(2)**:N31–N35.

[78] Alessio A, Kinahan P: *Nuclear Medicine* 2006 chap. PET Image Reconstruction.

[79] Horst A: **Numerische Verfahren zur Verbesserung der Ortsauflösung von volumetrischen Bilddaten der Positronen-Emissions-Tomographe für die optimierte Bestrahlungsplanung**. *Master's thesis*, Eberhard Karls Universität Tübingen 2012.

[80] Beyer T, Townsend DW, Brun T, Kinahan PE, Charron M, Roddy R, Jerin J, Young J, Byars L, Nutt R: **A Combined PET/CT Scanner for Clinical Oncology**. *J Nucl Med* 2000, **41**(8):1369–1379.

[81] Sattler B, Lee JA, Lonsdale M, Coche E: **PET/CT (and CT) instumentation, image reconstruction and data transfer for radiotherapy planning.** *Radiother. Oncol.* 2010, **96**:288–297.

[82] van Elmpt W, Öllers M, Dingemans AMC, Lambin P, Ruysscher DD: **Response Assessment Using 18F-FDG PET Early in the Course of Radiotherapy Correlates with Survival in Advanced-Stage Non-Small Cell Lung Cancer**. *J Nucl Med* 2012, **53**(10):1514–1520.

[83] Thorwarth D: **Functional imaging for radiotherapy treatment planning: current status and future directions - a review**. *Br. J. Radiol.* 2015, **88**(1051):20150056.

[84] Sjölund J, Forsberg D, Andersson M, Knutsson H: **Generating patient specific pseudo-CT of the head from MR using atlas-based regression**. *Phys. Med. Biol.* 2015, **60**(2):825–839.

[85] Demol B, Boydev C, Korhonen J, Reynaert N: **Dosimetric characterization of MIRI-only treatment planning for brain tumors in atlas-based pseudo-CT images generated from standard T1-weighed MR images**. *Medical Physics* 2016, **43-12**:6557–6568.

[86] Leibfarth S, Mönnich D, Welz S, Siegel C, Schwenzer N, Schmidt H, Zips D, Thorwarth D: **A strategy for multimodal deformable image registration to integrate PET/MR into radiotherapy treatment planning**. *Acta Oncol.* 2013, **52**(7):1353–1359.

[87] Nestle U, Weber W, Hentschel M, Grosu AL: **Biological imaging in radiation therapy: role of positron emission tomography**. *Phys. Med. Biol.* 2008, **54**:R1–R25.

[88] Warburg O: **On the origin of cancer cells**. *Science* 1956, **123**(3191):309–314.

[89] Gambhir SS, J C, Schwimmer DH J Silverman, Coleman RE, Phelps ME: **A tabulated summary of the FDG literature**. *J. Nucl. Med.* 2001, **42**:1S–93S.

[90] Liu T, Xu W, Yan WL, Ye M, Bai YR, Huang G: **FDG-PET, CT, MRI for diagnosis of local residualr or recurrent nasopharyngeal carcinoma, which one is the best?** *Radiother. Oncol.* 2007, **85**:327–335.

[91] Lebron L, Greenspan D, Pandit-Taskar N: **PET Imaging of Breast Cancer: Role in Patient Management**. *PET Clin* 2015, **10**(2):159–195.

[92] Yap ML, Sun A, Higgins J, Clarke K, Marshall A, Becker N, Le LW, Vines DC, Bezjak A, Bissonnette JP: **Adaptive Dose Escalation using Serial Four-dimensional Positron Emission Tomography/Computed Tomography Scans during Radiotherapy for Locally Advanced Non-small Cell Lung Cancer**. *Clin Oncol (R Coll Radiol)* 2016, **28**(12):e199–e205.

[93] Leibfarth S, Simoncic U, Monnich D, Welz S, Schmidt H, Schwenzer N, Zips D, Thorwarth D: **Analysis of pairwise correlations in multiparametric PET/MR data for biological tumor characterization and treatment individualization strategies**. *Eur. J. Nucl. Med. Mol. Imaging* 2016, **43**(7):1199–1208.

[94] Galldiks N, Langen KJ, Pope WB: **From the clinician's point of view - What is the status quo of positron emission tomography in patients with brain tumor?** *Neuro-Oncology* 2015, **17**(11):1434–1444.

[95] Wagner M, Seitz U, Buck A, Neumaier B, Schultheiß S, Bangerter M, Bommer M, Leithäuser F, Wawra E, Munzert G, Reske SN: **3'-(18F)Fluoro-3'-Deoxythymidine ([18F]-FLT) as Positron Emission Tomography Tracer for Imaging Proliferation in a Murine B-Cell Lymphoma Model and in the Human Disease**. *Cancer Research* 2003, **63**:2681–2687.

[96] Odewole OA, Tade FI, Nieh PT, Savir-Baruch B, Jani AB, Master VA, Rossi PJ, Halkar RK, Osunkoya AO, Akin-Akintayo O, Zhang C, Chen Z, Goodman MM, Schuster DM: **Recurrent prostate cancer detection with anti-3-[(18)F]FACBC PET/CT: comparison with CT**. *Eur. J. Nucl. Med. Mol. Imaging* 2016, **43**(10):1773–1783.

[97] Abolmaali N, Haase R, Koch A, Zips D, Steinbach J, Baumann M, Kotzerke J, Zophel K: **Two or four hour [18F]FMISO-PET in HNSCC. When is the contrast best?** *Nuklearmedizin* 2011, **50**:22–27.

[98] Reischl G, Dorow DS, Cullinane C, Katsifis A, Roselt P, Binns D, Hicks RJ: **Imaging of tumor hypoxia with [124I]IAZA in comparison with [18F]FMISO and [18F]FAZA–first small animal PET results**. *J Pharm Pharm Sci* 2007, **10**(2):203–211.

[99] Peeters SGJA, Zegers CML, Lieuwes NG, van Elmpt W, Eriksson J, van Dongen GAMS, Dubois L, Lambin P: **A Comparative Study of the Hypoxia PET Tracers [18F]HX4, [18F]FAZA,**

and [18F]FMISO in a Preclinical Tumor Model. *International Journal of Radiation Oncology • Biology • Physics* 2014, **0**(0), [[http://www.redjournal.org/article/S0360301614041984/abstract]].

[100] Zegers CML, van Elmpt W, Wierts R, Reymen B, Sharifi H, Ollers MC, Hoebers F, Troost EGC, Wanders R, van Baardwijk A, Brans B, Eriksson J, Windhorst B, Mottaghy FM, De Ruysscher D, Lambin P: **Hypoxia imaging with [(18)F]HX4 PET in NSCLC patients: Defining optimal imaging parameters**. *Radiother Oncol* 2013, **109**:58–64.

[101] Schweifer A, Maier F, Ehrlichmann W, Lamparter D, Kneilling M, Pichler BJ, Hammerschmidt F, Reischl G: **18F-Fluoro-azomycin-2-deoxy–d-ribofuranoside - A new imaging agent for tumor hypoxia in comparison with 18F-FAZA**. *Nucl. Med. Biol.* 2016, **43**(12):759–769.

[102] Brown R: **A brief account of microscopical observations made in the months of June, July and August, 1827, on the particles contained in the pollen of plants; and on the general existence of active molecules in organic and inorganic bodies**. *Philosophical Magazine* 1828, **4**(21):161–173.

[103] Einstein A: **Über die von der molekularkinetischen Theorie der Wärme geforderte Bewegung von in ruhenden Flüssigkeiten suspendierten Teilchen**. *Annalen der Physik* 1905, **322**(8):549–600.

[104] Perrin J: **Mouvement brownien et réalité moléculaire**. *Annales de chimie et de physique* 1909, **8**(18):5–144.

[105] Graham T: **The Bakerian Lecture – On the Diffusion of Liquids**. *Philosophical Transactions of the Royal Society of London* 1850, **140**:1–46.

[106] Fick A: **Über Diffusion**. *Poggendorff's Annalen der Physik* 1855, **94**:59–86.

[107] Haas U: *Physik für Pharmazeuten und Mediziner*. Wissenschaftliche Verlagsgesellschaft mbH Stuttgart, 6. auflage edition 2002.

[108] Daşu A, Toma-Daşu I, Karlsson M: **Theoretical simulation of tumour oxygenation and results from acute and chronic hypoxia**. *Phys Med Biol* 2003, **48**(17):2829–2842.

[109] Daşu A, Toma-Daşu I: **Vascular oxygen content and the tissue oxygenation–a theoretical analysis**. *Med Phys* 2008, **35**(2):539–545.

[110] Espinoza I, Peschke P, Karger CP: **A model to simulate the oxygen distribution in hypoxic tumors for different vascular architectures**. *Medical Physics* 2013, **40**(8):081703.

[111] Lagerlöf JH, Bernhardt P: **Oxygen Distributions - Evaluation of Computational Methods, Using a Stochastic Model for Large Tumour Vasculature, to Elucidate the Importance of Considering a Complete Vascular Network**. *PLoS One* 2016, **11(11)**:1–17.

[112] Grimes DR, Kannan P, Warren DR, Markelc B, Bates R, Muschel R, Partridge M: **Estimating oxygen distribution from vasculature in three-dimensional tumour tissue**. *J R Soc Interface* 2016, **13**(116).

[113] Mönnich D: **Modelling and Simulation of Hypoxia Imaging with Positron Emission Tomography**. *PhD thesis*, Mathematisch-Naturwissenschaftliche Fakultät der Eberhard Karls Universität Tübingen 2013.

[114] Bussink J, Kaanders JH, Rijken PF, Raleigh JA, Van der Kogel AJ: **Changes in blood perfusion and hypoxia after irradiation of a human squamous cell carcinoma xenograft tumor line**. *Radiat. Res.* 2000, **153**(4):398–404.

[115] Rijken PF, Bernsen HJ, Peters JP, Hodgkiss RJ, Raleigh JA, van der Kogel AJ: **Spatial relationship between hypoxia and the (perfused) vascular network in a human glioma xenograft: a quantitative multi-parameter analysis**. *Int J Radiat Oncol Biol Phys* 2000, **48**(2):571–582.

[116] Volger M: *Lichtmikroskopie - Theorie und Anwendung*. Universität Wien 2008.

[117] Reihani SNS, Oddershede LB: **Confocal microscopy of thick specimens**. *JBO Letters* 2009, **14(3)**:030513.

[118] Goldman D: **Theoretical models of microvascular oxygen transport to tissue**. *Microcirculation* 2008, **15**(8):795–811.

[119] Berg JM, Tymoczko JL, Styer L: *Stryer Biochemie 6. Auflage*. Springer Spektrum Akademischer Verlag 2007.

[120] Pruijn FB, Patel K, Hay MP, Wilson WR, Hicks KO: **Prediction of Tumour Tissue Diffusion Coefficients of Hypoxia-Activated Prodrugs from Physicochemical Parameters**. *Aust. J. Chem.* 2008, **61**(9):687–693, [[http://dx.doi.org/10.1071/CH08240]].

[121] Pruijn FB, Sturman JR, Liyanage HDS, Hicks KO, Hay MP, Wilson WR: **Extravascular transport of drugs in tumor tissue: effect of lipophilicity on diffusion of tirapazamine analogues in multicellular layer cultures**. *J. Med. Chem.* 2005, **48**(4):1079–1087.

[122] Secomb TW, Hsu R, Park EYH, Dewhirst MW: **Green's Function Methods for Analysis of Oxygen Delivery to Tissue by Microvascular Networks**. *Annals of Biomedical Engineering* 2004, **32**(11):1519–1529.

[123] Tannock IF: **Oxygen diffusion and the distribution of cellular radiosensitivity in tumours**. *The British Journal of Radiology* 1972, **45**:515–524.

[124] Gullino PM, Grantham FH, Courtney AH: **Utilization of Oxygen by Transplanted Tumors in Vivo**. *Cancer Res* 1967, **27**(6 Part 1):1020–1030.

[125] Reinhold H, DeBree C: **Tumour cure rate and cell survival of a transplantable rat rhabdomyosarcoma following X-irradiation**. *European Journal of Cancer* 1968, **4**:367–374.

[126] Lin SH: **Oxygen diffusion in a spherical cell with nonlinear oxygen uptake kinetics**. *Journal of Theoretical Biology* 1976, **60**(2):449–457.

[127] Rasey JS, Koh WJ, Grierson JR, Grunbaum Z, Krohn KA: **Radiolabeled fluoromisonidazole as an imaging agent for tumor hypoxia**. *International Journal of Radiation Oncology*Biology*Physics* 1989, **17**(5):985–991, [[http://www.sciencedirect.com/science/article/pii/0360301689901466]].

[128] Cowan DS, Hicks KO, Wilson WR: **Multicellular membranes as an in vitro model for extravascular diffusion in tumours.** *Br J Cancer Suppl* 1996, **27**:S28–S31, [[http://www.ncbi.nlm.nih.gov/pmc/articles/PMC2149990/]].

[129] Kumar P, Stypinski D, Xia H, McEwan AJB, Machulla HJ, Wiebe LI: **Fluoroazomycin arabinoside (FAZA): synthesis, 2H and 3H-labelling and preliminary biological evaluation of a novel 2-nitroimidazole marker of tissue hypoxia**. *Journal of Labelled Compounds and Radiopharmaceuticals* 1999, **42**:3–16, [[http://onlinelibrary.wiley.com/doi/10.1002/(SICI)1099-1344(199901)42:1<3::AID-JLCR160>3.0.CO;2-H/abstract]].

[130] **Molinspiration Property Calculation Service**. *[http://www.molinspiration.com]* 2013. [2013-07-02].

[131] **VCCLAB, Virtual Computational Chemistry Laboratory**. *[http://www.vcclab.org/lab/alogps/]* 2013. [2013-07-02].

[132] Cheng T, Zhao Y, Li X, Lin F, Xu Y, Zhang X, Li Y, Wang R, Lai L: **Computation of octanol-water partition coefficients by guiding an additive model with knowledge**. *J Chem Inf Model* 2007, **47**(6):2140–2148.

[133] Dearden JC: **Prediction of Physicochemical Properties**. In *Computational Toxicology*, no. 929 in Methods in Molecular Biology. Edited by Reisfeld B, Mayeno AN, Humana Press 2012:93–138.

[134] Brown JM, Workman P: **Partition coefficient as a guide to the development of radiosensitizers which are less toxic than misonidazole**. *Radiat. Res.* 1980, **82**:171–190.

[135] Biskupiak JE, Grierson JR, Rasey JS, Martin GV, Krohn KA: **Synthesis of an (iodovinyl)misonidazole derivative for hypoxia imaging**. *J. Med. Chem.* 1991, **34**(7):2165–2168.

[136] Dubois LJ, Lieuwes NG, Janssen MHM, Peeters WJM, Windhorst AD, Walsh JC, Kolb HC, Ollers MC, Bussink J, van Dongen GAMS, van der Kogel A, Lambin P: **Preclinical evaluation and validation of [18F]HX4,**

a promising hypoxia marker for PET imaging. *Proc. Natl. Acad. Sci. U.S.A.* 2011, **108**(35):14620–14625.

[137] Griffiths JR, Robinson SP: **The OxyLite: a fibre-optic oxygen sensor**. *Br J Radiol* 1999, **72**:627–630.

[138] Troost EGC, Laverman P, Philippens MEP, Lok J, van der Kogel AJ, Oyen WJG, Boerman OC, Kaanders JHAM, Bussink J: **Correlation of [18F]FMISO autoradiography and pimonidazole [corrected] immunohistochemistry in human head and neck carcinoma xenografts**. *Eur. J. Nucl. Med. Mol. Imaging* 2008, **35**(10):1803–1811.

[139] Wack LJ, Mönnich D, Yaromina A, Zips D, Baumann M, Thorwarth D: **Correlation of FMISO simulations with pimonidazole-stained tumor xenografts: A question of O2 consumption?** *Med Phys* 2016, **43**(7):4113–4121.

[140] Toustrup K, Sørensen BS, Nordsmark M, Busk M, Wiuf C, Alsner J, Overgaard J: **Development of a hypoxia gene expression classifier with predictive impact for hypoxic modification of radiotherapy in head and neck cancer**. *Cancer Res.* 2011, **71**(17):5923–5931.

[141] Zschaeck S, Haase R, Abolmaali N, Perrin R, Stützer K, Appold S, Steinbach J, Kotzerke J, Zips D, Richter C, Gudziol V, Krause M, Zöphel K, Baumann M: **Spatial distribution of FMISO in head and neck squamous cell carcinomas during radio-chemotherapy and its correlation to pattern of failure**. *Acta Oncol* 2015, **54(9)**:1355–1363.

[142] Bentzen SM: **Theragnostic imaging for radiation oncology: dose-painting by numbers**. *Lancet Oncol.* 2005, **6**(2):112–117.

[143] Hendrickson K, Phillips M, Smith W, Peterson L, Krohn K, Rajendran J: **Hypoxia imaging with [F-18] FMISO-PET in head and neck cancer: potential for guiding intensity modulated radiation therapy in overcoming hypoxia-induced treatment resistance**. *Radiother Oncol* 2011, **101**(3):369–375.

[144] Thorwarth D, Eschmann SM, Paulsen F, Alber M: **A model of reoxygenation dynamics of head-and-neck tumors based on serial 18F-fluoromisonidazole positron emission tomography investigations**. *Int. J. Radiat. Oncol. Biol. Phys.* 2007, **68**(2):515–521.

[145] Bartlett RM, Beattie BJ, Naryanan M, Georgi JC, Chen Q, Carlin SD, Roble G, Zanzonico PB, Gonen M, O'Donoghue J, Fischer A, Humm JL: **Image-guided PO2 probe measurements correlated with parametric images derived from 18F-fluoromisonidazole small-animal PET data in rats**. *J. Nucl. Med.* 2012, **53**(10):1608–1615.

[146] Busk M, Munk OL, Jakobsen S, Wang T, Skals M, Steiniche T, Horsman MR, Overgaard J: **Assessing hypoxia in animal tumor models based**

on pharmocokinetic analysis of dynamic FAZA PET. *Acta Oncol* 2010, **49**(7):922–933.

[147] Lewis JS, McCarthy DW, McCarthy TJ, Fujibayashi Y, Welch MJ: **Evaluation of 64Cu-ATSM in vitro and in vivo in a hypoxic tumor model**. *J. Nucl. Med.* 1999, **40**:177–183.

[148] Wack LJ, Mönnich D, van Elmpt W, Zegers CML, Troost EGC, Zips D, Thorwarth D: **Comparison of [18F]-FMISO, [18F]-FAZA and [18F]-HX4 for PET imaging of hypoxia - a simulation study**. *Acta Oncol* 2015, **54**:1370–1377.

[149] Busk M, Jakobsen S, Horsman MR, Mortensen LS, Iversen AB, Overgaard J, Nordsmark M, Ji X, Lee DY, Raleigh JR: **PET imaging of tumor hypoxia using ^{18}F-labeled pimonidazole**. *Acta Oncologica* 2013, **52**(7):1300–1307, [[http://www.tandfonline.com/doi/full/10.3109/0284186X.2013.815797]].

[150] Peeters SGJA, Zegers CML, Biemans R, Lieuwes NG, van Stiphout RGPM, Yaromina A, Sun JD, Hart CP, Windhorst AD, van Elmpt W, Dubois LJ, Lambin P: **TH-302 in Combination with Radiotherapy Enhances the Therapeutic Outcome and Is Associated with Pretreatment [18F]HX4 Hypoxia PET Imaging**. *Clin. Cancer Res.* 2015, **21**(13):2984–2992.

[151] Bentzen L, Keiding S, Nordsmark M, Falborg L, Hansen SB, Keller J, Nielsen OS, Overgaard J: **Tumour oxygenation assessed by 18F-fluoromisonidazole PET and polarographic needle electrodes in human soft tissue tumours**. *Radiother Oncol* 2003, **67**(3):339–344.

[152] Rasey JS, Grunbaum Z, Magee S, Nelson NJ, Olive PL, Durand RE, Krohn KA: **Characterization of radiolabeled fluoromisonidazole as a probe for hypoxic cells**. *Radiat. Res.* 1987, **111**(2):292–304.

[153] Souvatzoglou M, Grosu AL, Roper B, Krause BJ, Beck R, Reischl G, Picchio M, Machulla HJ, Wester HJ, Piert M: **Tumour hypoxia imaging with [18F]FAZA PET in head and neck cancer patients: a pilot study**. *Eur. J. Nucl. Med. Mol. Imaging* 2007, **34**(10):1566–1575.

[154] Geets X, Grégoire V, Lee JA: **Implementation of hypoxia PET imaging in radiation therapy planning**. *Q J Nucl Med Mol Imaging* 2013, **57**(3):271–282.

[155] Toma-Dasu I, Dasu A: **Modelling Tumour Oxygenation, Reoxygenation and Implications on Treatment Outcome**. *Computational and Mathematical Methods in Medicine* 2013, **2013**, [[http://www.hindawi.com/journals/cmmm/2013/141087/abs/]].

[156] Wehrl HF, Hossain M, Lankes K, Liu CC, Bezrukov I, Martirosian P, Schick F, Reischl G, Pichler BJ: **Simultaneous PET-MRI reveals brain function in activated and resting state on metabolic, hemodynamic and multiple temporal scales**. *Nat. Med.* 2013, **19**(9):1184–1189.

[157] Doss M, Zhang JJ, Bélanger MJ, Stubbs JB, Hostetler ED, Alpaugh K, Kolb HC, Yu JQ: **Biodistribution and radiation dosimetry of the hypoxia marker 18F-HX4 in monkeys and humans determined by using whole-body PET/CT**. *Nucl Med Commun* 2010, **31**(12):1016–1024.

9 Acknowledgments

First and most importantly, I would like to thank my supervisor Prof. Daniela Thorwarth for her support and encouragement during the last four years. Her insight and helpful guidance made this thesis possible in the first place. I would also like to thank Prof. Fritz Schick for his valuable feedback on my work. I am very grateful to Prof. Daniel Zips for the insightful discussions of the projects while I was working on my thesis.

I also owe thanks to our collaborateurs in Maastricht, particularly Dr. Catharina Zegers, Dr. Wouter van Elmpt and Prof. Esther Troost, for providing us with the much-needed HX4 imaging data, and our colleagues in Dresden, particularly Dr. Ala Yaromina and Prof. Michael Baumann for sharing their knowledge on tumor biology and immunofluorescence staining. Many thanks go to Katrin Trautmann from the Department of Neuropathology for her practical help with the tumor cutting, and to the Department of Urology for help with the HE staining. Also, I thank the Department of Experimental Ophthalmology allowing me to use their fluorescence microscope.

I would also like to thank Dr. David Mönnich for his help with the simulation in the last four years. His valuable insight helped me overcome many obstacles and his constructive criticism has been invaluable. Many thanks also to Dr. Apostolos Menegakis, whose help with immunofluorescence staining and microscopy was a priceless contribution to this work.

Many thanks go to the Section for Biomedical Physics and the Department of Radiation Oncology for creating a wonderful work atmosphere. Thanks to David, Sara, René, Simon, Kerstin, Jairo, Anja, Jenny, Valentin, Urban, Benjamin, Apostolos, Dominik, Aline, Viktoria, Jens, Jule, Raphael, Max, Luise, Johanna, Fiona, Sharin, Stefan, Oliver and Bastian for interesting and fun coffee breaks. Special thanks go to David Mönnich and Stefan Poijtinger for being great office mates who I will miss dearly.

Many thanks also to my parents and my sister, who supported me all this time. Many thanks to Gisela and Günther Muth for hosting me for many dinners. Last but not least, I would like to thank Bastian Muth, for his unconditional support while I was working on this thesis.